

DOE/ER/542-41-159

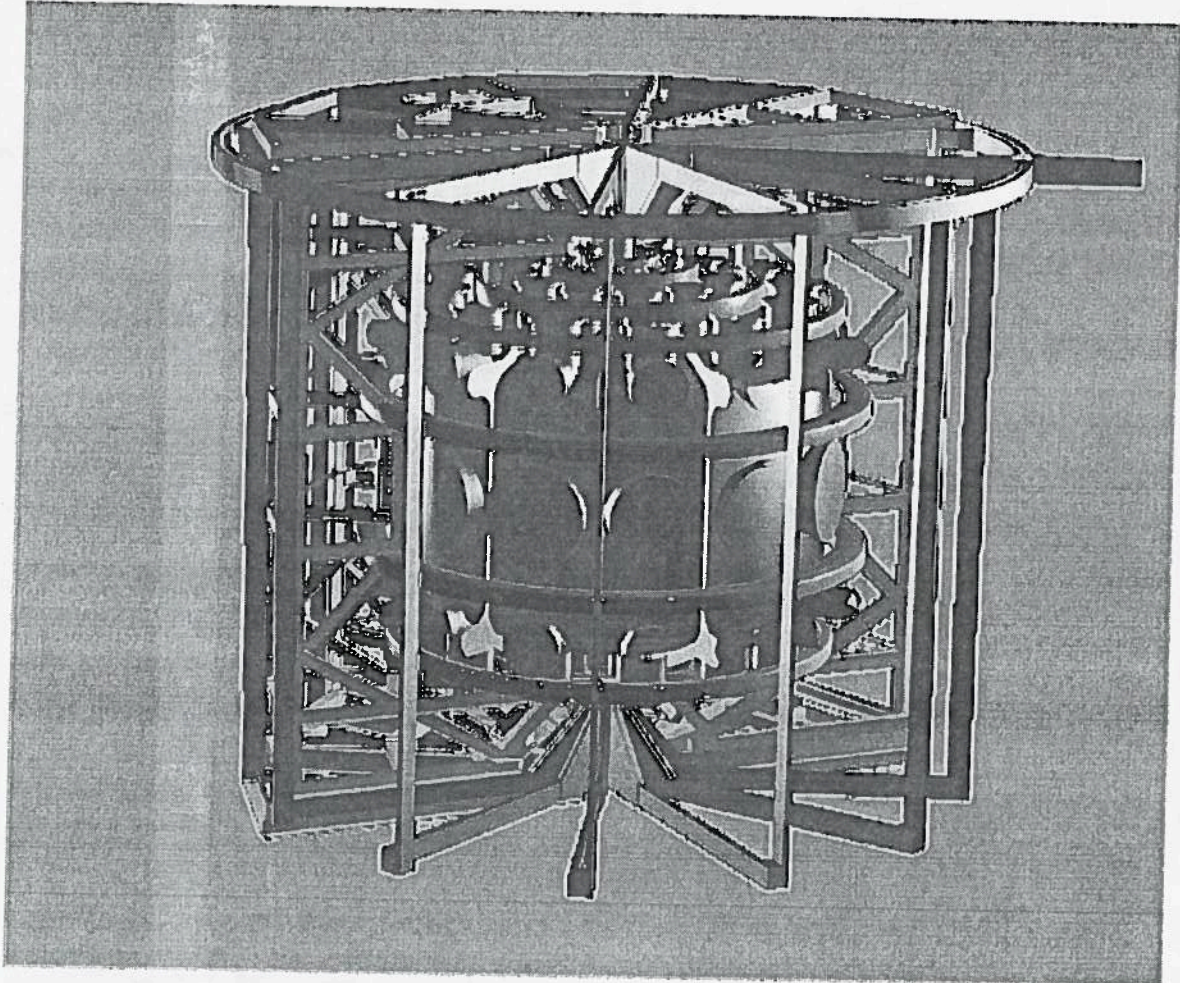
FRCR #480

**THE UNIVERSITY SPHERICAL
TOKAMAK EXPERIMENT - USTX**

**THE FUSION RESEARCH CENTER
The University of Texas at Austin
Austin, Texas 78712**

February 15, 1996

USTX



The University Spherical Tokamak Experiment

**Fusion Research Center
The University of Texas at Austin
Feb. 15, 1996**

**Proposal for Award of Grant
USTX
THE UNIVERSITY SPHERICAL
TOKAMAK EXPERIMENT**

A Plasma Research Facility

July 1, 1996 - June 30, 1999

**Fusion Research Center
The University of Texas at Austin
Austin, TX 78712**

**PREPARED FOR THE U.S. DEPARTMENT OF ENERGY
OFFICE OF ENERGY RESEARCH**

Table of Contents

i. Executive Summary

1. Overview of the USTX Project

- 1.1 Historical perspective: previous work
- 1.2 The point design and device description
- 1.3 USTX experimental program and goals (deliverables)
- 1.4 Schedule and cost summary
- 1.5 Site issues and cost effectiveness
- 1.6 Relationship of USTX to other proposals

2. Fusion-Oriented Rationale for Low Aspect Ratio

- 2.1 Machine architectural parameters
- 2.2 System studies: desirable properties at low aspect ratio
- 2.3 Critical questions to be addressed on USTX

3. Physics of Low Aspect-Ratio Tokamaks

- 3.1 Basic issues
- 3.2 Equilibrium and position-stability control
- 3.3 MHD stability and high-beta operation
- 3.4 Neoclassical effects
- 3.5 Turbulence and transport
- 3.6 Heating and current drive

4. Physics Design Considerations: Confinement

- 4.1 Design strategy and logic
- 4.2 Smallest credible machine size
- 4.3 Device optimization studies, performance estimates and flexibility

5. Physics Design Considerations: Magnetics

- 5.1 OH solenoid design strategy
- 5.2 Breakdown fields
- 5.3 Plasma current ramp rate
- 5.4 Plasma shape control
- 5.5 Plasma position control
- 5.6 Fault conditions
- 5.7 Time dependent simulation
- 5.8 Toroidal field coils
- 5.9 MHD stability

6. Device and Power Systems Description

- 6.1 Overall description

- 6.2 TF coil, OH solenoid and PF coils
- 6.3 Vacuum vessel and plasma-facing components
- 6.4 Support structure
- 6.5 Construction and assembly plan
- 6.6 Vessel pumping and bakeout
- 6.7 Power systems

7. Auxiliary Plasma Heating and Current Drive

- 7.1 Bootstrap current estimates
- 7.2 Neutral beam injection
- 7.3 ECH startup assist scenarios
- 7.4 Fast and Alfvén wave current drive system
- 7.5 Coaxial helicity injection

8. Diagnostics, Control, and Data Analysis

- 8.1 Overview
- 8.2 Proposed diagnostics set
- 8.3 Selected diagnostics and the needs of USTX
- 8.4 Data acquisition and analysis

9. USTX Research Program

- 9.1 Experimental schedule and alternatives
- 9.2 Experimental studies
- 9.3 Remote site operations
- 9.4 National facility organization and collaborators

10. Costs, Schedules, and Project Management

- 10.1 Project Management
- 10.2 Costs
- 10.3 Machine Operations
- 10.4 Schedule

Appendices

- A. Background and Experience of the Principal Investigator
- B. Description of Facilities and Resources of the Applicant
- C. Statement of Current and Pending Support
- D. Assurances and Certifications that Apply
- E. Annotated FRC Publication List
- F. Letter from ASIPP
- G. Magnetic Island Research on USTX, Auburn University

Executive Summary

Mission Statement

Low-aspect-ratio tokamaks have been predicted to have advantages both as neutron sources and as compact thermal reactors [1]. The Fusion Research Center at the University of Texas proposes to design, build, and operate, in collaboration with ASIPP (Hefei, The People's Republic of China), the University Spherical Tokamak Experiment (USTX), a low-aspect-ratio tokamak with major radius $R_0 \approx 0.7$ m, aspect ratio $A = R_0/a \approx 1.25 - 1.5$, where a is the minor radius, and toroidal plasma current $I_p \approx 1$ MA. USTX is intended to access high beta, high normalized beta, and low collisionality plasmas, with plasma properties dominated by the physics of low aspect ratio. It will be devoted to the study of stability, of global and local confinement and turbulence properties, and of plasma current-initiation and current-drive schemes. The research program will be carried out in collaboration with other laboratories and universities. To minimize start-up costs, the research is segmented into logical phases, with funding for each phase dependent on the success of the previous phase. We are presently requesting funding only for Phase I, but a discussion of subsequent phases is included to indicate our long term planning.

The flexible design of USTX allows for replacement of the vessel inner cylinder, toroidal-field inner leg and ohmic solenoid, so that arbitrarily small A can be investigated (even including a spheromak configuration). The flexible poloidal field system allows for large variations in plasma elongation and triangularity. A divertor option is included. Once a suitable current drive scenario has been identified, the toroidal and poloidal field systems will ultimately allow a pulse length exceeding two seconds.

USTX is designed to be the smallest, least expensive machine capable of answering the following key physics questions:

1. Can plasmas with confinement dominated by physics at low A be operated at $A \approx 1.4$, $A \approx 1.25$, and possibly lower? No existing machine meets this criterion.
2. What operating regimes are available? In particular, what current density profiles can be achieved, and what is the lowest safety factor q for operation?
3. What are the confinement and turbulence properties at low A , particularly at high β , high β_N , and low collisionality? What is the scaling of energy confinement with A , what gains over L mode can be achieved, what pressure-profile peaking factors can be achieved, and what impurity accumulation effects exist? How do these values compare with those at normal A ?
4. What is the maximum permissible beta at low A , and how does it compare with the normal- A case? Values of $\beta_N \approx 3 - 5$ should be attained.

5. Can low- A tokamaks be operated disruption free at low q ?
6. Is a divertor possible on a low- A tokamak? Can wide scrape-off layers be produced?

Further questions to be addressed in Phase II:

1. What fraction of I_p can be maintained by a well aligned bootstrap current?
2. What non-inductive I_p -drive schemes can be used, and with what efficiency?
Note: low power tests will be performed in Phase I.
3. Can high confinement, high beta, low safety factor, large bootstrap-current fraction, and high current-drive efficiency be obtained simultaneously? What is the potential of such a device as a scaled version of a prototypical low- A reactor?

Motivation for Low Aspect Ratio: Fusion

The principal gain of low A is that a smaller device can be built to achieve a given fusion power. The unexplained confinement scalings obtained with $A \approx 3$ to 4 show that, very approximately, the triple product $nT\tau_E$ varies as $(I_p A)^2$, where n is the density, T the temperature and τ_E the energy confinement time. The predicted loss in confinement at low A must be offset by the larger plasma current which can in principle be utilized. If the energy cost associated with driving this increased current is ignored, and if the implied hollow current densities can be maintained (by current drive and bootstrap current), then tokamaks with $A \approx 1.25$ reduce the overall machine volume to less than one half that at normal A .

In the short term a driven (non-ignited) low- A tokamak is envisioned as a neutron source. D-T reactors of low- A are also under consideration, but on a longer time scale than those of normal A because of engineering difficulties. These include the design of a toroidal field-coil inner leg that can withstand the neutron fluxes from D-T reactions without a neutron shield. One proposed solution is to use D-He³, which has a much reduced neutron flux, with $A \approx 2$ [2]. This solution is also long term, because of the necessity to produce He³.

Without experimental data, especially on confinement and operational regimes (*e.g.*, the lowest q value which can be maintained) the possible advantages of low A , now seen as $1.25 < A < 2$, cannot be assessed. There are no data in which the physics of low-aspect ratio dominates confinement. There are also no data in which reactor relevant dimensionless parameters have been reached. Therefore the next step in low- A tokamak research should be a flexible device of minimum size and cost to address physics issues. USTX is this step.

Motivation for Low Aspect Ratio: Plasma Physics

Theoretical expectations and previous experimental results on small machines lead us to expect

- a higher safety factor q for a given plasma current I_p

- stability at $\langle\beta\rangle \approx 30 - 60\%$ (a high β_N expectation for a given q)
- potentially disruption-free operation
- a high bootstrap-current fraction
- a large paramagnetism
- high edge magnetic shear, good for MHD stability
- a natural exhaust region (divertor)
- no necessity for feedback and wall stabilization.

If operation at low edge safety factor $q(a)$ is to be successful, then hollow toroidal plasma current densities must be produced and maintained by current drive and bootstrap currents. Therefore USTX can address such 'advanced tokamak' physics issues. The success of current drive scenarios will be crucial to the following generation of low-aspect-ratio machines. USTX will allow tests of these before they must be relied upon. For cost effectiveness, it is imperative to carry out low-power tests before proceeding to high power experiments.

Experiments on USTX will provide tests of toroidal theories of stability and confinement in which toroidal effects can no longer be treated as a perturbation. Any theory withstanding the rigors of these tests is then suitable for application at any aspect ratio. USTX will allow tests of bootstrap-current fractions, and all other neoclassical effects (because of the large trapped particle population). The variation in plasma parameters will allow tests of transport models which predict an increasing importance of magnetic turbulence as beta increases. Understanding confinement at low A will help us to gain precision and better understanding of confinement at normal A . Finally, the central core of a low- A tokamak simulates the confinement zone of a *larger* normal- A tokamak, allowing a program of basic physics studies relevant to the main line of tokamak research.

Costs, Schedules and Collaborations

USTX, a device suitable for investigating low- A current initiation and ramp-up, equilibria, operational regimes, stability, beta limits, and confinement properties can be constructed for a U.S. cost of \$3.5M. ASIPP would contribute the equivalent of \$9.3M. Initial plasma operation is expected approximately 33 months from initiation of funding, assuming a satisfactory funding profile. Routine operation of USTX is expected to cost the U.S. approximately \$2.8M per year.

USTX has been designed as a collaborative effort among many institutions. It is intended that operation will be as a National Facility with various institutions taking responsibility for major physics topics, in particular various current-drive techniques.

References

- [1] Y.-K. M. Peng, ITC6, Fusion Tech. (1995) to be published.
- [2] B. B. Kadomtsev and V. I. Pistunovich, in *Research Trends in Physics: New Ideas in Tokamak Confinement* (La Jolla International School of Physics, The Institute for Advanced Physics Studies), edited by V. Chan, N. Fisch, V. E. Golant, *et al.*, (American Institute of Physics, New York, 1994), p. 55.

CHAPTER 1

OVERVIEW OF THE USTX PROJECT

As part of the international research program to develop an economical fusion-reactor concept, the tokamak has been a durable front-runner. Tokamaks have achieved an order of magnitude greater product of density, temperature, and confinement time than other concepts, hence the programmatic emphasis on tokamaks over other concepts. However, presently envisioned conventional tokamak-reactor scenarios are only marginally economical. This combination of factors is a compelling reason to pursue a significantly different approach while retaining the basic tokamak concept. Development of the low-aspect-ratio tokamak concept is arguably the most promising such approach.

In this chapter we summarize the University Spherical Tokamak Experiment (USTX) project and its purpose, which derives from the predicted advantages of low-aspect-ratio tokamaks, both as neutron sources and as compact thermal reactors [1]. These advantages have not been tested experimentally, nor has their theoretical basis been fully worked out. Indeed, much of the physics of low aspect ratio remains unexamined. The needed examination should begin with the smallest, least expensive device that can demonstrate the physics of low aspect ratio. A research program based on such a device affords almost limitless opportunities for both plasma-physics innovations and connections to main-line fusion research. Student training and collaboration with plasma theorists should be a major part of such a program.

Therefore, the Fusion Research Center (FRC) at the University of Texas proposes to design, build, and operate the University Spherical Tokamak Experiment, a low-aspect-ratio tokamak with major radius $R_0 \approx 0.7$ m; aspect ratio $A = R_0/a \approx 1.25-1.5$, with a the minor radius in the horizontal plane; and a toroidal plasma current $I_p \leq 1$ MA. Sufficient flexibility is incorporated to allow even smaller aspect ratios, and a variety of plasma shapes (ellipticity and triangularity). USTX is intended to be a tokamak whose plasma properties are dominated by the physics at low aspect ratio, and which can access high beta, high normalized beta, and low collisionality. It will be devoted to the study of stability, global and local confinement and turbulence properties, plasma current initiation, and testing current-drive schemes. It will also create new opportunities for

research in plasmas with high beta and high bootstrap fraction, which will be of general interest in planning reactor-class devices of either low or moderate A . We propose to carry out this research in collaboration with many other laboratories and universities. In particular, the Academia Sinica Institute of Plasma Physics (ASIPP), Hefei, People's Republic of China (PRC) will play a key role and provide substantial funding. The first version of this proposal itself was written in collaboration with the spherical tokamak group at the Oak Ridge National Laboratory as well as other groups as described below.

Low-aspect-ratio tokamaks have been discussed as possible driven neutron sources and thermal reactors, with some of the reasons and examples presented in chapter 2. In particular, low A results in smaller overall machine size than normal A . These conceptual devices are based on theoretical predictions, some of which are discussed in chapter 3, and on extrapolations from experimental results (below and chapter 2). There are no experimental results, however, on stability, confinement or operational regimes in plasmas which are dominated by the physics at low A , or in plasmas in the relevant dimensionless parameter regimes. The purpose of USTX is to remedy this lack of information in the most cost-effective manner.

Apart from developing concepts for reactors and neutron sources, there is a wealth of interesting physics at low aspect ratio such as paramagnetism, bootstrap and Pfirsch-Schlüter currents, trapped particle effects, etc. Very little is known about low-aspect-ratio tokamaks. Many of the theories applied to tokamaks are invalid at low A , and empirical confinement scaling laws don't extend to low A . The physics of low-aspect-ratio tokamaks is exciting to study in its own right, and this will be aggressively pursued in USTX.

The critical questions to be addressed on USTX are summarized in chapter 2 and the physics concepts pertaining to these are described simply in chapter 3. The smallest, least expensive machine capable of providing the answers is discussed in chapter 4. The associated magnetic design is addressed in chapter 5, with chapter 6 providing the device and power system description. Auxiliary heating is necessary for studies of extremely high beta, and this is addressed in chapter 7, as are descriptions of current-drive schemes which will be tested. Chapter 8 describes the diagnostics, which can be transferred from TEXT-U with few modifications. Chapter 9 presents the experiments to be undertaken and a list of potential collaborators. Finally, chapter 10 discusses the costs and schedules. Note that this proposal merely describes a preliminary design which demonstrates feasibility. The detailed physics and engineering design are yet to be performed.

1.1 Historical perspective: previous work

The concept of a spherical tokamak (ST) was first introduced by Jassby [2, 3], who pointed out its attractive small size as a potential reactor. Subsequently, a group at Oak Ridge National Laboratory (ORNL) championed the ST cause, designing and proposing several devices [1, 4-6]. ORNL has also been involved in the START spherical tokamak [7, 8] from its inception. The experimental motivation for the USTX proposal is based largely on the recent favorable results of START. This device demonstrated the feasibility of producing high-current plasmas with $I_p < 250$ kA, aspect ratio $A = 1.2$ to 1.5 , and elongation κ as high as 4 , with a toroidal field $B_T < 0.5$ T. In addition, the confinement time was found to be in rough agreement with the neo-Alcator and Lackner-Gottardi scalings [9], and no disruptions were observed for $A < 1.8$ [10]. Pulse lengths have been limited to less than 50 ms, however, due to the small ohmic heating solenoid capable of only 80 mV-s. While there have been at least ten tokamaks with $A < 1.6$ [1, 11], only four of these – FBX II [12], START, HIT [13], and CDX-U [14] – have reached $T_{e0} \geq 100$ eV. Parameters of these four machines are listed in Table 1.1.

The HIT machine has produced short-duration plasmas with $A = 1.5$ and $I_p < 200$ kA inside a copper shell. Plasma production by coaxial helicity injection in this device is encouraging for future spherical tokamaks, which will require non-inductive current drive. One additional experiment of note is TS-3 [14] in an ultra-low- A (1.05) configuration, which has achieved $I_p = 50$ kA, although only for 0.4 ms. This device has shown that the tilt instability characteristic of spheromaks can be stabilized with a very small axial current in a center conductor such that the edge safety factor $q(a) \approx 1$.

Table 1.1. Parameters of some existing low - A tokamaks.

Device Name	R_0 (m)	a (m)	A	I_p (kA)	t_{pulse} (ms)	B_{T0} (T)	T_{e0} (eV)
FBX II	0.47	0.33	1.4	100	2	0.5	300
START	0.30	0.25	1.3	250	40	0.5	500
HIT	0.30	0.20	1.5	200	10	0.46	100
CDX-U	0.32	0.20	1.6	100	10	0.12	150

1.2 The point design and device description

The overriding design strategy has been to identify the most economical and flexible device capable of accomplishing the key physics goals (described in Sec. 2.3), especially those relevant to advancing the fusion program toward an economical reactor design. As a university experimental program we are willing to take calculated risks if they have the potential for large payoffs. On the other hand, since the device we are proposing substantially departs from the existing database of tokamak performance in several respects, we feel it is not advisable to commit solely to unproven methods of current drive and heating. Most presently identified tokamak reactor candidates require non-inductive current drive (CD), and we plan to implement and study CD techniques in Phase II as described in chapters 3 and 7. Based on our assessment of the current status of CD suitable for low-A devices, however, we conclude that it is impractical to rely solely on this technology. We have analyzed the performance sensitivity of low-A devices to major input parameters such as R_0 , a , I_p , B_{T0} , and κ , and have examined the impact of engineering and physics constraints such as the central solenoid design and neutral-beam deposition. (See chapters 4 and 7, and McCool *et al.* [15].) We demonstrate in this proposal and in Ref. 15 that Ohmic operation is not only sufficient to test confinement predictions and to obtain a wealth of basic physics understanding, but also can result in very high betas. To fully test stability and confinement over all required operational regimes requires only one H^0 neutral beam. *The design we describe is of the smallest credible device capable of meeting the key physics objectives* (see Sec. 4.2).

The principal parameters of USTX are listed in Table 1.2. Their justification will appear in later sections, particularly in chapter 4. The pulse length quoted is for a double-swing ohmic solenoid without non-inductive current drive (chapters 5-6), and it is adequate for current equilibration [15, 16]. Should bootstrap and short-pulse auxiliary current drive prove successful, then long-pulse auxiliary current drive can be implemented. The toroidal and poloidal field coil systems and available stored energy in the motor generators will then allow pulse lengths exceeding two seconds (see the discussion at the end of chapter 6). The parameters listed in Table 1.2 constitute the basis for a conceptual design about a single point in parameter space, i.e., a "point design." We include numbers for both the initial base machine proposed here (Phase I) as well as the Phase II device including one neutral beam, current drive, and an $A=1.25$ solenoid. The geometric parameters of the point design are not to be considered as an optimum set, but rather as a starting point for experimental exploration: USTX is intended as a flexible assembly

allowing variations in plasma position, shape, safety factor, etc. The poloidal field coils are designed with this flexibility in mind allowing, for example, much higher triangularity to be achieved than for the nominal $A = 1.43$ point design.

Cross sections of the USTX device are shown in Fig. 1.1 – under a toroidal field coil on the left, and between coils on the right. USTX utilizes a domed thin-wall vacuum vessel with no toroidal insulating breaks, and has excellent diagnostic access with space reserved at the outside equator for RF antennas. It has twelve large demountable toroidal

Table 1.2. The USTX principal parameters (point-design parameters in parentheses, Phases defined in Sec. 1.3).

Parameter		Phase I	Phase II
A	aspect ratio	1.33 - 2.0 (1.43)	1.22 - 1.7 (1.25)
R ₀	major radius	≤ 0.85 m (0.70 m)	≤ 0.85 m (0.75 m)
a	minor radius	≤ 0.64 m (0.49 m)	≤ 0.67 m (0.60 m)
κ	elongation	1.5 - 2.0 (1.7)	1.5 - 2.0 (2.0)
δ	triangularity	0 - 0.5 (0.25)	0 - 0.5 (0.5)
I _{p,max}	plasma current	1.0 MA	0.5 MA + non-inductive CD
t _{pulse}	pulse length	130-350 ms‡	> 2 s
B _{T0}	toroidal vacuum field on axis	≤ 0.5 T at R = 0.7 m	
n̄ _e	electron density	0.2 - 1.5×10 ²⁰ m ⁻³ (0.7×10 ²⁰)	
T _{e0}	electron temperature on axis	1 - 2 keV from scaling law study*	
T _{i0}	ion temperature on axis	0.6 - 1.2 keV	
τ _E	confinement time	20 - 90 ms (50 ms)	
⟨β⟩	= 2 μ ₀ ⟨p⟩/B _{T0} ²	~ 30%*	
Auxiliary Heating and Current Drive			
ω _{ce} breakdown		40 kW at 14 GHz	
ECH		400 - 600 kW at 60 GHz (2ω _{ce} T _e ramp)	
NBI†, H ⁰ → D ⁺ or D ⁰ → D ⁺			1.25 - 1.5 MW at 40 - 60 keV
Alfvén- and fast-wave current drive†			2 MW at 3-13 MHz for 100 ms

[‡]sensitive to plasma model.

*Scaling studies and β limits are discussed in chapter 4. A Troyon factor $\beta_N \approx 3$ to 5 should be obtained with less than 1.5 MW of auxiliary power. For Lackner-Gottardi scaling, $\langle \beta \rangle = 22\%$ and $\beta_N = 3.7$ should be possible with Ohmic heating only.

[†]NBI and Alfvén heating and current drive are planned for Phase II. Alfvén- and fast-wave current drive assumed to be provided and funded by collaborators (e.g., UWM, chapter 7).

field (TF) coils producing minimal ripple, five pairs of poloidal field coils providing sufficient coverage to allow for a range of plasma shapes, and a center vessel core including the ohmic-heating solenoid and TF center post. The center core is designed to be removable with one planned initially for $A = 1.43$ and a second solenoid with $A = 1.25$ planned for Phase II (even a spheromak configuration is potentially possible). The $A = 1.43$ solenoid is capable of inductively driving $I_p = 1.0$ MA, compared to 500 kA with the $A = 1.25$ solenoid. This two-solenoid plan allows for full 1-MA studies without relying on unproven CD techniques which will be investigated in Phase II.

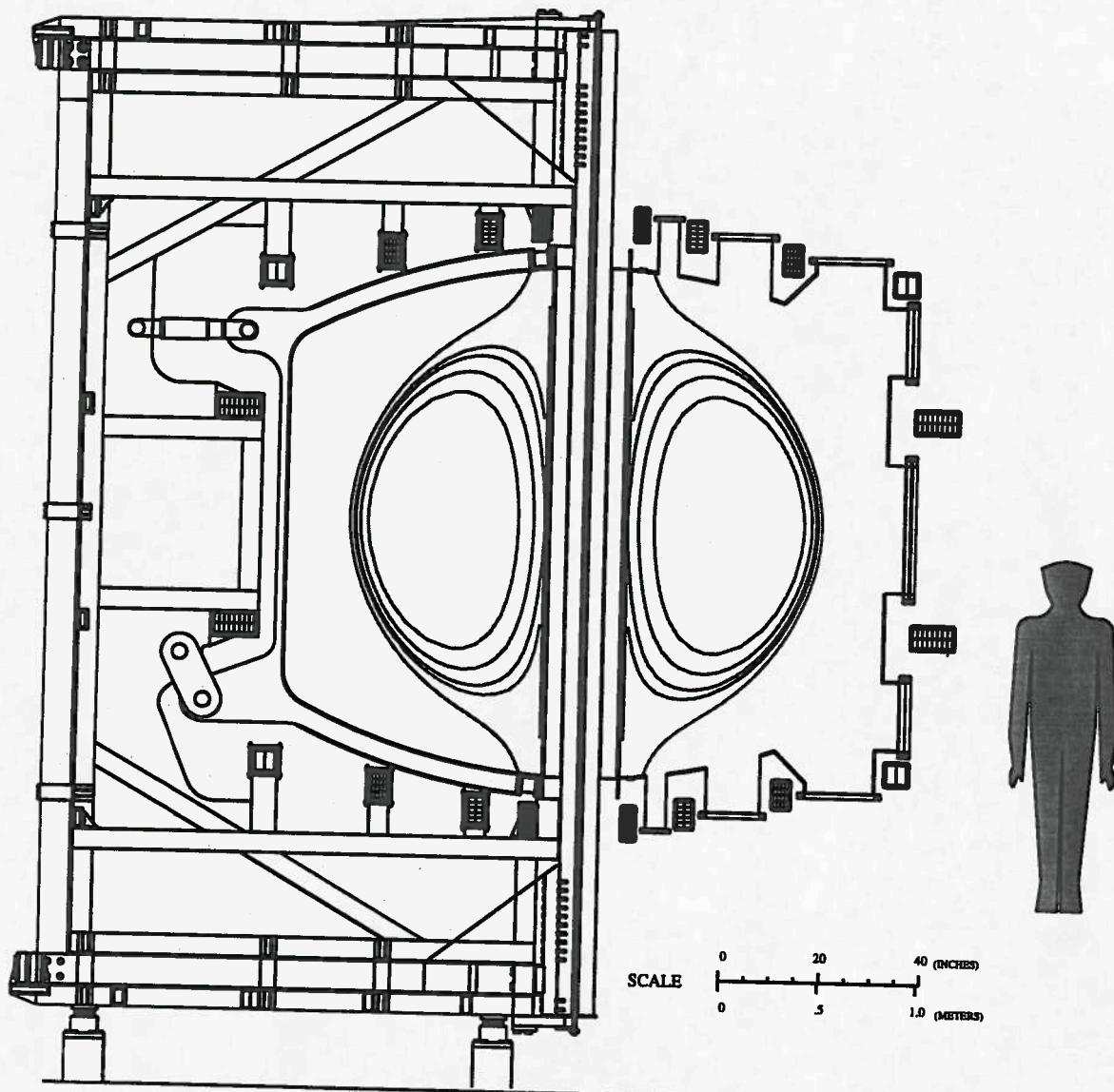


FIG. 1.1. Cross section of USTX. The left-hand side is a cross section in a plane between flanges. The right-hand side is a cross section in a plane centered on the flanges and omitting the support structure.

1.3 USTX experimental program and goals (deliverables)

Here we summarize the experimental schedule and list the deliverables expected from the project. In later chapters we describe some of the considerations leading to the engineering and experimental program, together with details of the proposed research. All required diagnostics (chapter 8) are currently available on TEXT-U and will be transferred with minimum modification to USTX. More details of specific experiments are found in chapter 9.

Experimental schedule

The experimental schedule presented here assumes that the initial plasma will have an aspect ratio $A = 1.43$, with $A \geq 1.33$ possible if no antennas occupy space at the outer equator. An $A = 1.25$ option is to be designed and built in Phase II. Further lower- A options are possible because of the vessel inner-cylinder design (chapter 6). Modification for a divertor option is feasible (chapter 9).

Phase I – Build USTX with $A = 1.43$, $I_p \approx 1.0$ MA. Earliest operation in Spring 1999.

- Commission basic diagnostics, control systems, wall preparation techniques.
- Determine OH operating regimes, MHD characteristics, and global confinement properties, especially at high β and high β_N .
- Explore various current-initiation schemes including ECH assisted breakdown and low toroidal-field breakdown and ramp-up for beta optimization and pulse-length extension.
- Investigate scrape-off-layer (SOL) parameters.
- Study internal reconnection events (IRE's).
- Study turbulence and transport at low A , high β .
- Determine operational regime and study MHD stability limits.
- Categorize at low A the phenomena which limit operation at normal A .
- Study sawteeth and their effects on low- q operation.
- Determine confinement properties:
 - scaling with machine parameters,
 - scaling with dimensionless parameters,
 - turbulence.
- Evaluate whether a subsidiary outer wall is required to obtain maximum beta.

- Study stability and feasibility of hollow current-density profiles.
- Study basic wave phenomena in preparation for current-drive scenarios.
- Provide a test bed for low-power studies of novel and potential breakthrough techniques of non-inductive current drive.
- Determine if SOL parameters lend themselves to a divertor option (included in proposal).
- Measure parameters necessary to determine which $A = 1.25$ option to build.
- Design and build new solenoid, toroidal-field post and vacuum-vessel inner cylinder for Phase II.

Phase II – Add 1.25 MW of neutral-beam injection. This provides heating, current drive, and rotation (to improve stability at high beta and to reduce the impact of locked modes). Earliest operation in Fall 2000. (NBI will be added at the earliest possible date if funding permits.) Build and operate the $A = 1.25$ option with inductive or non-inductive start-up, non-inductive current drive, and auxiliary heating. Possible addition of helicity injection hardware. Earliest operation in Winter 2000.

- Compare bootstrap current with theoretical predictions.
- Optimize non-inductive current drive including high-power fast-wave CD, and attempt to develop a non-inductive scenario from breakdown to flat-top.
- Seek a regime with simultaneous moderate q (important because the power dissipated in the TF post may limit ST reactor performance), high confinement, high bootstrap fraction, and high current-drive efficiency.

The development of non-inductive current-initiation and current-drive schemes is a major goal of USTX. We cannot formulate a well developed experimental schedule for their evaluation until theoretical work has provided insight into the utility of various conceptual current-drive techniques.

Deliverables (all partially addressed in Phase I, some ultimately addressed in Phase II)

As a consequence of the experimental plan tabulated above, we plan to:

- Assess the viability of building and operating a 1-MA inductively driven and heated (ultimately, neutral-beam and RF heated) low-aspect-ratio tokamak and

document the engineering and physics problems encountered. We will compare the critical parameters assumed in the design process with those measured, in particular volt-second consumption, current-density profile evolution, and disruption currents and voltages (chapter 5). The vessel structure and measures that will be taken to handle disruption forces are discussed in chapter 6.

- Compare phenomena occurring at normal aspect ratio with those found at predominantly low aspect ratio, e.g. axisymmetric modes, tearing modes, sawteeth, ballooning modes and second stability, locked modes, and disruptions.
- Assess the possible operating regimes of a 1-MA inductively driven, ultimately auxiliary heated low-aspect-ratio tokamak. In particular, we will investigate whether the regimes found in normal tokamaks ($A \geq 3.5$) exist at low A , e.g., improved ohmic confinement, L mode, natural H mode, biased H mode, VH mode, and detached plasmas. We will compare the models explaining these regimes with the physics parameters measured in USTX.
- Present scalings for global confinement times (energy, particle, impurity, momentum) in a plasma dominated by low- A physics, especially at high beta, high normalized beta, and low collisionality. These will be cast in both engineering and dimensionless parameters. We will emphasize ρ_i^* because it is the only dimensionless parameter varying significantly from USTX to proposed reactors. By comparison with existing data we will study whether it is possible to describe both normal and low- A tokamaks using a common scaling.
- Compare the beta limits achieved with those expected theoretically. Variables to be utilized to maximize beta include all engineering parameters, aspect ratio, plasma current profile (i.e., safety factor profile), plasma pressure profile, plasma shape, plasma-to-wall distance, and plasma rotation velocity.
- Compare local confinement properties with turbulence characteristics, both electrostatic and electromagnetic. In the plasma edge we will directly compare turbulence-driven and total fluxes, while in the interior we will use the most general available theoretical ideas to interpret the turbulence data.
- Assess different techniques of non-inductive current initiation, e.g. electron-cyclotron heating (ECH).

- Investigate various means of producing currents non-inductively, such as neutral-beam injection, bootstrap, and fast magnetosonic and Alfvén-wave absorption.
- Endeavor to produce a scaled version of a prototypical ST reactor – very low aspect ratio ($A \approx 1.25$), plasma current non-inductively initiated and driven, and auxiliary heated.

We propose to carry out this program with an FRC staff of ten scientists and faculty among other support staff as outlined in chapter 10. In addition ASIPP will provide a sufficient staff of engineers, scientists, and technicians necessary to construct the core device and assist with operation. As part of their graduate training, approximately ten students in any given year will contribute to the project by carrying out original dissertation research. The research will also be supported by the FRC Theory Program and the Institute for Fusion Studies.

1.4 Schedule and cost summary

To build and operate Phase I of USTX we request

- \$7,230,000 over approximately three years; this includes salaries, operation, and \$3,490,000 in construction costs.
- \$2,760,000 per year thereafter for operation and maintenance of the machine, power supplies, heating systems and diagnostics; and computing facilities, supplies, travel, and overhead. This includes salaries and required fringe benefits of FRC staff and students and ~12 ASIPP staff on site.

The load assembly, suitable for investigating low- A current initiation and ramp-up, equilibria, operational regimes, stability, beta limits, and confinement properties, will be built by the ASIPP. At least one FRC engineer or technician will be on site at the ASIPP for the entire design and fabrication phase. The total equivalent U.S. construction cost including salaries is \$12.8M; of this, the US share is \$3.5M. This figure assumes that major components of the machine are designed and built in the PRC, and includes engineering supervision and quality control. The above assumes an unused P/S at Lawrence Livermore National Laboratory (LLNL) is made available; if not, the US cost is increased by \$0.3M. Assuming initiation of funding in July, 1996 and a satisfactory funding profile, initial USTX plasma operation is expected in Spring, 1999.

Our collaborators will request additional funds to build and operate current-drive hardware and additional diagnostics. For example, the University of Wisconsin at Madison has expressed interest in a current-drive concept, utilizing up to 2 MW of fast magnetosonic waves and/or Alfvén waves.

1.5 Site issues and cost effectiveness

The laboratory occupied by the TEXT-U device can house the USTX device together with ultimately two neutral beams (none are costed in this proposal) and a full complement of diagnostics (see Table 8.1). Having specified the major radius and aspect ratio (see later chapters), we find the height of the machine to be determined by the requirements of plasma shaping control. The available vertical clearance in the laboratory, 10.2 m, is sufficient to allow removal of the center core (2.6-m height).

USTX will fully utilize existing power supplies. The present toroidal-field (TF) supply is more than adequate for providing the maximum field, $B_{T0} = 0.5$ T. Most operation is envisaged at lower fields (to increase β), but should a higher field be needed, the existing TF supply was designed to be upgraded from the present 160-kA limit to 210 kA without additional cabinet space. The five poloidal field coils (other than the central ohmic solenoid) will be powered by combinations of the existing six TEXT-U poloidal-field power supplies. The neutral beam(s) when added would utilize the existing modulator-regulator units. The only power supply required that is not presently available on site is the specialized high-current OH solenoid supply. An appropriate supply exists at LLNL, but in case this is not made available, we have completed a conceptual design and costing of an appropriate supply.

The ultimate limit on pulse length capability of USTX is determined by either the primary power available to the laboratory, or stress and heating limitations in the inner core assembly (chapter 6). The presently available grid power to the laboratory is 6 MW, expandable to 8 MW for approximately \$160K. Our present motor-generator capacity is 130 MJ: "MG-0" at 100 MJ, and "MG-1" and "MG-2" each at 15 MJ. With the present optimized design, the TF pulse length is limited by heating of the TF inner leg, whereas the plasma pulse length at maximum plasma current is limited by the stored energy (or pulsed-power rating) of MG-1 and MG-2, assuming a loop voltage of 1.5 V. At an assumed loop voltage of 0.5 V, the plasma-current pulse length is limited by heating of the ohmic solenoid.

The present design calls for Phase-II installation of a single neutral beam, although space is available to install a second beam. There will be no relevant limitation on USTX operation for H^0 beams into D^+ or H^+ plasmas. We also have the capability to run D^0 into D^+ , although with currently available shielding we would be limited to several hundred maximum-performance shots per year [15], which would not restrict the envisaged experimental program.

All existing major diagnostics on TEXT-U (except those based on ECE which are hampered by the combination of low toroidal field and relatively high density), including those of collaborators, can be used on USTX with minor modifications.

The team at the Fusion Research Center with the addition of two engineers and the assistance of approximately 12 physicists and engineers from ASIPP is capable of operating the proposed USTX. The Fusion Research Center team previously operated TEXT-U, which, with its divertor, three gyrotron systems, diagnostic neutral beam, stochastic-field coil set, and full diagnostic set, was of approximately equivalent complexity. A majority of the physicists from that team are still at the FRC. That the team is capable of producing results is demonstrated by its publication record (see Appendix E).

1.6 Relationship of USTX to other proposals

Tables 1.3 and 1.4 list some of the major characteristics of USTX, together with those of PEGASUS [17], GLOBUS-M[18], MAST [19] and NSTX [20]. PEGASUS is an $A = 1.1$ START-scale machine being proposed by the University of Wisconsin, Madison. To our knowledge the Russian device GLOBUS-M, a small (10-ms pulse) Brazilian device ETE[21], and MAST (at Culham) are the only low- A tokamaks approved for construction. GLOBUS-M is designed for $A \approx 1.6$, and because of its small size, the confinement will not be dominated by the physics of low A (chapter 4). The proposal for NSTX presented by staff of the Princeton Plasma Physics Laboratory at the March, 1995 Field Task Proposals meeting at Germantown, MD, represents the most ambitious proposal, with a construction cost of \$26.5M including renovation of beam lines (\$18.5M without beam upgrades).

While the physics goals of the various proposals overlap in some areas, they differ widely in approach, and each device has unique capabilities. These proposed devices are

complementary rather than redundant. The distinguishing feature of USTX is that it is a 1-MA-class ST capable of producing a quality target plasma for RF and NBI heating and current drive for an extremely low cost (to the U.S.). Other features of USTX include the engineering approach and state-of-the-art diagnostics (such as the existing heavy-ion beam probe, to be operated by a group from the Rensselaer Polytechnic Institute). Another distinguishing feature is that USTX is to be built and operated in a university setting (in collaboration with a variety of laboratories), and will result in the training of many capable scientists. We emphasize that, with the exception of GLOBUS-M, ETE, and MAST (all outside the U.S.), none of these proposals has received construction approval. Note that the existing moderate-A tokamak database was only achieved through the combined research of some 40 devices. Existing results from low-A tokamaks are exciting but preliminary in nature. The next step in low-A tokamak research should be a flexible, minimum-size (but relevant), minimum-cost device to address physics issues crucial to the international fusion program. USTX is this step. We are eager to pursue this next step in low-A tokamak research.

Table 1.3. Comparison of spherical tokamaks either proposed or under construction.

	USTX (I → II)	NSTX (OH → CD)	MAST	PEGASUS	GLOBUS-M
R_0 (cm)	70 → 75	80	70	40	36
a (cm)	49 → 60	64	50	36	24
κ	1.7 → 2.0	2	2	1.5	2.2
$I_{p,OH}$ (MA)	1.0 → 0.5	1.0* → 0?	1 - 2	0.3	0.3
B_T (T)	0.5	0.33	0.63	0.2	0.5
$\langle \beta \rangle$	0.20 → 0.30	0.44	0.25	0.05-0.4?	0.08
A_{min}	1.33 → 1.22	1.25	1.35	1.1	1.5
flat-top (ms)*	130-350 → >2000	$\leq 500 \rightarrow > 5000$	500	<50	200
NBI capable?	Yes	Yes	Yes	No	No
diagnostics	standard + HIBP, FIR interferometry/polarimetry/scattering, reflectometry, BES, CHERS, PCI	standard + multi-channel TVTS, MSE, CHERS	?	standard + BES, CHERS, correlation reflectometry, SXR tomography	standard + HIBP
risk factors	international relations	reliance on untested start-up and CD scenarios	impurity problems, size scaling restrictions from internal coils	failure to achieve $A = 1.1$, limited OH performance	low-A physics not dominant
construction cost (\$M) [†]	U.S. cost - 3.5* Value - 12.8 [†]	18.55	13?	1.5	2.4

* sensitive to plasma model

* Phase I

* assumes significant bootstrap current

[†] includes PRC contribution in U.S. \$[†] does not include base program

Table 1.4. Physics and engineering comparison between various spherical tokamaks.

	USTX	NSTX	MAST	PEGASUS	GLOBUS-M
Physics Missions & Topics	test n_e , β , q limits; τ_E scaling vs. $A = 1.25^* - 1.7$; study turbulence at low A ; SOL, exhaust, and divertor studies; test low-voltage FWCD; develop non-inductive start-up to flat-top [*] scenario; produce/sustain hollow $j(r)$	τ_E , β , q limits; conducting shell for max. β ; low v^* , high f_{bs} , high P_{NB} , $A = 1.25$, $I_p > 1$ MA for pulse $> \tau_{skin}$. FWCD $j(r)$ control	test low- A concept - sustained plasmas at MA level, aux. heating, size; β , q , density limits; confinement - scalings at low A , neoclass. effects; S-S operation with CD; edge physics, divertor options	high- β equilibria, confinement, stability; minimal B_7 requirements and tilt stabilization; sustainment of $A=1.1$ plasma with FWCD; minimal target conditions for FW or Alfvén CD; disruption studies	feedback current, shape control; inductive start-up vs. preion. technique; high density with special wall conditioning, pumped limiters; mater. studies; RF heating studies; high β with CD; energy confinement
Current Drive & $j(r)$ Control	inductive 3-13 MHz FWCD, NBCD [*] possible helicity injection	inductive 7.5 MW FWCD, NBCD [*] helicity inj.	induction/compression NBCD upgrade	inductive 2 \rightarrow 4 MW FWCD or AWCD	inductive 3 GHz lower hybrid
OH Solenoid	4 (2) [*] layers, 0.91 (0.35) [*] V-s @ ± 60 kA, 240 (160) [*] turns	tapered, 4 layers, 0.7 V-s @ ± 20 kA	~ 1 V-s full-swing	single-layer, helical, LN cooled, 0.10-0.12 V-s @ ± 110 kA	2 layers, 116 turns, 0.31 V-s @ ± 70 kA
Aux. Heating	0.6 MW, 60 GHz ECH; 14 GHz ECH startup, 1.25 MW NBI, [*] 2 MW Alfvén [*]	5 MW NBI [*] 7.5 MW Fast or Alfvén waves	5 MW NBI upgrade	2 \rightarrow 4 MW Fast or Alfvén waves	8 MHz ICRH
Vacuum Vessel	6-mm wall, domed cylinder, R=1.5 m, h=2.6 m 80 - 350°C bake	13-mm wall, domed cylinder, R=1.6 m, h=3.3 m, 100°C bake	thick-wall cylinder, R=2 m, h=4.4 m, 200°C bake	3/8-in wall cylinder, 2 toroidal gaps, R=0.9m, h=1.5m, mild baking	2-3 mm wall, spherical, R=0.635 m, 150 - 200°C bake
Other	2 MeV HIBP (full poloidal coverage)	passive stabilizing plates	coils internal to vessel		130 keV HIBP

* phase II

* requires upgrade

References to Chapter 1

- [1] Y.-K. M. Peng, ITC6, Fusion Tech. (1995) to be published.
- [2] D. L. Jassby, *SMARTOR – A Small-Aspect-Ratio Torus for Demonstrating Thermonuclear Fusion*, Report PPPL-1371, Princeton Plasma Physics Laboratory (1977).
- [3] D. L. Jassby, Comments Plasma Phys. Controlled Fusion **3** (1978) 151.
- [4] Y.-K. M. Peng and D. J. Strickler, Nucl. Fusion **26** (1986) 769.
- [5] Y.-K. M. Peng and J. B. Hicks, in *Fusion Technology 1990* (Proc. 16th Symposium), edited by B. E. Keen, M. Huguet, and R. Hemsworth, (Elsevier Science Publisher B. V., London, UK, 1990), Vol. 2, p. 1287.
- [6] Y.-K. M. Peng, J. D. Galambos, and P. C. Shipe, Fusion Tech. **21** (1992) 1729.
- [7] A. Sykes, J. W. Connor, R. Duck, *et al.*, Plasma Phys. Controlled Fusion **35** (1993) 1051.
- [8] A. Sykes, Y.-K. M. Peng, J. W. Connor, *et al.*, in *Plasma Physics and Controlled Nuclear Fusion Research 1994*, (International Atomic Energy Agency, Vienna, 1995).
- [9] S. M. Kaye, C. W. Barnes, M. G. Bell, *et al.*, Phys. Fluids B **2** (1990) 2926.
- [10] A. Sykes, M. Bevir, R. A. Bamford, *et al.*, in *Plasma Physics and Controlled Nuclear Fusion Research 1994*, (International Atomic Energy Agency, Vienna, 1995), Vol. 1, p. 719.
- [11] G. D. Garstka, J. Basken, J. R. Danielson, *et al.*, Bull. Am. Phys. Soc. **39** (1994) 1574.
- [12] M. Irie, H. Kusama, N. Saitou, *et al.*, in *Proceedings of the 17th European Phys. Soc. Conf.*, (European Physical Society, Petit-Lancy, Switzerland, 1990), Vol. 14B, Part II, p. 626.
- [13] B. A. Nelson, T. R. Jarboe, D. J. Orvis, *et al.*, Phys. Rev. Lett. **72** (1994) 3666.
- [14] Y. Ono, A. Morita, M. Katsurai, *et al.*, Phys. Fluids B **5** (1993) 3691.
- [15] S. C. McCool, A. J. Wootton, R. V. Bravenec, *et al.*, *Optimization of a Megampere Spherical Tokamak for Beta-Limit and Confinement Studies*, Report FRCR 464, The University of Texas (1994).
- [16] D. R. Mikkelsen, Phys. Fluids B **1** (1989) 333.
- [17] R. J. Fonck, J. D. Callen, R. D. Durst, *et al.*, presentation at the U.S.-Japan Workshop for Low Aspect Ratio Tokamak and International Workshop on Spherical Torus, PPPL, Nov., 1995.
- [18] V. K. Gusev, *et al.*, *ibid.*
- [19] A. W. Morris, *et al.*, *ibid.*
- [20] S. Kaye, *et al.*, presentation at the NSTX Validation Review, PPPL, June, 1995.
- [21] G. Ludwig, L. F. W. Barbosa, E. Del Bosco, *et al.*, *ibid.*

CHAPTER 2

FUSION-ORIENTED RATIONALE FOR LOW ASPECT RATIO

Here we review some of the advantages of low aspect ratio, first using simple analytic estimates in Sec. 2.1. The emphasis is on the choice of possible reactor architectural parameters, and how they vary with aspect ratio. The many simplifying assumptions are noted. These analytic estimates are intended to complement detailed systems-code studies, by showing that many of their results can be simply understood. Note that initially no account is taken of the energy costs of either current drive or toroidal field production, but that the toroidal field costs are considered later. The code results in Sec. 2.2 do account for these and many other factors. This second section summarizes proposals for a low-aspect-ratio reactor, a low-A neutron source, and a low-A divertor test facility. Here the emphasis is on what is required to make a viable low-A option, rather than whether the physics and engineering parameters are completely consistent. Taken together, the two sections provide a set of assumptions and requirements which a low-A tokamak must satisfy if it is to be considered for a neutron or fusion power source. This set provides the basis for a list of critical questions, Sec. 2.3, which USTX must answer.

2.1 Machine architectural parameters

Low-aspect-ratio tokamaks have been proposed as possible neutron sources and as maintainable fusion power plants with a competitive cost of electricity. Here we present simple physics and scaling arguments which explain some possible advantages and disadvantages of low aspect ratio over normal aspect ratio. The assumptions which lead to the usefulness of low aspect ratio are noted; testing these assumptions provides a main part of the experimental research program in the proposed USTX facility.

D-T fusion yield

The major objective of low aspect ratio considered here, is to permit a smaller machine size than at normal aspect ratio ($A \approx 4$). Therefore, the machine-encompassing volume $V_m = 2\pi ka(R_0 + a)^2$ required to achieve a certain neutron power, with relevant

constraints applied, is derived as a function of A . In particular V_m is derived as a function of $F = P_\alpha / (W/\tau_E)$, with P_α the alpha-particle power, τ_E the energy confinement time, and W the stored energy. F is related to the ratio $Q_n = P_n / P_{\text{aux}}$, by $Q_n \approx 4F/(1-F)$. Here, P_n is the power carried out of the plasma by the neutrons, and P_{aux} is the auxiliary heating power.

For a D-T Maxwellian plasma with the reacting temperature between 5 and 20 keV, where $\langle \sigma v \rangle \propto T^2$, P_α can be written as

$$P_\alpha(W) = 1.5 \times 10^{-37} \langle nT \rangle^2 V \frac{g^2 (1 + \gamma_n + \gamma_T)^2}{1 + 2(\gamma_n + \gamma_T)}, \quad (2.1)$$

where $V(\text{m}^3) = 2\pi^2 \kappa R_0 a^2$ is the plasma volume, $\langle \dots \rangle$ denotes a volume average, the profiles of density $n(\text{m}^{-3})$ and temperature $T(\text{keV})$ are given by the following functions of γ_n and γ_T

$$n, T = n_0, T_0 \left[1 - (r/a_p)^2 \right]^{\gamma_n, \gamma_T},$$

and $g \equiv 2Z_i(Z_i - Z_{\text{eff}}) / [(Z_i - 1)(2Z_i + 1 - Z_{\text{eff}})]$ accounts for fuel dilution. Then,

$$F = 3.2 \times 10^{-22} \langle nT \rangle \tau_E \frac{g^2 (1 + \gamma_n + \gamma_T)^2}{1 + 2(\gamma_n + \gamma_T)}, \quad (2.2)$$

or, using energy balance,

$$F = \frac{2 \times 10^{-6} P_\Sigma \tau_E^2}{3V} \frac{g^2 (1 + \gamma_n + \gamma_T)^2}{1 + 2(\gamma_n + \gamma_T)}, \quad (2.3)$$

where P_Σ is the total heating power (external plus alpha). Note that in deriving the machine parameters required to achieve a certain F , the *energy cost of producing the plasma current is not considered*. To proceed further, an expression for $P_\Sigma \tau_E^2 / V$ in terms of A is required.

Confinement scaling

Consider scaling relations for τ_E of the form proposed by Goldston [1, 2];

$$\tau_E(\text{s}) = c H I_p(A) P_\Sigma(W)^{-0.5} \kappa^{0.5} R_0(\text{m})^{\alpha_R} a(\text{m})^{\alpha_a}, \quad (2.4)$$

where for L mode $c = 3.7 \times 10^{-5}$, $\alpha_R = 1.75$, and $\alpha_a = -0.37$. The factor H describes any improvement in confinement over L mode. No explicit density or toroidal field (B_T) dependence is considered. The form of the scaling with power is important, because in this particular case F is independent of power. The parameters α_R and α_a are left as free parameters to investigate how their uncertainty affects the final results. Using Eqs. (2.3) and (2.4), we find that

$$F = \frac{2 \times 10^{-6} c^2 H^2 I_p^2 \kappa R_0^{2\alpha_R} a^{2\alpha_a}}{3V} \frac{g^2 (1 + \gamma_n + \gamma_T)^2}{1 + 2(\gamma_n + \gamma_T)} \quad (2.5)$$

in MKS units. The objective is to observe how this parameter varies as A is reduced, with certain constraints applied. Equation (2.5) can be written approximately as $F \propto (I_p A)^2$; that is, reducing A degrades F , and the loss must be made up by using a larger I_p .

Constraints

The plasma current I_p in Eq. (2.5) is assumed to be restricted by the edge safety factor q , which is taken in the form of a fit to numerical and analytic low-aspect-ratio equilibria [3]:

$$q = q_{\text{cyl}} \left(1.22 - \frac{0.68}{A} \right) \left(1 - \left(\frac{1}{A} \right)^2 \right)^{-2}, \quad (2.6)$$

with the large aspect-ratio (cylindrical) part given by

$$q_{\text{cyl}} = \frac{2\pi a^2 B_{T0}}{\mu_0 I_p R_0} \left(\frac{1 + \kappa^2 (1 + 2\delta^2 - 1.2\delta^3)}{2} \right). \quad (2.7)$$

(Throughout this document we use q rather than q_ψ to denote the true safety factor.)

The plasma surface is described by the equation $R = R_0 + x$ with $x = a \cos(\alpha + \delta \sin \alpha)$ and $y = a \kappa \sin \alpha$, where δ is the triangularity and κ the vertical elongation of the cross section. (δ is not accounted for in the volume.) Note that q as written does not give the correct limit as $A \rightarrow \infty$ (see chapter 3). The toroidal field B_{T0} in Eq. (2.7) is the vacuum field at the plasma geometric axis, which is assumed to be given by

$$B_{T0} = B_{T\text{max}} (A - 1)/A. \quad (2.8)$$

That is, it is limited by restricting the field to a maximum $B_{T\max}$ at the inner toroidal-field-coil leg which has no associated radial width in the inner equatorial plane. Therefore, *the problems associated with the toroidal field generation are ignored.*

Machine size

Equations (2.5) through (2.8) can be combined to determine the architectural parameters R_0 and a , as well as the field parameters I_p and B_{T0} , uniquely as functions of the aspect ratio A . The machine-encompassing volume V_m is found to be given by

$$V_m = \left(\Lambda_m F q^2 f_{4m}(A) f_5(\delta, \kappa) \right)^{(3/(2\alpha_a - 1 + 2\alpha_R))}, \quad (2.9)$$

where

$$\Lambda_m = \frac{4.8 \times 10^{-7} \pi^2 (2\pi)^{(2\alpha_a - 1 + 2\alpha_R)/3} [1 + 2(\gamma_n + \gamma_T)]}{[c H g (1 + \gamma_n + \gamma_T) B_{T\max}]^2}, \quad (2.10)$$

$$f_{4m}(A) = \frac{(1 - (1/A)^2)^4}{(A - 1)^2} \left(1.22 - \frac{0.68}{A} \right)^{-2} A^{(5 - 2\alpha_R)} (1 + A)^{2(2\alpha_a - 1 + 2\alpha_R)/3}, \quad (2.11)$$

$$\text{and } f_5(\delta, \kappa) = \frac{\kappa^{(2\alpha_a - 1 + 2\alpha_R)/3}}{[1 + \kappa^2 (1 + 2\delta^2 - 1.2\delta^3)]^2}. \quad (2.12)$$

From Eq. (2.9), the ratio $r_{V_m} \equiv V_m(A) / V_m(A = 4)$ of machine volume at any aspect ratio A to that at an aspect ratio $A = 4$, can be derived. It is a function of aspect ratio only *as long as the confinement characteristics (c, H, α_R, α_a), the profiles (γ, γ_n), the impurity dilution (g), the shaping factors (κ, δ), and the operational value of q are aspect-ratio independent.* Note that low- A machines can operate at higher values of κ than can high- A machines without requiring feedback stabilization. This advantage of low A , however, is offset by the difficulty of feedback suppression of $n = 0$ modes at low A , because of the large currents involved.

Figure 2.1 shows r_{V_m} using the accepted values $\alpha_R = 1.75$ and $\alpha_a = -0.37$ (solid line). Reduced volumes are possible for $A < 2$, with significant reductions (greater than 25%) when $A < 1.5$. As A is reduced at fixed q , either $q(0)$, the value on axis, becomes less than unity, or, to avoid this, the plasma current density must peak near the plasma

edge. Such hollow profiles must rely on bootstrap currents and non-inductive current drive. The delineating aspect ratio A_H between peaked and necessarily hollow profiles is the one for which the current-density profile is flat and $q(0) = 1$, *i.e.* where $q_{cyl} \approx 1$ (Eq. (2.7)). Because the shaping parameters (κ , δ) diminish as the magnetic axis is approached, this constraint still permits $q(0) < 1$, or alternatively, hollow current-density profiles. However, this diminution of shaping parameters, leading to lower q on axis or hollow profiles, is considered to be offset by the increased toroidal field from the paramagnetic effect, which increases q on axis or, equivalently, allows flatter profiles. Taking $q_{min} = 3.2$ gives $A_H = 1.38$, and Fig. 2.1 then yields $r_{Vm} = 0.5$. That is, a 50% reduction in machine volume is achieved to obtain a given normalized neutron power.

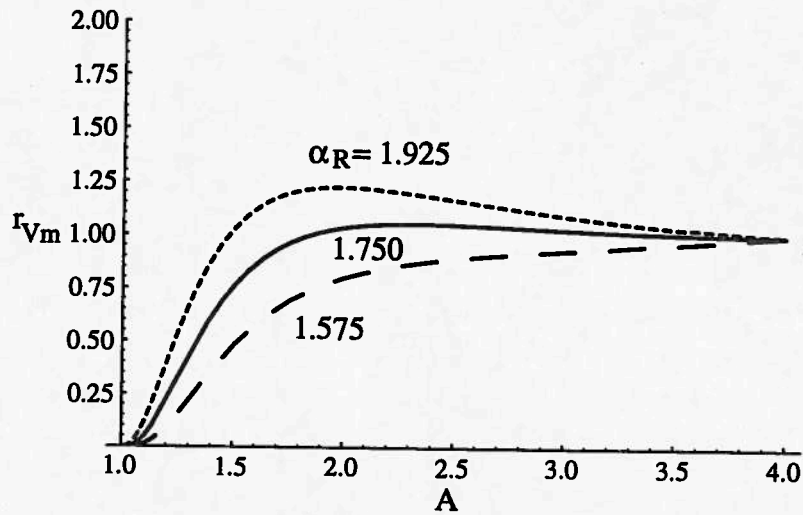


FIG. 2.1. The ratio $r_{Vm} = V_m(A)/V_m(A=4)$ of machine volume V_m to that at aspect ratio $A = 4$ as a function of aspect ratio. Solid line $\alpha_R = 1.75$, short dashes $\alpha_R = 1.925$, long dashes $\alpha_R = 1.575$. $\alpha_a = -0.37$.

Also shown in Fig. 2.1 are the values of r_{Vm} with α_R perturbed by +10% ($\alpha_R = 1.925$, short dashes) and -10% ($\alpha_R = 1.575$, long dashes). The choice of α_R is important, since near A_H , a 10% change in α_R from the accepted value changes r_{Vm} by about 50%. *Clearly the assumed confinement properties are critical*; confinement experiments must be performed in the relevant geometry.

Figure 2.2 shows the sensitivity of r_{Vm} to the assumed minimum safety factor q , again for different values of α_R , for an aspect ratio $A = 1.25$. It is assumed that the normal aspect-ratio case ($A = 4$) is operated with $q = 3.2$. The nominal case ($\alpha_R = 1.75$) permits an advantage at low A (*i.e.* $r_{Vm} < 1$) only if $q < 4.5$. However, the maximum q

that can be tolerated before $r_{Vm} > 1$ is itself critically dependent on α_R , *i.e.* on the confinement properties at low aspect ratio. For example, decreasing α_R by 10% allows this advantage up to $q \approx 5.5$, while increasing α_R by 10% removes any advantage of low A for $q > 3.5$. Again we deduce that confinement experiments in low- A geometry must be performed before predictions about usefully reliable low-aspect-ratio advantages for fusion can be made.

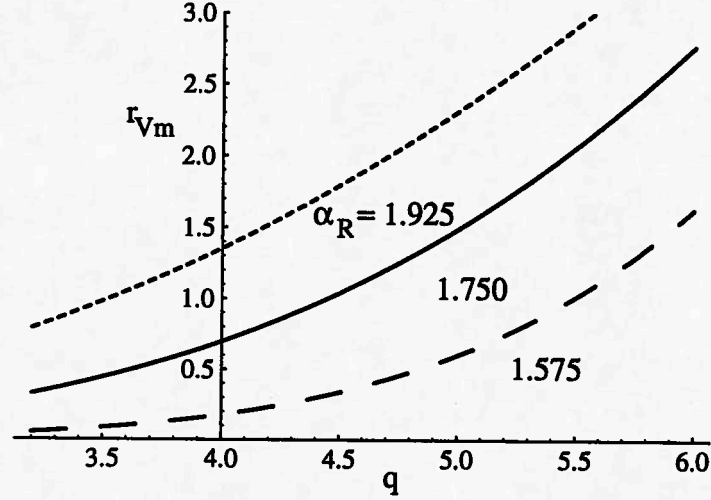


FIG. 2.2. The ratio $r_{Vm} = V_m(A)/V_m(A=4)$ for $A = 1.25$, as a function of assumed minimum q , with three values of α_R . Solid line for $\alpha_R = 1.75$, short dashes for $\alpha_R = 1.925$, long dashes for $\alpha_R = 1.575$.

Plasma current

The reduced machine volume possible at low- A comes at the expense of larger plasma currents. That is, low aspect ratio allows large plasma currents, whose confinement properties offset the loss in confinement time associated with the changed geometry. The resulting expression for $r_{Ip} = I_p(A)/I_p(A=4)$ is a function of aspect ratio for A -independent confinement characteristics (c , H , α_R , α_a), profiles (γ_T , γ_n), impurity dilution (g), shaping factors (κ , δ), and operational value of q . Figure 2.3 shows r_{Ip} increases significantly as A is reduced, and at $A = A_H \approx 1.38$ (below which hollow current profiles are a necessity) $r_{Ip} \approx 4$. Since there is little room for poloidal field coils at the small-major-radius side of the plasma, *current drive becomes a necessity*. Because the gains associated with low A have not considered the power associated with this current, current drive must be at a high (but as yet undetermined) efficiency.

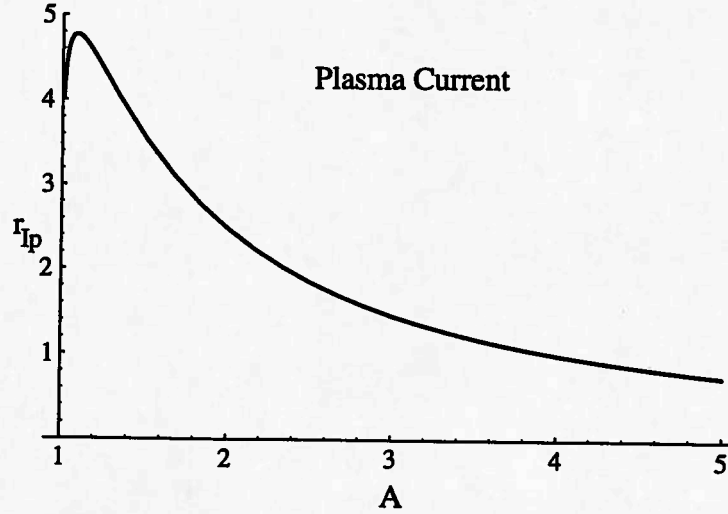


FIG. 2.3. The ratio $r_{Ip} \equiv I_p(A)/I_p(A=4)$ of plasma current at aspect ratio A to that at $A=4$, as a function of aspect ratio, for $\alpha_R = 1.75$, $\alpha_a = -0.37$.

Wall loading

Tokamak reactors suffer from large energy fluxes to material surfaces. In an ignited machine ($Q = \infty$, $F = 1$) the general problem is characterized by the neutron or alpha power per unit first-wall area, or *wall loading*. This ratio is calculated using the surface area of an elliptical plasma, $S \approx 2\pi^2 Ra(1 + \kappa)$, which is the appropriate first-wall area for large A where a blanket surrounds the plasma. At low A there is no blanket at the inner equator, and the area of a spherical shell is more appropriate. However, because the area associated with the inner-major-radial wall becomes vanishingly small as $A \rightarrow 1$, the error introduced by using the elliptical version is small.

With the definitions of pressure $\langle p \rangle = 2k_b \langle nT \rangle$ (k_b is Boltzmann's constant) and beta with respect to the vacuum toroidal field $\beta = 2\mu_0 \langle p \rangle / B_{T0}^2$, and assuming that a limiting value of β independent of aspect ratio exists [4],

$$\beta \leq 10^{-8} \beta_N \frac{I_p(A)}{a(m) B_{T0}(T)}, \quad (2.13)$$

then the alpha particle power can be written as

$$P_\alpha \leq 4.58 \times 10^{-10} \beta_N^2 \frac{g^2 (1 + \gamma_n + \gamma_T)^2}{1 + 2(\gamma_n + \gamma_T)} \kappa R_0 B_{T0}^2 I_p^2. \quad (2.14)$$

Thus, the neutron power $P_n \approx 4P_\alpha$ and the neutron wall load $\Gamma_n \approx 4P_\alpha/S$ are determined. Restrictions are imposed using Eqs. (2.6) and (2.7) for I_p , and Eq. (2.8) for B_{T0} . The major radius R_0 is that of the optimum machine, discussed above. The result is an expression for the maximum neutron wall loading Γ_n . The ratio $r_{\Gamma_n} \equiv \Gamma_n(A)/\Gamma_n(A=4)$ is a function of aspect ratio only as long as the remaining parameters are aspect-ratio independent.

Figure 2.4 shows r_{Γ_n} against A . The advantage of high aspect ratio ($A > 4$) is apparent. At the point $A_H = 1.38$ (i.e. a flat current profile) then $r_{\Gamma_n} \approx 1.5$, that is, worse than the standard $A = 4$ case. However, $r_{\Gamma_n} < 1$ for $A < 1.25$.

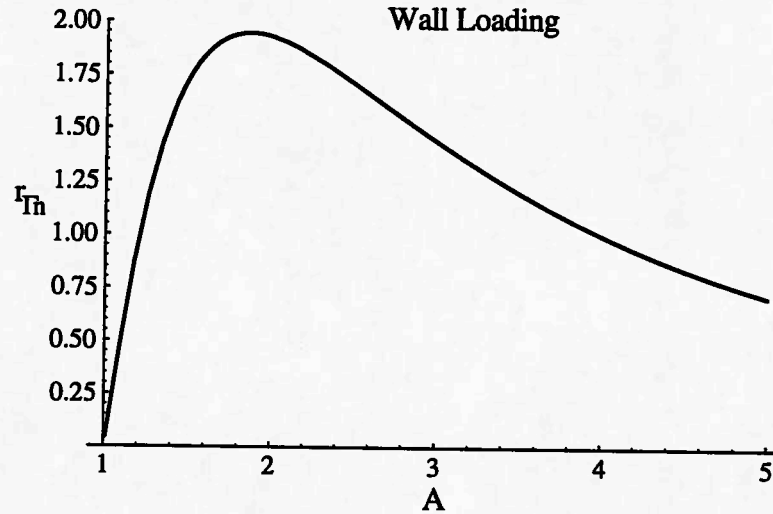


FIG. 2.4. The ratio $r_{\Gamma_n} \equiv \Gamma_n(A)/\Gamma_n(A=4)$ of neutron wall loading at aspect ratio A to that at aspect ratio $A = 4$, as a function of aspect ratio, for $\alpha_R = 1.75$, $\alpha_a = -0.37$.

The maximum β_N , restricted by wall loading, increases with increasing confinement time. This is because $\Gamma_n \propto V/S \propto a \propto R_0$ at fixed A ; increasing confinement allows a smaller R_0 , and thus (see Eq. (2.14)) a higher β_N for a given loading. For the scalings assumed here, $\beta_{N\max} \propto (P_n/S)_{\max}^{1/2} \propto H^{1/2}$. Figure 2.5 shows the values of $\beta_{N\max}$ as a function of H , restricted by $P_n/S = 5 \text{ MW/m}^2$, for the smallest possible ignition machines at different values of A . Conditions taken are $q = 3.2$, $B_{T\max} = 13 \text{ T}$, $g = 0.9$, $\gamma_n = \gamma_T = 0.5$, $\kappa = 2$, and $\delta = 0.3$. (Remember that $B_{T\max}$ is the value at the inner TF leg.) We see that for these 'smallest high-yield machines' $\beta_N \leq 3$, i.e. presently attained values are sufficient.

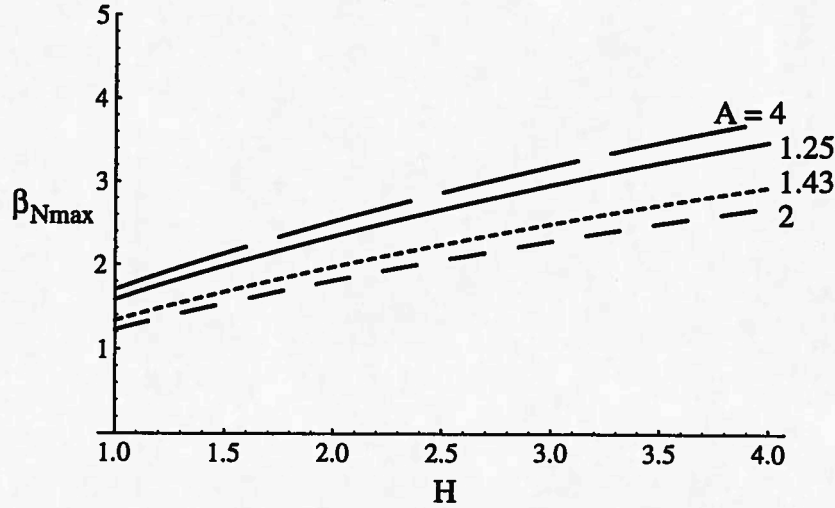


FIG. 2.5. The maximum normalized beta β_{Nmax} possible as a function of the confinement improvement factor H , restricted by neutron wall loading of 5 MW m^{-2} . Other conditions are given in the text. Results are shown for $A = 1.25, 1.43, 2$, and 4 .

Toroidal field production

The simple analysis presented above shows that gains (in allowing a smaller machine-encompassing volume) can be achieved in principle by using low aspect ratio. In particular the smallest ignition machine is provided by the largest toroidal field. In what has been presented so far a simple maximum toroidal field B_{Tmax} at the toroidal field (TF) leg surface at $R_0 - a$ has been assumed, with no account taken of any nuclear blanket thickness, or of any power dissipated in the TF leg. Here two more realistic cases are presented:

- 1) a superconducting TF coil (no power dissipated) with a nuclear blanket of thickness w , and
- 2) a normal copper coil with associated power dissipation, but no blanket.

Superconductor TF coils

For the superconducting case with blanket thickness w_b we replace Eq. (2.8) by

$$B_{T0} = B_{Tmax} \frac{(A-1)}{A} \left(1 - \frac{w_b A}{R_0 (A-1)} \right). \quad (2.15)$$

Then the expression for the minimum major radius R_0 is given by

$$R_{sc} \approx \left(\frac{Fq^2}{\lambda B_{Tmax}^2 f_1(A) f_3(\delta, \kappa)} \right)^{1/(2\alpha_R - 1 + 2\alpha_p)} + \frac{w_b A}{(A-1)}. \quad (2.16)$$

Copper TF coils

Here we consider the constraints imposed by the power required to produce the toroidal field using copper coils. No nuclear blanket is considered; easy TF coil replacement is assumed. For a central TF leg of height $2\kappa a$ and radius at the equator $R_0 - a$, the power consumed in producing the toroidal field is

$$P_{TF} = \frac{8\eta \pi \kappa B_{Tmax}^2 R_0}{\mu_0^2 f_{Cu} A} \left[1 - \exp(-1.3\omega\sqrt{A-1}) \right]. \quad (2.17)$$

The power consumption in the outer TF legs is assumed negligible, because these can be made with as large a cross section as is necessary. The parameter f_{Cu} represents the conducting fraction of the TF leg area (assumed independent of height), the remaining fraction being used for cooling. The function $\left[1 - \exp(-1.3\omega\sqrt{A-1}) \right]$ describes the reduced TF leg resistance possible if the full central aperture is used; $\omega = 1$ for a plasma with an elliptic cross section, and $\omega = \infty$ for a triangular plasma ($\delta = 1$). We assume that it is possible to remove the heat generated in the TF leg by water cooling, and that in so doing the resistivity is given by $\eta \approx 2 \times 10^{-8} \Omega - m$. A working constraint is that the power P_{TF} should be a small fraction of the total electric power of the reactor; we write the recirculating power fraction as

$$\chi = \frac{P_{TF}}{P_{el}} = \frac{P_{TF}}{f_{el} P_n}, \quad (2.18)$$

where we assume a futuristic $f_{el} = 0.4$ efficiency of conversion from neutron power to electricity. We also assume all neutrons produced can be utilized towards producing electricity. Two limits to P_n are now considered: a wall loading limit and a beta limit.

Wall loading

Material availability restricts the possible neutron power per unit surface area to values $\Gamma_n = P_n / S \leq \Gamma_{n0} < 5 \text{ MWm}^{-2}$. This imposes a maximum neutron power P_n ,

and thus with P_{TF} defines a recirculating power fraction χ . The toroidal field can then be expressed in terms of χ . Finally an expression for the major radius R_Γ results, which is the major radius of the smallest machine possible to achieve a specified value of F and χ at a specified aspect ratio A , with the assumed values of safety factor q , geometry κ and δ , confinement parameters c and H , impurity content g , profile factors γ_n and γ_T , restricted only by the wall loading Γ_{n0} :

$$R_\Gamma = \left[\frac{1.92 \times 10^{-6} \pi \eta F q^2 [1 + 2(\gamma_n + \gamma_T)] (1 - e^{-1.3\omega\sqrt{A-1}}) \kappa}{\mu_0^2 \chi f_{el} f_{Cu} \Gamma_{n0} c^2 H^2 g^2 (1 + \gamma_n + \gamma_T)^2 f_1(A) f_3(\delta, \kappa) (1 + \kappa)} \right]^{\frac{1}{2\alpha_R + 2\alpha_a}} \quad (2.19)$$

β_N limit

If β_N is the restricting parameter, then the associated major radius R_{β_N} is found to be

$$R_{\beta_N} = \left[\frac{1.39 \times 10^{17} \eta c^2 H^2 (1 - e^{-1.3\omega\sqrt{A-1}}) A^7 (A-1)^{-2} A^{-(4+2\alpha_a)}}{48\pi^2 \beta_N^2 \chi f_{el} f_{Cu} F} \right]^{\frac{1}{3-2\alpha_R-2\alpha_a}} \quad (2.20)$$

Results

We use the values of various parameters given in Table 2.1. Figure 2.6 shows the machine encompassing volume V_m as a function of aspect ratio A , for the copper coil model with $\chi = 0.1$, $\chi = 0.25$, and $\chi = 0.5$, the simple model with $B_{T\max} = 13$ T ('simple'), and the superconducting model with $B_{T\max} = 13$ T ('sc'). The β_N limit restricts the copper coil model R_0 and V_m at the lowest and highest A , with the wall loading limit restricting at intermediate A . The optimum device is where these two limits are equal, and occurs for $A \approx 1.2$. It is not possible to construct an exothermic tokamak reactor with lower aspect ratio.

Table 2.1. Values used in the examples

parameter	value
q	3.2
γ_n	1
γ_T	1
g	0.9
c	3.7×10^{-5}
H	3 (VH mode)
F	1 (Ignition)
κ	2
δ	0.3
α_a	-0.37
α_R	1.75
Γ_{n0} (Wm^{-2})	5×10^6
β_N	5
f_{el}	0.4
f_{Cu}	0.7
η ($\Omega\text{-m}$)	2×10^{-8}
χ	0.1, 0.25, 0.5
ω	1, ∞

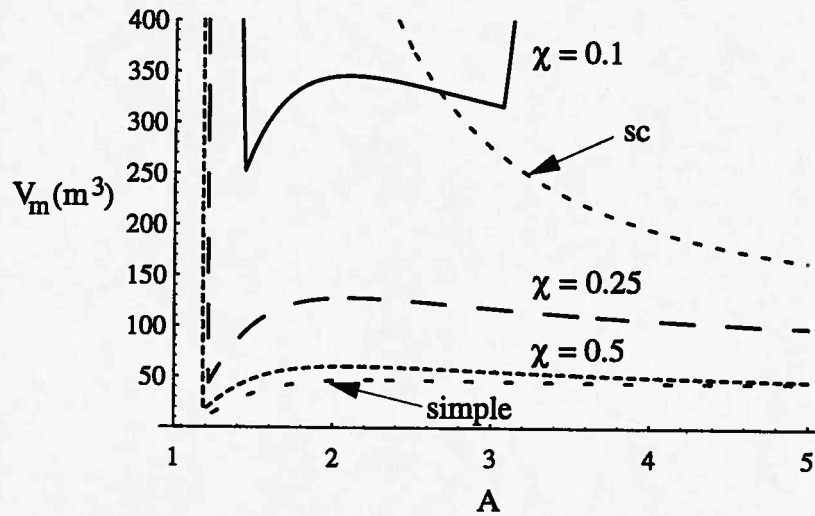


FIG. 2.6. The machine-encompassing volume V_m as a function of aspect ratio A for different recirculating power fractions χ . Solid line $\chi = 0.1$, broken line $\chi = 0.25$, dotted line $\chi = 0.5$. Other values are found in Table 2.1. Also shown are values for the simple model with $B_{T\max} = 13$ T ('simple'), and the superconducting case with $B_{T\max} = 13$ T ('sc').

Advanced fuels

The central toroidal-field-coil leg has particular problems, because the conductor (*e.g.* copper) cannot be shielded from neutrons if low A is required. Neutron damage is measured in displacements per atom (dpa), and a D-T neutron flux of 10 MW/m^2 for one year is approximately equivalent to 150 dpa. For copper and its alloys the neutron-induced swelling is highly temperature sensitive. Values less than 10 dpa are recommended, although no data at high dose ($> 5 \text{ dpa}$) exist [5]. At a continuous 5 MW/m^2 , a copper central conductor would need to be replaced at least every 2 months.

The use of D-He³ fuel has been suggested (see [6, 7] and references therein), with a consequent reduction in neutron flux and associated damage. Direct conversion is then required [8]. Two effects, the reduction (with respect to D-T) of the reaction cross section, partially offset by an increase in the energy retained by the plasma due to improved confinement of reaction products (which are all charged), lead to a decrease in the ratio F in Eq. (2.2) by a factor of 10 to 20. Repeating the analysis above leads to the conclusion that larger devices with higher currents are required for D-He³ than for D-T machines. For example, if I_p were not increased, a D-He³ machine volume would have to be a factor of 100 larger than the corresponding D-T machine with similar output. Optimization for D-He³ devices which include energy accounting for the driven and bootstrap current lead to an optimum aspect ratio $A \approx 2$.

Conclusions

The case study of the machine parameters required to achieve a certain Q as a function of aspect ratio was made tractable by means of certain assumptions. In particular, it was assumed that the inner toroidal field leg occupies no space at the inner equator, the costs of maintaining the plasma current were not considered, and initially the costs of producing the toroidal field were ignored. The results then show that much smaller (less than 50 % by volume) ignited plasmas can be built at low aspect ratio ($A \approx 1.3$) than at normal aspect ratio ($A = 4$). The penalty is that an externally and bootstrap-driven plasma current must be provided that is approximately four times that at normal aspect ratio.

Some important values of A are implied. Below $A = A_H \approx 1.4$ hollow current density profiles are a necessity (if $q(0) > 1$). Including the power to provide the toroidal field restricts $A > 1.2$. To reduce the wall loading at maximum beta to that of the

standard $A = 4$ case, $A < 1.25$ is required. However, published studies for D-He³ machines which include the energy cost of current drive conclude that $A \approx 2$ is optimum. Note: the higher aspect ratio dictated for D-He³ also easily meets the constraint $A > 1.25$ required by TF post considerations described earlier.

The results depend critically on the stability and confinement properties of the low- A plasmas. Sensitivities to the assumed lowest q , and to the scaling of confinement with geometry, are significant. For this reason the relative fusion advantages of low aspect ratio need to be tested.

2.2 System studies: desirable properties at low aspect ratio

Here we discuss some properties of low-aspect-ratio tokamaks that would be *desirable* (if not necessarily *achievable*), if they are to contribute to engineering progress in fusion. Engineering and cost constraints suggest the physics results that would allow viable next steps toward power plants, neutron sources, or divertor test facilities. These properties partially determine the research on USTX, leading to a list of experiments to be performed. This work has been performed by our colleagues at ORNL [9-11].

Power plant

First we consider properties which have been *assumed* in designing low- A tokamak power plants, together with the present standard-aspect-ratio tokamak data and the most advanced physics projections of high aspect ratio (see Ref. [10]). Data derived using SUPERCODE [12] is given in Table 2.2 in which λ_p is the pressure e-folding thickness, and Δ_{SOL} is the scrape-off layer thickness for heat flux.

Modest external field and high plasma current in small size are properties of low aspect ratio that lead to reduced weight and capital cost for the fusion power source. Strong plasma shaping, high steady-state confinement, and high stable beta ensure ignition capability in a small tokamak plasma. Normal-conducting toroidal-field coils that dissipate power become acceptable under these conditions. Effective non-inductive startup to the full plasma current would eliminate the need for an inboard solenoid and contribute to lowering the aspect ratio. High self-driven current and efficient current drive minimize the external current drive and recirculating power. A thick scrape-off

layer (SOL) mitigates the challenge of high divertor heat flux. The absence of disruptions and a simplified fully de-mountable configuration would make the development of reliable and maintainable fusion devices more likely.

Table 2.2. Desirable Low-A Properties for Economic Power Production.

Tokamak Power Source Properties (aspect ratio)	Parameters or Features (R_0/a)	Present Best Data (2.5–3.5)	Advanced High-A (4.5)	Desired Low-A (1.1–1.3)
Modest external fields	I_p/I_{tf}	0.2	0.04	1–3
	I_p/I_{pf}	0.2	0.1	1
High current in small size	I_p/aB_{T0} (MA m ⁻¹ T ⁻¹)	2	1	~10
Strong plasma shaping	$I_p q/aB_{T0}$ (MA m ⁻¹ T ⁻¹)	10	4	~100
High steady-state confinement	H (ITER power law)	2.5	4	~4
High stable toroidal beta	$\langle\beta\rangle \equiv 2\mu_0\langle p\rangle/B_{t0}^2$	0.1	0.06	~0.3–1
High normalized beta	$\beta \equiv \langle\beta\rangle aB_{T0}/I_p$	3.0	5.0	~5–10
Non-inductive startup	$\Psi_{OH}/L_p I_p$	0	0	0
Non-inductive current drive	$\gamma_{CD} (\equiv I_{CD}R_0\langle n_e\rangle/P_{CD})$	0.3	0.3	0.3
High self-driven current	I_{self}/I_p	≤ 0.85	≥ 0.9	≥ 0.9
Thick scrape-off layer	$\lambda_p = \Delta_{SOL}/3$ (cm)	2	2	~10
Free of disruption	disruption probability	small	small	zero
Adequate maintainability	jointed TFC	no	no	yes

The above properties, when assumed in systems-code calculations of reactor parameters and economics lead to improvements in the potential competitiveness of tokamak fusion power. Table 2.3 summarizes the best projected capital cost and cost of electricity (COE), assuming an ITER-like costing approach in 1993 dollars, for the three cases of Table 2.1, each producing a net electricity of 1000 MWe. The low-aspect-ratio tokamak option further uses a single-turn Cu center leg for the toroidal field coil, eliminating inboard induction solenoid, insulators, and shielding. Non-inductive initiation and ramp-up of full plasma current is therefore required. Blanket, first wall, divertors, and Cu center leg for low aspect ratio are replaced regularly and treated as fuel cost. The best-experience pressurized-water fission reactor (PWR) producing a net electricity of 1200 MWe is included for comparison.

Table 2.3. Power source parameters and cost components, compared with the best-experience pressurized-water fission reactor (PWR).

	Present Best Data	Advanced Physics High-A	Economy Driven Low-A	Best PWR
Normalized average toroidal beta β_{Nr}	3.5	5.0	5.8	N/A
Average toroidal beta $\langle\beta_T\rangle$	0.055	0.046	0.44	N/A
Steady-state confinement H -factor	1.7	2.5	2.4	N/A
Plasma (core) size $R_0 + a$ (m)	8.5	7.3	5.4	~2.5
Aspect ratio R_0/a	2.8	4.5	1.2	N/A
Toroidal field at R_0 (T)	5.6	7.0	2.4	N/A
Plasma current I_p (MA)	19.8	8.5	43.0	N/A
Fusion neutron wall loading (MW/m ²)	2.6	3.4	6.0	N/A
Power core mass (ktonne)	30.8	22.9	9.7	~2
Core mass power density (kWe/tonne)	32.4	43.7	103.3	~600
Total capital cost (\$B)	7.48	5.28	3.62	2.66
Balance of plant cost (\$B)	2.09	1.80	1.77	1.81
Power source equipment cost (\$B)	5.39	3.48	1.85	0.85
Total cost of electricity (¢/kW-hr)	14.78	10.81	8.43	6.12
Capital investment (¢/kW-hr)	12.69	8.95	6.15	4.23
Operation and maintenance (¢/kW-hr)	1.06	1.06	1.06	1.03
Fuel (¢/kW-hr)	1.03	0.80	1.23	0.86
blanket and first wall (¢/kW-hr)	0.73	0.61	0.74	0
divertors (¢/kW-hr)	0.19	0.09	0.14	0
copper TFC center leg (¢/kW-hr)	0	0	0.25	0
tritium or uranium (¢/kW-hr)	0.06	0.06	0.06	0.80
waste handling (¢/kW-hr)	0.05	0.05	0.05	0.06

The COE varies widely among these four cases, due primarily to variations in the capital investment (cost of money) for the total capital cost of the power plant. The capital cost is itself dominated by the cost of power-source equipment (tokamak and support systems). The economy of tokamak fusion therefore depends *first* on attractive plasma physics properties that minimize the cost of the power source equipment, and *second* on the device physics and configuration features that permit adequate

maintainability and reliability for sustained power production. It is seen that low aspect ratio could lead to the most attractive tokamak power plant. Its direct cost would be about \$1B higher, and its COE about 2 ¢/kW-hr higher, than the best-experience PWR power plant, but it is significantly cheaper than the best envisioned conventional-A tokamak reactor.

High-volume plasma neutron source (HVPNS)

Another objective for low-aspect-ratio tokamaks is to make a high-volume plasma neutron source (HVPNS) for testing materials and power-producing blankets [9]. Proposed (i.e. *assumed possible*) parameters are listed in Table 2.4 [13], and contrasted with those of ITER. It is seen that the low-aspect-ratio tokamak can offer a cost-effective approach for a HVPNS because of small size and modest requirements in tritium, fusion, and power consumption, while providing adequate neutron wall load and first-wall area for testing. The key physics and engineering issues for a low-aspect-ratio HVPNS are similar to, but more modest than, those desired for competitive energy production. The D-T physics performance of the HVPNS is expected to be defined by $Q \sim 1$; steady-state operation is not required.

Divertor test facility

Because the natural divertors for low aspect ratio are located significantly inboard of R_0 ($R_{div} \sim 0.2 - 0.3$ m), high divertor heat flux can be produced without requiring large auxiliary heating power. Given that a long divertor channel (~ 1 m) is also provided, a 1 MA-level device would become useful for testing ITER-relevant or equivalent divertor concepts. A comparison of the divertor power flux factor (P/R_{div}) for a single-null natural divertor in the low-aspect-ratio experiment with the advanced divertors in DIII-D and JET is provided in Table 2.5. It is seen that a low-aspect-ratio experiment at the MA-level, using a heating power of 3–10 MW, will have the ability to achieve values for (P/R_{div}) similar to those anticipated in ITER.

Table 2.4. Design options for a high-volume plasma neutron source, compared with ITER (taken from Table C-III of [13]).

	ITER EDA	Super Conductor	Normal Conductor Standard A	Normal Conductor Low A
Neutron wall load (MW/m^2)	1	1	1–2	1–2
Normalized toroidal beta β_{Nt}	2.0	2.5	2.5	3.0
Steady-state confinement H -factor	2.1	2.5	2.5	2.5
Inboard shield (m)	1.2	0.72	0.23	0.03
Plasma size R_0+a (m)	11.1	4.7	2.8	1.4
Aspect ratio R_0/a	2.7	4.4	2.5	1.3
Toroidal field at R_0 (m)	5.7	7.7	4.3–5.5	2.0–2.4
Plasma current (MA)	24	6.4	9–11	9.4–10.4
Plasma drive power (MW)	0	140	60–90	19–29
Fusion power (MW)	1500	360	120–260	32–65
Steady-state power consumption (MW)	200	330	540–700	130–180
First wall area (m^2)	1300	290	100–107	26

Table 2.5. Comparison of anticipated divertor power flux parameters for ITER, DIII-D, JET, and a low-A tokamak experiment such as USTX (Phase II).

	ITER	DIII-D	JET	Low-A
Major radius R_0 (m)	8.1	1.6	3.0	0.7–0.8
Divertor channel radius R_{div} (m)	8	1.5	2.8	0.2–0.3
Aspect ratio R_0/a	2.7	2.5	2.5	1.2–1.5
Field at divertor (T)	6	2	2.5	1.0–2.0
Plasma current (MA)	24	2	5	0.5–1
Plasma heating power (MW)	300	25	50	3–10
Divertor power flux factor	38	17	18	15–50
P/R_{div} (MW/m)				

2.3 Critical questions to be addressed on USTX

The analysis and comparisons presented in Secs. 2.1 and 2.2 show that the following questions and experimental goals are critical. All can be addressed on USTX, although the full exploration of questions 3, 4, and 9 probably requires the addition of a neutral beam, as envisioned in Phase II. The full exploration of question 6 requires first the development of relevant theory, followed by low power tests, before full power current drive can be implemented in Phase II. Most importantly, whether low-A tokamaks are worth pursuing as fusion devices depends on the confinement properties of such machines; these properties are unknown.

1. Can plasmas whose confinement is dominated by physics at low aspect ratio be operated at $A \approx 1.4$ and $A \approx 1.25$? We note that no existing machine meets this criterion, as existing devices have less than 10% of their confinement volume at low A .
2. What operating regimes are available? In particular, what current density profiles can be achieved? What is the lowest possible q for operation?
3. What are the confinement properties at low A ? In particular, what is the scaling of energy confinement with A , what gains over L mode can be achieved, what pressure-profile peaking factors can be achieved, and what impurity accumulation effects exist? How do these compare with those at normal A ?
4. What is the maximum permissible β at low A , and how does it compare with the normal- A case? Are values of $\beta_N \approx 3 - 5$ attainable?
5. What fraction of the plasma current can be maintained by bootstrap current?
6. What external current-initiation and current-drive scenarios can be used, and with what efficiency?
7. Can low-aspect-ratio tokamaks be operated disruption-free at low q ?
8. Can wide scrape-off layers be produced?

9. Can high confinement, high beta, low safety factor, large bootstrap-current fraction, and high current-drive efficiency be obtained simultaneously?
10. Can a machine such as USTX be used as a divertor test facility?

References to Chapter 2

- [1] R. J. Goldston, *Plasma Phys. Controlled Fusion* **26** (1984) 87.
- [2] S. M. Kaye, C. W. Barnes, M. G. Bell, *et al.*, *Phys. Fluids B* **2** (1990) 2926.
- [3] Y.-K. M. Peng and D. J. Strickler, *Nucl. Fusion* **26** (1986) 769.
- [4] F. Troyon, R. Gruber, H. Saurenmann, *et al.*, *Plasma Phys. Controlled Fusion* **26** (1984) 209.
- [5] *Fusion Materials, Semiannual Progress Report for the Period Ending March 31, 1994*, Report DOE/ER-0313/16, pages 313-368, The U. S. Department of Energy (1994).
- [6] *Proceedings of the Second Wisconsin Symposium on Helium-3 and Fusion Power*, Report WSCAR-TR-AR3-9307-3, The University of Wisconsin, College of Engineering (1994).
- [7] B. B. Kadomtsev and V. I. Pistunovich, in *Research Trends in Physics: New Ideas in Tokamak Confinement* (La Jolla International School of Physics, The Institute for Advanced Physics Studies), edited by V. Chan, N. Fisch, V. E. Golant, *et al.*, (American Institute of Physics, New York, 1994), p. 55.
- [8] J. Santarius, J. P. Blanchard, G. A. Emmert, *et al.*, *Energy Conversion Options for ARIES-III – a Conceptual D-He³ Tokamak Reactor*, Report UWFD-815, The University of Wisconsin, Fusion Technology Institute (1989).
- [9] Y.-K. M. Peng, J. D. Galambos, and P. C. Shipe, *Fusion Tech.* **21** (1992) 1729.
- [10] Y.-K. M. Peng, ITC6, *Fusion Tech.* (1995) to be published.
- [11] Y.-K. M. Peng, D. J. Strickler, and J. Galambos, personal communication (1995).
- [12] S. W. Haney, W. L. Barr, J. A. Crotinger, *et al.*, *Fusion Tech.* **21** (1992) 1749.
- [13] M. Abdou, S. Berk, S. Booth, *et al.*, *Phase 1 Report of the IEA Study on High Volume Plasma Based Neutron Source (HPVNS)*, Report UCLA-FNT-94, UCLA-ENG-95-111, UCLA (1994).

CHAPTER 3

PHYSICS OF LOW-ASPECT-RATIO TOKAMAKS

The USTX program will allow us to explore the continuum leading from normal tokamak operation to the low-aspect-ratio limit. Thus, we will be able both to investigate the unique features and advantages of low- A tokamaks and to help elucidate general tokamak physics. In this chapter we discuss this physics, beginning in Sec. 3.1 with the basic effects that distinguish low A from high A . Then, under each major topic in Secs. 3.2 to 3.6 we discuss both the implications for tokamak performance and the opportunities for basic research on USTX. By extending studies of stability and transport to low aspect ratio, we will both enlarge our understanding of these basic phenomena and further define the reactor potential of the low- A regime.

3.1 Basic issues

Toroidal field variation

Nearly every distinguishing feature of the low-aspect-ratio tokamak results from the variation of the toroidal magnetic field with major radius,

$$B_T = F(\psi) / R, \quad (3.1)$$

where $F(\psi)$ is a slowly varying function of the flux coordinate. On a flux-surface $B_T(r, \theta) \propto (1 + \varepsilon \cos \theta)^{-1}$, where $\varepsilon = r / R_0$. (For this simple discussion, we take r to be a flux label denoting the horizontal radial distance to a flux surface, and θ to be a poloidal angle-like variable.) As $\varepsilon \rightarrow 1$ the toroidal-field variation on a flux surface becomes extreme,

$$B_T(r, 0) / B_T(r, \pi) = (1 + \varepsilon) / (1 - \varepsilon) \xrightarrow{\varepsilon \rightarrow 1} \infty. \quad (3.2)$$

At the plasma edge this ratio is 5.7 or 9.0 for $A = 1.43$ or $A = 1.25$, respectively. As we emphasize throughout, this implies strong poloidal asymmetries of most physical quantities, e.g., the local toroidal current density (Sec. 5.8).

On the other hand, the poloidal field,

$$B_p = |\nabla\psi|/R, \quad (3.3)$$

remains finite and its low to high-field-side ratio is of order unity, since the plasma current density is everywhere finite. That is, $|\nabla\psi| = (\partial\psi/\partial r)|\nabla r|$ should itself vary as R , with corrections of order unity. To illustrate the effects of low A we will assume constant poloidal field on the flux surfaces, $B_p(r, \theta) = B_p(r)$. To simplify the figures we map this elementary model, extended to include ellipticity and triangularity, onto concentric surfaces. Of course, with real equilibria, especially at high β , we will have to take into account the radial dependence of the Shafranov shift and the variation of B_p with θ .

Many quantities entering any theory then depend on two flux-surface averaged dimensionless quantities, denoted, in the notation of Howe [1], by

$$c_\phi \equiv \langle B_T^2 \rangle \frac{R_0 V'}{4\pi r^2 F^2} = \frac{R_0 V'}{4\pi r^2} \left\langle \frac{1}{R^2} \right\rangle, \quad (3.4)$$

$$c_\theta \equiv \langle B_p^2 \rangle \frac{R_0 V'}{4\pi r^2 \psi'^2} = \frac{R_0 V'}{4\pi r^2} \left\langle \frac{|\nabla r|^2}{R^2} \right\rangle, \quad (3.5)$$

where $\psi' = \partial\psi/\partial r$, $V' = \partial V/\partial r = \oint dl/B_p$ is the radial derivative of the volume enclosed by r , and $\langle \dots \rangle = \oint dl \dots / B_p / V'$ here represents the flux-surface average. The normalization is chosen to yield convenient values of order unity for normal aspect ratio.

Note that at low aspect ratio c_ϕ varies much more strongly with radius than c_θ . In our model (with zero triangularity) we find that $V' = 4\pi^2 \kappa r R_0$,

$$c_\phi(r) = \kappa / (1 - \varepsilon^2)^{3/2}, \quad (3.6)$$

$$c_\theta = (1 + \kappa^2) / 2\kappa. \quad (3.7)$$

These enter, for example, into the equation for the resistive evolution of the current or poloidal flux [1]. See Blum and Le Foll [2], Pfeiffer *et al.* [3], and Hogan [4] for alternative notations.

The most obvious manifestation of the strong variation of B_T is in the variation of the field pitch on a surface and the strong increase in the safety factor $q(\psi)$. (Recall that

we denote by q what is often labeled q_ψ .) In our model the safety factor (again with zero triangularity) is given by

$$q(r) = \frac{c_\phi(r)}{\kappa} q_{\text{cyl}}(r) = \frac{q_{\text{cyl}}(r)}{(1-\varepsilon^2)^{3/2}}, \quad (3.8)$$

with

$$q_{\text{cyl}}(r) = c_\theta \kappa q_{\text{cir}}(r) = \left(\frac{1+\kappa^2}{2} \right) q_{\text{cir}}(r) = \left(\frac{1+\kappa^2}{2} \right) \frac{2\pi r^2 B_{T0}}{\mu_0 R_0 I_p(r)}, \quad (3.9)$$

where κ is the elongation, B_{T0} is the toroidal field at the magnetic axis R_0 and $I_p(r)$ is the plasma toroidal current contained within the radius r . In the spheromak limit, $\varepsilon \rightarrow 1$, the true safety factor would actually diverge as $(1-\varepsilon^2)^{-2}$ rather than $(1-\varepsilon^2)^{-3/2}$, because an ellipsoidal separatrix forms intersecting the major axis [5, 6]. This is unimportant for the range of A considered for USTX; Eq. (3.8) agrees well over this range with the empirical formula $q = q_{\text{cyl}} (1.22 - 0.68\varepsilon)(1-\varepsilon^2)^{-2}$ of Peng and Strickler [6], which we use elsewhere (e.g. chapter 2). (Numerical equilibria at high β yield somewhat lower values of q [7]). Equation (3.8) also yields the correct limit as $\varepsilon \rightarrow 0$ which we will need for profile considerations. Figures 3.1a,b show the field-line behavior at $A = 1.25$, one of the point-design values for USTX (Phase II). In Fig. 3.1a, $q = 10$ with $q_{\text{cyl}} \approx 2.4$, while in Fig. 3.1b, $q = 3$ with $q_{\text{cyl}} \approx 0.65$. The field line has a steep pitch at the outside of the torus, while wrapping strongly about the central core [6].

Implications

These considerations have at least two sets of implications. First, they complicate all estimates, extrapolations, and theoretical calculations. Clearly we cannot trust any argument based on the high-aspect-ratio or small- ε expansion. Any expansion in toroidal/poloidal (n/m) harmonics is also suspect. (The large n ballooning theory should survive, however, provided the metrics are estimated properly in the transformation.) All trapped-particle and neoclassical effects must be re-examined, including the fraction of trapped particles, mean curvature drifts, transit times, mode ballooning, and effective collisionalities. Further, since the dependence on I_p or q of empirically determined scalings has not been explored at small A , we do not know for certain which is the relevant parameter for any extrapolation, or whether other aspect-ratio terms will enter. We must make educated guesses based on limited numerical and experimental evidence.

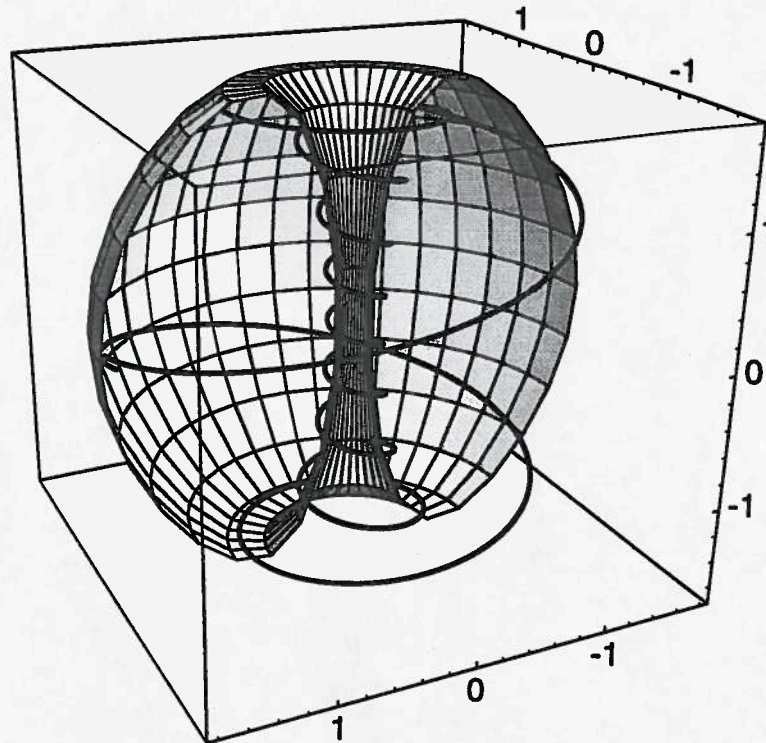


FIG. 3.1a. Field line for $q = 10$, $A = 1.25$, $\kappa = 2.0$, $\delta = 0.3$.

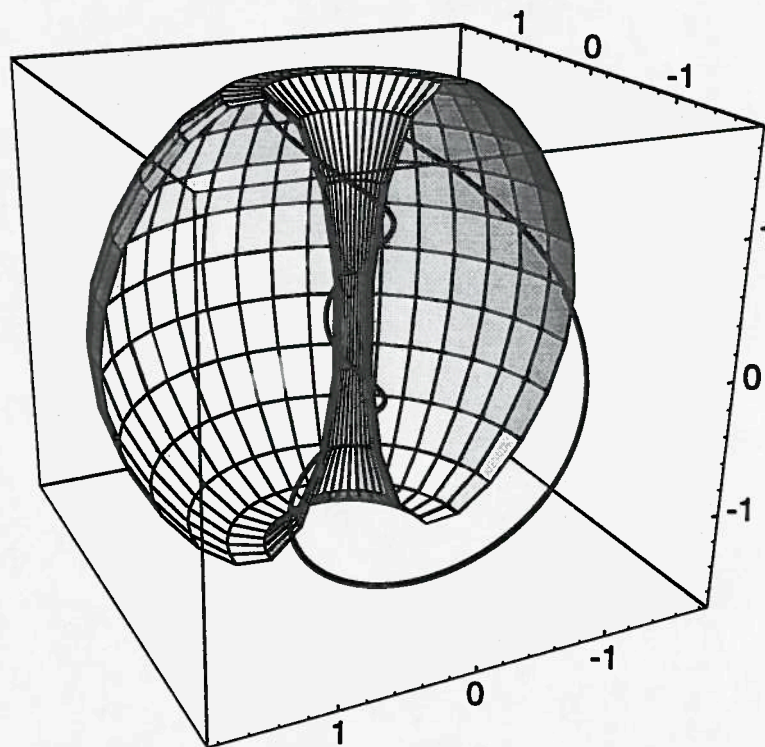


FIG. 3.1b Field line for $q = 3$, $A = 1.25$, $\kappa = 2.0$, $\delta = 0.3$.

Second, the ε -dependence of q raises questions about how to achieve desired operating regimes. Note from Eq. (3.9) that the plasma current $I_p(r)$ and therefore the current density $j(r)$ is more closely associated with q_{cyl} than with q . This means that operation at moderately low q while still keeping $q(0) > 1$ will require the maintenance of a hollow current profile. This is illustrated, for our model, in Figs. 3.2a,b, where a "normal" q -profile yields a decreasing $q_{cyl}(r)$ and therefore a rising $j(r)$ in the core.

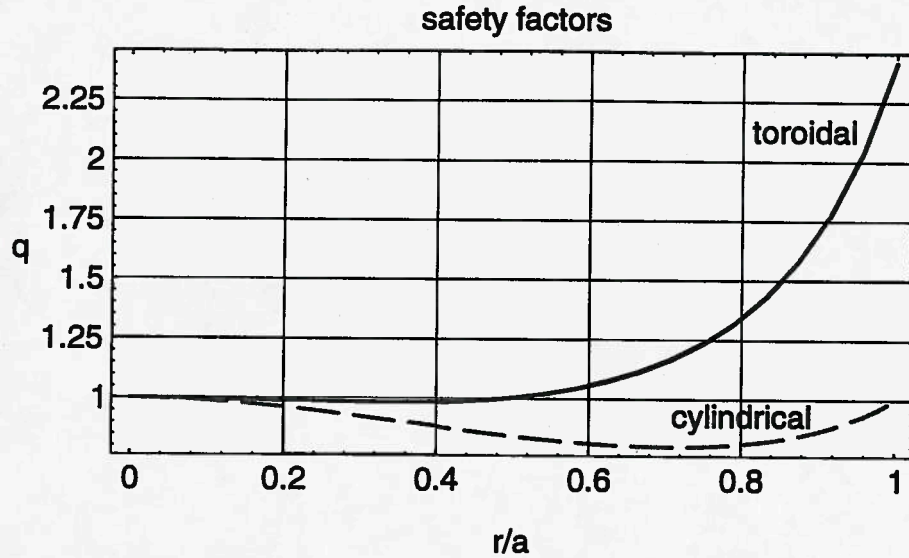


FIG. 3.2a. q vs. minor radius for a low- q case with $A = 1.5$.

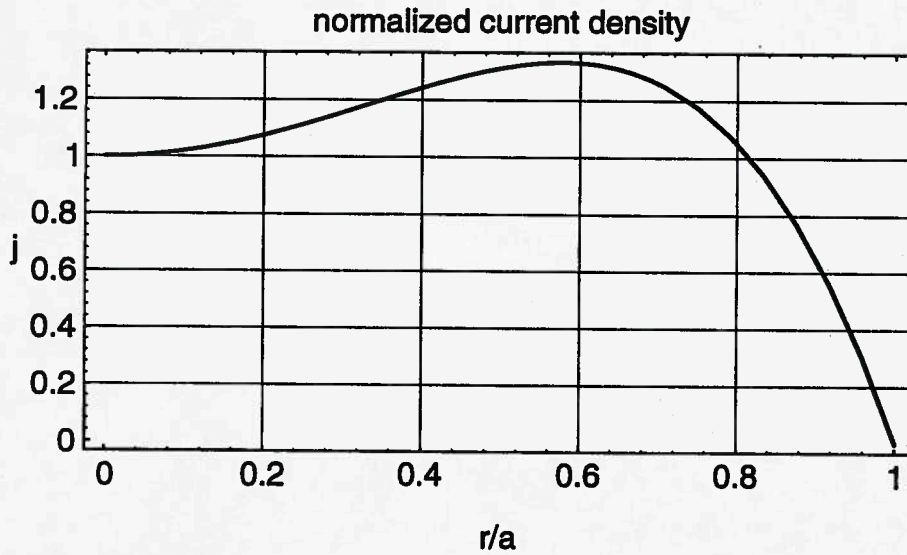


FIG. 3.2b. j vs. minor radius for the same case as 3.2a.

More extreme examples of this requirement are found when we consider high- β , high bootstrap-current, or reversed shear regimes [7]. On the other hand, for normal $j(r)$ profiles, $q(0)$ falls well below unity, suggesting that large modes with $n/m = 1/1$ will be driven in practice (coupled to $m = 2, 3, 4, \dots$). Whether these lead to benign sawteeth or harmful disruptions needs to be investigated.

The shape of $F(\psi)$ in Eq. (3.1) will also affect the q profile. Tokamaks are paramagnetic, $F(\psi_{\text{axis}}) > F(\psi_{\text{edge}})$ if $\beta_p < 1$. Low- A devices, therefore, tend to be strongly paramagnetic since $\beta_p = \langle p \rangle_{\text{vol}} / 2\mu_0 B_p(a)^2$ is smaller relative to $\beta = \langle p \rangle_{\text{vol}} / 2\mu_0 \langle B^2 \rangle_{\text{vol}}$ than for high aspect ratio. This can be seen in equilibrium calculations, and it introduces some uncertainties into the MHD stability limits discussed in Sec. 3.3 [6]. Here, $\langle \dots \rangle_{\text{vol}}$ denotes a volume average.

Program

Exploring the operational limits set on low-aspect-ratio tokamaks by MHD equilibrium and stability considerations is one of the principal objectives of USTX. It is encouraging that START has exceeded favorable theoretical expectations in several respects [8, 9]: first, by disruption-free operation (internal reconnection events did not lead to major disruptions), and second, by the observation of higher than expected confinement (exceeding conventional Neo-Alcator scaling, for example). In addition to testing these observations at higher current and beta, and in a low- A dominated plasma, the USTX experiment will investigate turbulence and transport, scrape-off layer physics, and sawtooth oscillations. We will also provide a target plasma and preparations for radio-frequency current drive; low-power antenna studies could begin near the end of Phase I.

We will ultimately require a time-dependent code that couples realistic USTX equilibria with theoretically credible transport and current-drive calculations. In the mean time, we will investigate equilibrium, stability, and transport with a variety of models tailored to individual purposes. Equilibria for initial performance estimates and engineering design, theoretical MHD stability, and turbulent transport studies will be generated with separate codes. We have begun to study transport using the simple model of the present section mapped onto one radial dimension. This approach has proven adequate to investigate current ramp-up (chapter 5), and will be used to scope out profile and confinement estimates, based on empirical or "mixing length" models, and to estimate the current drive required for particular q profiles.

In each of the areas relating to performance on USTX, there are fundamental physics issues to be addressed. These will afford almost limitless opportunities for research into the basic mechanisms of MHD stability, neoclassical effects, turbulence and anomalous transport, and wave propagation and current drive.

3.2 Equilibrium and position-stability control

To evaluate the expected performance of USTX we construct plasma equilibria using the EFIT code [10] to solve the Grad-Shafranov equation. Initially, these studies have been performed for the engineering design using standard current and pressure profiles (Sec. 5.4) [11]. These profiles are parameterized by a few constants which are optimized by the code to match a desired $q(0)$ and a desired plasma boundary. As noted in Sec. 3.1, it may be difficult with these profiles to achieve low $q(a)$ while maintaining $q(0) > 1$. START, however, has operated with q_{95} as low as 3.9 [12], where q_{95} is the safety factor at the 95% flux surface (corresponding to $(r/a)^2 = 0.95$ in our simple model). In the future, we will employ a wider range of profiles based on theoretical characterizations of stability and transport. We have also begun to develop a fast interactive Grad-Shafranov solver based on advanced adaptive grid methods [13, 14].

Control of shape in a low-aspect-ratio tokamak may be difficult. Since poloidal field coils are severely limited on the high field side of the torus, the last closed flux surface cannot be constrained as well as in a standard tokamak. This becomes an issue when trying to compensate the solenoid stray fields.

One advantage of a low-aspect-ratio tokamak, however, is its natural elongation; that is, a spatially uniform vertical field produces a neutrally stable equilibrium with elongation greater than unity, and with some natural triangularity as well. Such shapes can be advantageous from an MHD point of view. In medium-A tokamaks, elongation implies difficulties in position control, which would be alleviated in low-A tokamaks. Natural elongation has been described as a function of A and l_i (as shown in Fig. 3.3), although more recent calculations by the Culham group indicate a more complex functional dependency [15]. When fully non-inductive current drive is achievable, natural elongation will be a major feature of low-aspect-ratio tokamaks (it allows more current in the plasma for a given safety factor, without loss of vertical position stability). In the meantime, the solenoid and poloidal-field coils do not produce a homogenous vertical field, and the position stability and shape control of the plasma need to be studied

on a case by case basis. Further, the plasma shapes that we are considering may be elongated beyond that natural value, so up-down position feedback will be necessary [11].

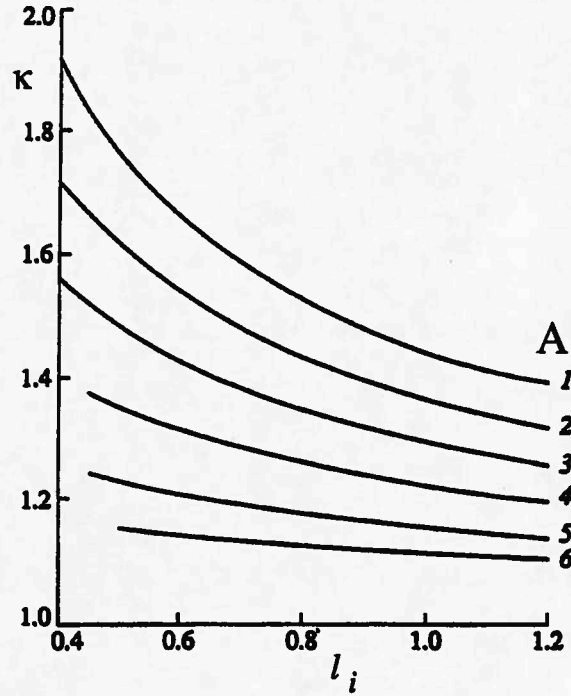


FIG. 3.3. Natural elongation as a function of l_i and A (from Kalmykov [15]).

3.3 MHD stability and high-beta operation

A principal goal of low- A studies is to verify that high β can be achieved, i.e., comparable to the Troyon limit [16],

$$\beta_{\max} (\%) \approx \beta_N \frac{I_p (\text{MA})}{a(\text{m}) B_{T0} (\text{T})}, \quad (3.10)$$

where β_N is a constant of order 3.5, I_p is the total plasma current and a is the horizontal minor radius. The considerations of Sec. 3.1 apply here, i.e., is there additional dependence on aspect ratio? The first studies of high- n ballooning and Mercier stability indicated that the scaling of Eq. (3.10) is reasonably well satisfied [7, 17-20]. The definition $\beta = \langle p \rangle_{\text{vol}} / 2\mu_0 B_{T0}^2$ was typically used in these studies, rather than $\beta = \langle p \rangle_{\text{vol}} / 2\mu_0 \langle B^2 \rangle_{\text{vol}}$. The studies of Holmes *et al.* [18], for example, began with

Troyon-optimized JET configurations at $A = 2.5$, which were then varied to $A = 1.6$ with subsequent further profile optimization at $q(a) \approx 3$ and $q(0) > 1$. It was assumed that sawtooth oscillations benignly flatten the profile at $q = 1$, or (tacitly) that some current drive scenario maintained $q(0) \approx 1.6$. For reversed-shear profiles β_N has been shown to reach values as high as 6 to 10 [7], with wall stabilization and extreme shaping.

A major question is whether such plasma profiles and shapes can be achieved in practice, and what happens when the profile strays from the optimum value. The role of bootstrap current (Sec. 3.4) is important here. Current profiles optimized for ideal MHD stability are characterized by strong gradients near the edge. These are likely to lead to tearing-mode activity, which will act to broaden the profile and degrade confinement, possibly inhibiting the formation of edge transport barriers. Numerical studies also show that ballooning instabilities play a more important role in determining the beta limits than in conventional tokamaks, where the kink mode is usually dominant. This, combined with the absence of hard disruptions in START, suggests that the β limit is "soft," leading to natural optimization of the pressure profile.

From the MHD point of view, some of the most interesting problems posed by a low-aspect-ratio tokamak are:

- 1) Strong toroidal coupling plus NBI makes this machine (Phase II) well suited for studying the stabilizing effect of rotation on low- n modes and the wall mode. This problem is relevant both to fusion in general and to advanced operating scenarios in particular. Note that the stabilizing effect of plasma rotation arises from the perpendicular component of the velocity shear. For high aspect-ratio plasmas rotating toroidally, the perpendicular component of the velocity shear is weak since the magnetic field lines have a weak pitch. In a low-aspect-ratio device, by contrast, the pitch of the magnetic field is of order unity on the outboard side, precisely where the curvature is unfavorable, so that the stabilizing effect of rotation will be enhanced at low aspect ratio.

- 2) A significant question that must be addressed experimentally is the role of "infernal" modes, which are predicted to be important in the presence of a large region with weak magnetic shear [18]. In this respect it should be noted that toroidal rotation has been shown to have a stabilizing effect in equilibria where the magnetic shear is weak.

3) There is a possible effect of l_i on β_N . If wall stabilization is effective, low l_i is preferable, as the broad current profile "leans" against the wall. If wall stabilization is not effective, then narrow current profiles or high l_i is favored. Current drive, together with neoclassical resistivity and bootstrap current should allow exploration of different current profiles at high β . In general, access to the highest β_N requires optimum q profiles [18]. As discussed earlier, it is essential to know whether such profiles, which imply hollow current distributions, can be obtained in practice. Also, MHD stability depends not only on the j profile, but on the pressure profile as well. Neutral beams, pellets, gas puffing, etc., can be used as knobs to modify both profiles, possibly in orthogonal ways.

4) Is the disruption-free operation of START characteristic of low- A tokamaks (because of the large q/q_{cyl} , for example)? What are the internal reconnection events, from which the plasma is able to recover? Would a close-fitting shell prevent recovery because of an increase in major radius during a disruptive event? Can a shell on the inboard side be effective to stabilize the kink?

We expect to explore these and other questions both analytically and numerically. USTX will be flexible enough to explore a wide range of plasma shapes and current profiles. We have already investigated the stability of some proposed equilibria (Sec. 5.8) using the MHD stability code of Glasser [21], which generalizes the criterion of Newcomb, and with the time-dependent nonlinear code of Aydemir [22]. Stability is found to be extremely sensitive to the shape and profile parameters. Charlton *et al.* [20] are also carrying out MHD stability studies.

The role of the $q=1$ surface in determining the Troyon limit is currently a focus of interest within the framework of the MHD initiative. Low-aspect-ratio tokamaks provide useful information on the role of the internal kink mode in setting the beta limit. The uniqueness of the $n = 1$ kink mode is a high aspect-ratio phenomenon: it arises as the result of the marginal stability of this mode in the large- A limit. Numerical studies of $n = 1$ stability performed at the Institute for Fusion Studies (IFS) show that this mode becomes more stable as the aspect ratio is decreased [23]. First, ideal marginal stability is increased with respect to the well-known Bussac threshold [24]. Second, the resistive growth rate is found to decrease continuously as a function of aspect ratio, vanishing asymptotically towards $A = 1$. For experimentally expected values of the resistivity, the resistive growth rate is expected to be very weak for USTX. The results also show that

elongation has an unfavorable effect on the kink growth rates, leading to significant growth rates for $\kappa > 1.6$.

3.4 Neoclassical effects

The neoclassical transport coefficients in the limit $A \rightarrow 1$ need to be computed for all ion collision frequencies ν_i ranging from the banana regime in the core plasma to the Pfirsch-Schlüter regime at the edge. This has, of course, been done for high A , and the analytic transport coefficients are well known [25, 26]. They are also known in the banana regime for $A \rightarrow 1$ [27] and have been verified by numerical calculations [28] (using the bounce-averaged Fokker-Planck code of Karney [29]). (See also Crume *et al.* [30].) For low collisionality, the numerical coefficients do not vary dramatically with aspect ratio. For example, one of the dimensionless coefficients in the bootstrap-current formula (Fig. 1 of Hirshman [27]) may be modeled by $L_{31} \approx \sqrt{\epsilon}(2.5 - \sqrt{\epsilon})$, which varies by about 50% over the range $\epsilon = 0.2 - 1$ or $A = 1 - 5$, as shown in Fig. 3.4.

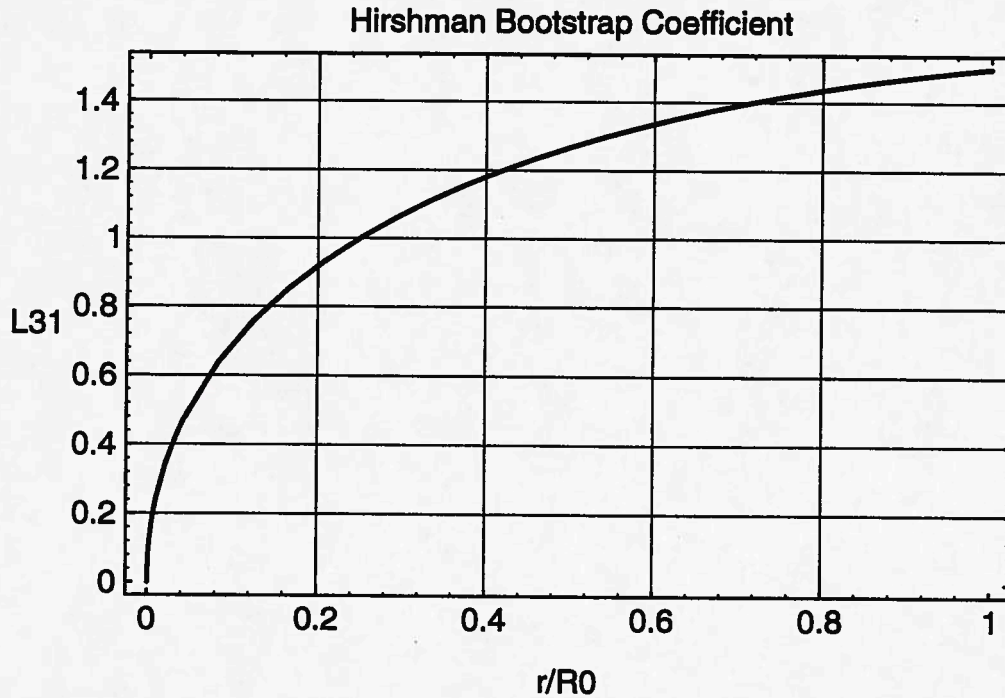


FIG. 3.4. Dependence of bootstrap current on inverse aspect ratio.

For the Pfirsch-Schlüter limiting values, however, previous expressions for $A \rightarrow 1$ are incomplete and may be misleading. Recent research by Shaing *et al.* [31] finds that in

the collisional regime there may be a large stress contribution arising from the singular A -dependence of the quantity $\langle (\mathbf{n} \cdot \nabla B)^2 \rangle \sim (1 - \epsilon)^{-3/2}$ as $\epsilon \rightarrow 1$, even though the viscosity coefficient is decreasing as ν_i^{-1} . Thus, the strong collisionality variation of the bootstrap-current transport coefficients and the ion thermal conductivity may diminish at low A , implying experimentally an increase in the bootstrap current as $A \rightarrow 1$ over the entire range of collisionality. This result follows from the assumption that a constant $q(a)$ is maintained as A is varied. Careful calculations are needed to determine how strong this effect will be in real equilibria for the aspect ratios of USTX. This will become important in the high- β regime, where the bootstrap current becomes significant.

In the banana regime, the neoclassical conductivity is reduced toward zero in the $A \rightarrow 1$ limit as the fraction of circulating particles f_c vanishes. This effect has been computed analytically and confirmed numerically [28]. Again, as the lower temperature, higher collisionality edge is encountered, conventional extrapolations [32] fail accurately to reproduce the physical effect noted above, namely, that the viscous stress remains high as $A \rightarrow 1$ even in the collisional regime. This effect tends to reduce the neoclassical conductivity to zero (relative to the classical value) as $A \rightarrow 1$, even though there are technically no trapped particles in the short mean free path regime! This also means that the neutral-beam and RF-driven currents may be reduced by the strong viscous effect.

Experimentally, an increased bootstrap current should manifest itself as a significant reduction (at fixed β_p) in the ohmic current required over the entire range of collisionality. This may not, however, imply a reduction in the volt-seconds required to run the tokamak in steady state (a large bootstrap fraction), since a calculation is needed to account for the offsetting effects of increased plasma resistance and decreased external and mutual inductance as $A \rightarrow 1$ [33]. We have implemented a simple model of these effects in a 1-D transport code.

ORNL researchers have constructed an analytical expression for the viscosity coefficients valid in arbitrary collision-frequency regimes and for all aspect ratios [34, 35]. This expression is being compared with the DKES code [36] to verify the asymptotic limits. Once the viscosity is known, all the transport coefficients (bootstrap, resistivity, conductivity) can be obtained by the moment approach. The advantage of this approach is that only a single analytical formula needs to be constructed instead of one formula for each coefficient as was done by Hinton and Hazeltine [25]. We will compute the transport coefficients for real equilibria to test Shaing's proposition [31].

3.5 Turbulence and transport

Empirical confinement and L-H mode considerations

We have obtained initial estimates of the confinement of USTX by means of zero-dimensional studies and by simulations with the SUPERCODE [37], using a variety of conventional scaling relations [38-41]. One of our goals is to cover the parameter space sufficiently to distinguish among the scaling relations. We have also performed a similar study in terms of dimensionless parameters, which shows that USTX can cover the reactor-like range in all variables except $\rho_* \equiv v_{ti} / \omega_{ci} a$ [42]. The results are discussed in Sec. 4.3.

We have already noted that these studies are highly uncertain, owing to the lack of empirical studies at low aspect ratio. As a simple example, consider the customary ohmic scaling known as neo-Alcator [43] and its subsequent variations. The q -dependence may scale as q^a , where $a \leq 1$, but is not well known [39]. It was not included at all in the original studies. Now, START confinement seems to greatly exceed neo-Alcator confinement if we assume it varies as q_{cyl} but not if we assume it varies as q , illustrating the need for extensive experimental studies. (We use this example for illustration only. Recent results on Alcator C-Mod suggest that this is not the right way to characterize ohmic confinement [44, 45].)

Another example is the power threshold for H-mode transitions. According to studies by Ryter *et al.* [46, 47] one expression for this is

$$P_{\text{thresh}} (\text{MW}) / S (\text{m}^2) = 0.04 \bar{n}_e (\text{m}^{-3}) B_{T0} (\text{T}), \quad (3.11)$$

where S is the plasma surface area. This result, which is highly favorable for H mode in USTX, has not been extended to low aspect ratio, but other forms of the scaling relation give even more favorable major-radius scaling [46]. The threshold also depends on other factors, which have not all been quantified [46]: magnetic drift (about a factor of two for the unfavorable direction), limiter proximity, neutral beam angle (perpendicular is favorable in PBX), and, perhaps most important, edge temperature, which must be sufficiently high prior to the transition.

Equation (3.11) suggests that USTX should always be in H mode. We are using an H-factor of 1.6 in most of our confinement scaling studies, based on expectations for

$H^0 \rightarrow D^+$ beam injection in Phase II, or on scaled START studies in the ohmic Phase I. In ASDEX, an H-factor of 2 was found for $D^0 \rightarrow D^+$ and 80% of this value for other beam-target combinations [47]. This is consistent with an overall mass scaling as $A_i^{0.3}$ to $A_i^{0.45}$ obtained from the ITER H-mode database, depending on the machine and whether the H mode is ELMy or ELM-free [48]. With this assumed scaling we infer (Sec. 4.3) that we can cover the desired range of plasma conditions, including the β limit, without deuterium injection, although we also intend to perform a limited number of experiments using deuterium injection.

A third example of a scaling uncertainty is the density limit, given by either the Greenwald [49] or the Hugill [50] expression,

$$\bar{n}_{e20} < I_p (\text{MA}) / \pi a^2, \quad (3.12)$$

and

$$\bar{n}_{e20} < 2B_{T0} (\text{T}) / R_0 q, \quad (3.13)$$

respectively, where \bar{n}_{e20} is the chord-averaged density in 10^{20} m^{-3} . This is an important issue because the maximum achievable β , with a given neutral beam power, can be a fairly sensitive function of the density limit [51]. If the expression for q rather than q_{cyl} is used in the Hugill expression, then the Greenwald and Hugill limits are found to differ by a factor involving only κ and δ with the Greenwald limit the more optimistic of the two for $\kappa > 1.23$ by a factor of approximately $0.4(1 + \kappa^2)$. The physics basis for the density limit is generally understood to be an edge density and radiation limit [51].

A recent study of the density limit on DIII-D demonstrates that the Hugill limit does not adequately represent the DIII-D data [52]. In particular, the unfavorable scaling of the Hugill limit with κ was not observed when κ was varied at constant q_{95} . On the other hand, the Greenwald limit when multiplied by 0.80 accurately predicts the density limit for all conditions in DIII-D as long as $Z_{\text{eff}} \leq 2$. We have used this value as an upper bound for most of our scaling studies. It remains to be demonstrated whether the more favorable κ scaling of the Greenwald limit holds at low aspect ratio.

We have begun to complement the SUPERCODE and zero-dimensional studies by employing a new one-dimensional transport code [53], taking into account ellipticity, triangularity, finite aspect ratio, and neoclassical effects, using the simple geometry described in Sec. 3.1. This will allow us, prior to the operation of the device, to explore

scenarios of the plasma evolution and profiles, including current ramping and penetration, bootstrap current, *ad hoc* current drive, various transport models [54-56], and later a sawtooth model. Initially, we have carried out current ramping studies to assist with the engineering design, Chap. 6. Eventually, we will employ a full two-dimensional fluid code, coupled to the equilibrium, making use of advanced computational methods [14, 57].

Power-balance data will provide points in a new region of parameter space. We have begun a study to see whether the range of parameters available in USTX will be sufficient to distinguish among the various global scaling relations, taking into account typical experimental errors. The initial results (Sec. 4.3) show that we should be able to distinguish those of different "families." (L-mode scalings that are generically of the Goldston [38] or ITER-89P [40] type are likely to remain indistinguishable from one another.) Most of these studies will require the NBI of Phase II. Even in the ohmic Phase I, however, we may be able to distinguish $I_p \propto q_{\text{cyl}}^{-1}$ from q in some of the confinement dependences, as discussed earlier. Since both the aspect ratio and current can be varied, a wide range of q will be accessible. Furthermore, by current ramping, a range of current profiles can be explored. As proposed theoretical explanations develop, these distinctions become as important here as in the MHD studies.

Turbulence and anomalous transport

We now turn to the topics which have been historically of greatest interest to the TEXT, FRC Theory, and IFS groups. From the physics point of view, the questions are not only how well a proposed machine will perform, but what we can learn about confinement scaling and basic transport mechanisms from the experiments.

All of the effects mentioned in Sec. 3.1 play a role in the investigation of turbulence and transport: the fraction of trapped particles, bounce-averaged drifts, collisionality, and degree of mode ballooning. All theoretical calculations need to be looked at carefully, and most likely redone, to take these into account. Some numerical codes in current use already contain the full (axisymmetric) geometry. For example, the work reported for low A by Rewoldt and Tang [58, 59] employs a linear eigenvalue code with quasilinear transport estimates in the ballooning representation. (See also Rewoldt, Tang, and Hastie [60] and references therein.) All the relevant geometrical and trapped particle effects are included, as well as an accurate model collision operator.

In work performed at the IFS (with PPPL), a quasilinear initial-value ballooning code by Kotschenreuther also now contains all the relevant geometry and a Fokker-Planck collision operator, and a full 3-D nonlinear code by Dorland *et al.* is being modified to include all these effects [61-66]. This work has so far focused on the ion-temperature-gradient (ITG) mode regime, with considerable success in describing TFTR experimental data. Attention is now being directed at the plasma edge region, and full non-adiabatic electron effects are being incorporated, so that trapped-electron modes can be included.

One might expect that the increased fraction of trapped particles at large- ε would lead to greater instability. Simple trapped-particle-mode theory [67] suggests that modes can always balloon to the bad curvature regions and go unstable. Initial results from Rewoldt [58, 59], however, for trapped-electron modes indicate greater stability in the low-aspect-ratio limit. The reason for this is that more of the trapped-particle orbit is in the good curvature region, providing stabilizing resonances between the bounce-averaged drifts and the waves. Ion Landau damping prevents the modes from ballooning too strongly to the outside, because the implied larger k_{\parallel} brings the ion resonant velocity into the thermal range.

Another important aspect of low frequency turbulence at high β is the necessity to include all components of the magnetic fluctuations. The usual drift-Alfvén ordering, as employed, e.g., in the IFS work described above, retains the electrostatic and parallel vector potentials, ϕ and A_{\parallel} , and neglects the perpendicular vector potential, i.e., the parallel or compressional magnetic fields. This ordering is likely to break down at the β values of 30-40% envisioned in spherical tokamak experiments. Coupling to the compressional modes will have to be computed, which is no trivial undertaking.

Finally, just as in MHD theory, transport theory places shear in the mass flow, u , as a primary control parameter, on equal footing with the magnetic shear. New understanding of basic plasma physics for transport will occur when the parallel mass flow, u_{\parallel} , and the ion thermal flow, q_{\parallel} , are documented by spectroscopic and probe measurements. Just as these flows determine the momentum viscosity $\langle \mathbf{B} \cdot \nabla \cdot \Pi \rangle$ and the thermal viscosity $\langle \mathbf{B} \cdot \nabla \cdot \Theta \rangle$ that determine the bootstrap current and poloidal flow damping, they also determine the nature of the fluctuation-induced transport and the L- to H-mode threshold (by shear-suppression of the turbulence). These features also indirectly affect the degree to which there is a macroscopic component to the correlation length $l_c = \rho_s (L_T / \rho_s)^{\alpha}$ with $\alpha > 0$. Power balance studies, nonlocal phenomena (as

observed on TEXT in cold pulse studies), and ρ^* scaling all suggest that $\alpha \approx 1/2$ (Bohm) is a feature of correlation length. These scaling issues were the focus of the turbulence studies at the 1995 Santa Barbara ITP Program [68] and could be a part of the USTX studies. Mass and thermal flows distort the ion distribution with two components, $f_i = F_1 + g_1$, where F_1 contains the Pfirsch-Schlüter flows that are driven by the divergence of the compression in the flows, and g_1 is the incompressible part of the global flow components. Each of the components (F_1, g_1) has two surface functions associated with it connected to the mass flow and the thermal flow. Thus, $u_{||} = V_1(\psi)/B + K_1(\psi)B$, which has the same as the form as the current density. The strong compression and large poloidal asymmetries in a spherical tokamak offer a unique opportunity for measurement.

Much work remains to be done, with great opportunities for analytical as well as numerical work. Analytical calculations can help to identify the most unstable modes by showing how changes in the drifts, collisionality, and degree of mode ballooning affect stability. The IFS numerical initial-value code [61], mentioned above, finds the most unstable mode automatically, but even with this very fast code, only a limited number of cases can be run. Collisionality is crucial: the scaling of the ion temperature-gradient (ITG) mode equations indicates that collisional ITG modes should be increasingly stable, while the presence of more trapped particles in the collisionless regime could still be dangerous [69]. Of course, the weighting of quantities over the flux surface is crucial. As noted earlier, adaptation of transport codes to low-A studies is important to determine the evolution of the plasma profiles for comparison with power balance analysis and MHD stability. The IFS model [61-66] will also be used in a transport code coupled to a computed equilibrium. The H-mode theories developed for high-aspect-ratio tokamaks also need to be extended to include finite-aspect-ratio effects. The results will be useful not only for USTX, but also for validating transport scenarios in other machines, including ITER.

The modes discussed above employ the standard ballooning formulation. A systematic investigation of the 2-D structure of modes in an axisymmetric torus, however, reveals other interesting possibilities [70, 71]. Recently, a new structure (Ballooning Mode II) has been found which, in the resistive limit, displays up-down asymmetry in the poloidal plane [71] in contrast to the usual modes centered about $\theta = 0$ (or π). These interesting 2-D structures can occur at a variety of radii and should manifest themselves with observable signatures in a low-A torus. Testing of the

mathematical theories of 2-D modes could be an important component of the physics program on USTX.

A recent result of Isichenko *et al.* [72-74] illustrates how low aspect ratio can enhance our attempts at experimental verification. These authors' theory of the anomalous particle pinch implies that $n_e(r)q(r) \approx \text{const}$ at high aspect ratio. This is approximately borne out by TEXT data. More generally, however, $n_e(\psi)V'(\psi) = \text{const}$, where $V'(\psi)$ is the derivative of the volume enclosed by the poloidal flux ψ . At small ε , these two expressions become indistinguishable, but as $\varepsilon \rightarrow 1$ differences will be observable. The original work [72] dealt with trapped-particle transport in the collisionless regime, while more recent studies have turned to the effects of passing particles and high collisionality [73, 74].

Experimentally, a low-aspect-ratio machine provides opportunities to extend fluctuation studies, like those performed on TEXT and TEXT-U, to help verify or refute the concepts discussed above. Together with power-balance scaling studies, systematic investigation of the fluctuations should shed further light on transport theories. The low-aspect-ratio device is ideal for such studies. Because of the small magnetic field and relatively large minor radius, if gyro-Bohm-like drift waves (including ITG modes) are present, we might expect $k_{\perp} \sim \rho_s^{-1} \sim B_{T0}$ to be small, and the fluctuation level $\tilde{n}/n \sim 1/k_{\perp} L_n \sim \rho_s/L_n$ to be moderately large. Comparing to TEXT, we expect $k_{\perp} \approx 0.5 - 1.0 \text{ cm}^{-1}$ and $\tilde{n}/n \approx 3 - 4\%$ in the interior of USTX. Thus, the HIBP and BES will be able to measure the fluctuations easily and to access the greater portion of the spectrum, making comparison with FIR scattering easier (see chapter 8). The effects of the radial electric field and its gradient would also have to be explored. We also intend to employ Langmuir probes in the far edge and scrape-off layer (SOL). Here, the effects of low aspect ratio on the SOL-width scaling and correlation properties can be studied. The effect of the geometry on parallel correlation and field-line identification should be particularly interesting. Besides current ramping, other perturbative experiments will also help elucidate fluctuation and transport behavior. We will devote some attention to determining which ones are feasible in a low-aspect-ratio configuration.

In view of the strong in-out asymmetries expected, we desire (or need) a full complement of profile diagnostics, covering the plasma cross section. Access should be sought to as much of the plasma as possible for each diagnostic, e.g., HIBP, BES, and FIR scattering (see chapter 8). Poloidal-field or pitch-angle measurements will be particularly important to give us a direct determination of the current or q profile.

3.6 Heating and current drive

The small inner ohmic solenoid of a low-aspect-ratio tokamak implies that one cannot depend on the ohmic current and heating alone. Auxiliary current drive is an outstanding problem for most tokamak reactor scenarios, but it may be the single most critical element in realizing the reactor potential of the low- A tokamak. First, the limited available space for coil placement and the limits on available volt-seconds make inductive ramp-up and long flat-top times difficult. Second, controlled auxiliary drive will probably be required to get to the desired q -profiles for MHD stability and large bootstrap fraction, as well as to maintain those desired profiles.

Low-aspect-ratio current-drive investigations are exploratory and should first be conducted in a modest device like USTX. We will provide a flexible target facility for such tests, with a toroidal-field time exceeding the inductive-current time. There is an extraordinary opportunity for development of new theoretical descriptions and physics understanding in the geometry depicted in Figs. 3.1. Again, because of the breakdown of small- ε expansions, we cannot be sure *a priori* how wave propagation and particle acceleration will scale to low A . Also, in light of neoclassical considerations (Sec. 3.4), we will need to revisit the driven currents in all collisionality regimes.

Current drive by tangential neutral-beam injection may turn out to be the principal non-inductive method. In Phase II, we intend to explore current-profile control through neutral-beam current drive (NBCD) to determine whether net profiles can match those required to reach the high- β and the low- q regimes. ECH-assisted breakdown and current ramp has been shown to be promising by results from START [75] and CDX-U [76-78], and will be implemented on USTX. Computationally, we have begun to simulate the current ramp with a transport code including a model of the ECH heating and initial current distribution. Coaxial helicity injection (CHI), based on results from the Helicity Injected Tokamak (HIT) [79], is also being considered. Since HIT operates essentially in a spherical tokamak configuration, the main physics questions are the scaling with size and plasma parameters. We shall postpone further discussion of the above methods to chapter 7.

Finally, we will provide a test bed for Alfvén-wave and fast-wave current drive (AWCD and FWCD) on USTX — for example, in a collaborative program proposed by the University of Wisconsin (Sec. 7.4). We devote the rest of this chapter to Alfvén

waves, as another example of both the physics opportunities and the difficulties afforded by low- A studies.

Alfvén-wave and fast-wave current drive

AWCD has been demonstrated on the Phaedrus-T tokamak [80, 81], and further experiments and testing of innovative antenna arrays are planned for the next two years. We intend to explore a range of scenarios from $\omega \leq \omega_{ci,\min}$ to $\omega > \omega_{ci,\max}$, with the possibility of going to $\omega \gg \omega_{ci}$ in the later experimental phases.

Alfvén wave theory

Alfvén-wave calculations are often done in terms of nearest neighbor poloidal-harmonic coupling. For higher frequencies, an eikonal or ray-tracing method is often used. We have experience, for example, in the kinetic description of Alfvén-wave propagation, absorption, and current drive [82-90] and have identified some of the effects experimentally [91, 92]. These studies, however, suffer from the same difficulties as those of micro-instabilities and must be redone for the low- A case.

For Alfvén waves in a cylinder the important resonance (resolved by kinetic effects) is

$$\omega^2 = \frac{(k_{\parallel} V_A)^2}{1 + (k_{\parallel} V_A / \omega_{ci})^2}, \quad (3.14)$$

where $\omega < \omega_{ci}$ is the driven frequency, $V_A = B / \sqrt{\mu_0 m_i n_i}$ is the Alfvén velocity, $k_{\parallel} = (n - m/q) / R$, and n/m are the toroidal/poloidal mode numbers. Energy absorption and current drive occur through electron Landau damping of kinetic Alfvén waves generated near the surfaces defined by Eq. (3.14). At small- ε in circular plasmas, we may restrict ourselves to coupling neighboring values of m to $m \pm 1$. Introduction of elongation couples m to $m \pm 2$. In the low- A torus, on the other hand, the Alfvén velocity varies by a factor of four or five over the plasma cross section. All harmonics are coupled, and we must treat $k_{\parallel} \rightarrow \partial/\partial s$ as an operator, following the wave propagation in the direction s along the field line. In the MHD limit, the existence of Alfvén resonances coincident with flux surfaces has been proved [93]. If, however, an effective potential well forms for the wave, standing modes might result, inhibiting traveling-wave propagation and current drive [94]. At finite values of ω/ω_{ci} , the existence of resonant

surfaces is itself then brought into question [95, 96]. New theoretical and numerical methods need to be developed before we can be certain how the energy deposition and current drive will be distributed radially. This problem is very difficult, because the parallel wave number appears in the argument of the electron plasma dispersion function $Z(\omega / |k_{\parallel}| v_e)$. Full-wave calculations with kinetic effects have not yet fully taken into account the toroidicity [97-99]. The presence of trapped electrons may also inhibit current generation, although there is reason to believe this may not be a problem [100].

TAE mode investigations

It is known that anomalous loss of suprathermal particles can be caused by their resonant interaction with shear Alfvén modes or with low-frequency MHD waves (e.g., kinks, sawteeth, etc.). This is of particular relevance to fusion reactors containing alpha particles, but is also important for non-ignited plasmas with high-power auxiliary heating (NBI, ICRH) that can create fast ion tails. As an example, consider the toroidicity-induced shear Alfvén eigenmode (TAE) that has been predicted and observed in usual tokamaks and also in helical devices. In a spherical tokamak, since the inverse aspect ratio is larger than the value of the magnetic shear out to a larger radius, the low-shear version of the TAE modes (the so-called "core localized modes" [101]) have, in fact, recently been found to have an enlarged spectrum, with a multiplicity of modes present [102]. Due to their broadened radial width, these multiple core-localized TAE modes are expected to be robustly unstable. Thus a spherical tokamak like USTX would be a convenient "laboratory" for investigating the threshold characteristics and nonlinear behavior of the TAE modes. Either neutral beams or externally antenna excitation could be used to drive these modes in the experiment. Since the trapped particle fraction is large at low aspect ratio, the destabilizing wave-particle interaction would presumably occur at the fast particle bounce frequency (for shear Alfvén modes) or the precessional frequency (for lower frequency MHD modes). Theory collaborators at JET (H. Holties and S. Sharapov) have recently run calculations with their 2-D linear stability code, CASTOR, and found that multiple TAE modes may be expected in USTX. Means of exciting these modes and their damping mechanisms will be examined theoretically to determine whether such experiments are feasible in Phase I.

Fast-wave current drive

Another possibility for current drive is that by fast waves below ω_{ci} (compressional Alfvén waves), which has been investigated for wave numbers with weak Alfvén resonance absorption [88]. At low aspect ratio, however, *any* antenna will generate a broad spectrum of poloidal harmonics and modes related to both branches of the dispersion relation. Therefore, it is not generally possible to completely separate AWCD and FWCD effects. Energy deposition in the plasma periphery may dominate, owing to the presence of "side-band" harmonics, as observed in MHD calculations at Lausanne [96, 98, 103-105]. Studies with their code LION [105] are being initiated at the University of Wisconsin. Frequencies in the range $\omega \geq \omega_{ci,max}$ appear to yield good electron absorption for FWCD.

Fast-wave current drive in the intermediate range of frequencies, $\omega_{ci} \ll \omega \ll \omega_{LH}$, where ω_{LH} is the lower hybrid frequency, is also under investigation [106]. Successful heating and current drive have been detected in this range in DIII-D [107-109], where one avoids complications with low-order cyclotron harmonics. In considering these fast magnetosonic waves in USTX, we note that the ion cyclotron frequency, f_{ci} , at $B_{T0} = 0.5$ T and $A = 1.43$, varies from 3.5 to 13 MHz (including the poloidal field) over the deuterium plasma cross section. We are considering frequencies up to 13 MHz with possible extensions to 40 MHz. The DIII-D results have been simulated by the ORNL PICES code [97], but again we expect large changes in the propagation and absorption properties of the waves owing to the strong toroidal coupling.

The future: high beta and small aspect ratio plasmas in astrophysics

High beta plasmas are common in astrophysics. Among other things, a distinguishing aspect of these plasmas is the strong coupling between the Alfvén and the sound waves. It is also not uncommon to find toroidally confined plasmas in the stellar coronas. The solar coronal loops (some with long lifetimes) are a subject of great interest and may possibly hold the key to understanding the coronal heating mechanisms which lead to temperatures of the order of a few hundred eV. Many of the more stable coronal loops are parts of low aspect-ratio tori with their 'feet' located on the solar surface. The formation, maintenance, stability, and density and temperature profiles of these loops, and the processes that heat the plasma in their interiors, are still far from understood. A

laboratory experiment which can closely simulate these natural plasmas can be of great help in solving a number of observational puzzles. It should be possible, by doing controlled experiments in a low aspect-ratio torus, to test some of the contending theoretical models proposed to explain the richness of the phenomena observed in the solar atmosphere. In particular, an investigation of the propagation characteristics of the collective modes, their ability to drive currents in, and to heat the ambient plasma could be very significant.

In summary, we emphasize once more that it is crucial to institute a research program on a relatively modest device such as USTX, together with supporting theoretical work, before we commit to dependence on these methods on the reactor scale. An enormous amount of interesting physics remains to be investigated.

References to Chapter 3

- [1] H. C. Howe, *PROCTR Formulary*, Report ORNL/TM-9537, Oak Ridge National Laboratory (1985).
- [2] J. Blum and J. Le Foll, *Computer Phys. Reports* **1** (1984) 465.
- [3] W. W. Pfeiffer, R. H. Davidson, R. L. Miller, *et al.*, *ONETWO: A Computer Code for Modeling Plasma Transport in Tokamaks*, Report GA-A16178, General Atomic Company (1980).
- [4] J. T. Hogan, *Nucl. Fusion* **19** (1979) 753.
- [5] L. E. Zakharov and V. D. Shafranov, in *Reviews of Plasma Physics*, edited by M. A. Leontovich, (Consultants Bureau, New York, 1986), Vol. 11, p. 153.
- [6] Y.-K. M. Peng and D. J. Strickler, *Nucl. Fusion* **26** (1986) 769.
- [7] V. S. Chan, M. S. Chu, C. B. Forest, *et al.*, in *Proceedings of the Small Aspect Ratio Tokamaks Workshop*, Oak Ridge, TN, (1994); V. S. Chan, M. S. Chu, R. Miller, *et al.*, in *Proceedings of the U. S.-Japan Workshop for Low Aspect Ratio Tokamak and International Workshop on Spherical Torus*, Princeton, NJ, 13-15 November, 1995; J. Menard, M. Chance, S. Jardin, *et al.*, *ibid.*
- [8] A. Sykes, J. W. Connor, R. Duck, *et al.*, *Plasma Phys. Controlled Fusion* **35** (1993) 1051.
- [9] M. Gryaznevich and the START Team, in *Proceedings of the U. S.-Japan Workshop for Low Aspect Ratio Tokamak and International Workshop on Spherical Torus*, Princeton, NJ, 13-15 November, 1995, Vol. 1.
- [10] L. L. Lao, H. St. John, R. D. Stambaugh, *et al.*, *Nucl. Fusion* **25** (1985) 1611.
- [11] E. R. Solano, D. J. Strickler, J. Uglum, *et al.*, in *Proceedings of the Sherwood Theory Conference*, Lake Tahoe, NV, (1995).
- [12] M. Gryaznevich, R. J. Colchin, R. Duck, *et al.*, in *Proceedings of the 21st European Phys. Soc. Conf. on Controlled Fusion and Plasma Physics*, Montpellier, (European Physical Society, 1994), Vol. 18B, Part I, p. 22.
- [13] J. C. Wiley and D. W. Ross, in *Proceedings of the Sherwood Theory Conference*, Lake Tahoe, NV, (1995).
- [14] J. C. Wiley, in *Proceedings of the Second Annual Object-oriented Numerics Conference*, Sun River, Oregon, (1994).
- [15] S. G. Kalmykov, *Plasma Phys. Reports* **20** (1994) 844; M. Gryaznevich (personal communication (1996)).
- [16] F. Troyon, R. Gruber, H. Saurenmann, *et al.*, *Plasma Phys. Controlled Fusion* **26** (1984) 209.
- [17] S. G. Bespoludennov, L. M. Degtyarev, and S. Y. Medvedev, *Sov. J. Plasma Phys.* **12** (1986) 441.
- [18] J. A. Holmes, L. A. Charlton, J. T. Hogan, *et al.*, *Phys. Fluids B* **1** (1989) 358.

- [19] B. A. Carreras, L. A. Charlton, J. T. Hogan, *et al.*, in *Plasma Physics and Controlled Nuclear Fusion Research 1986*, (International Atomic Energy Agency, Vienna, 1987), Vol. 2, p. 53.
- [20] L. A. Charlton, J.-N. Leboeuf, and B. A. Carreras, *Bull. Am. Phys. Soc.* **39** (1994) 1700.
- [21] A. H. Glasser, *The Direct Criterion of Newcomb for the Stability of an Axisymmetric Toroidal Plasma*, Report LA-UR-95-528 (submitted to *Phys. Plasmas*), Los Alamos National Laboratory (1995).
- [22] A. Y. Aydemir, R. E. Denton, R. D. Hazeltine, *et al.*, in *Plasma Physics and Controlled Nuclear Fusion Research 1988*, (International Atomic Energy Agency, Vienna, 1989), Vol. 2, p. 131.
- [23] A. Y. Aydemir, in *Proceedings of the Sherwood Theory Conference*, Lake Tahoe, NV, (1995).
- [24] M. N. Bussac, R. Pelat, D. Edery, *et al.*, *Phys. Rev. Lett.* **35** (1976) 1638.
- [25] F. L. Hinton and R. D. Hazeltine, *Rev. Mod. Phys.* **48** (1976) 239.
- [26] S. P. Hirshman and D. J. Sigmar, *Nucl. Fusion* **21** (1981) 1079.
- [27] S. P. Hirshman, *Phys. Fluids* **31** (1988) 3150.
- [28] Y. R. Lin-Liu, F. L. Hinton, C. F. F. Karney, *et al.*, in *Proceedings of the Sherwood Theory Conference*, Dallas, TX, (1994).
- [29] C. F. F. Karney and N. J. Fisch, *Phys. Fluids B* **29** (1986) 180.
- [30] E. C. Crume, Jr., C. O. Beasley, Jr., S. P. Hirshman, *et al.*, *Phys. Fluids* **30** (1987) 1152.
- [31] K. C. Shaing, C. T. Hsu, M. Yokoyama, *et al.*, *Phys. Plasmas* **2** (1994) 349.
- [32] S. P. Hirshman, R. J. Hawryluk, and B. Birge, *Nucl. Fusion* **17** (1977) 611.
- [33] S. P. Hirshman and G. H. Neilson, *Phys. Fluids* **29** (1986) 790.
- [34] W. Houlberg, in *Proceedings of the U. S. - Japan Workshop on Bootstrap Current in Tokamaks and Stellarators*, Lake Lanier Islands, GA, (1994).
- [35] W. A. Houlberg, K. C. Shaing, and S. P. Hirshman, in *Proceedings of the Sherwood Theory Conference*, Lake Tahoe, NV, (1995).
- [36] S. P. Hirshman, K. C. Shaing, W. I. V. Rij, *et al.*, *Phys. Fluids* **29** (1986) 2951.
- [37] S. W. Haney, W. L. Barr, J. A. Crotinger, *et al.*, *Fusion Tech.* **21** (1992) 1749.
- [38] R. J. Goldston, *Plasma Phys. Controlled Fusion* **26** (1984) 87.
- [39] S. M. Kaye, *Phys. Fluids* **28** (1985) 2327.
- [40] S. M. Kaye, C. W. Barnes, M. G. Bell, *et al.*, *Phys. Fluids B* **2** (1990) 2926.
- [41] N. A. Uckan, *Fusion Tech.* **15** (1989) 391.
- [42] G. G. Castle, *Dimensionless parameters, scaling laws, and the implications for ETG*, Report FRCR # 462, The University of Texas (1995).
- [43] S. Fairfax, A. Gondhalekar, R. Granetz, *et al.*, in *Plasma Physics and Controlled Nuclear Fusion Research 1980*, (International Atomic Energy Agency, Vienna, 1981), Vol. 1, p. 439.

- [44] M. Greenwald, R. L. Boivin, F. Bombarda, *et al.*, Bull. Am. Phys. Soc. **39** (1994) 1751.
- [45] M. Greenwald and Alcator Group, Bull. Am. Phys. Soc. **39** (1994) 1666.
- [46] F. Ryter and H-Mode Database Working Group, in *Proceedings of the 20th European Phys. Soc. Conf. on Controlled Fusion and Plasma Physics*, Lisboa, (European Physical Society, 1993), Vol. 17C, Part I, p. 15.
- [47] F. Ryter, M. Alexander, J. C. Fuchs, *et al.*, in *Proceedings of the 21st European Phys. Soc. Conf. on Controlled Fusion and Plasma Physics*, Montpellier, (European Physical Society, 1994), Vol. 18B, Part I, p. 330.
- [48] O. Kardaun, F. Ryter, U. Stroth, *et al.*, in *Plasma Physics and Controlled Nuclear Fusion Research 1992*, (International Atomic Energy Agency, Vienna, 1993), Vol. 3, p. 251.
- [49] M. Greenwald, J. L. Terry, S. M. Wolfe, *et al.*, Nucl. Fusion **28** (1988) 2199.
- [50] J. Hugill, in *Proceedings of the 2nd Joint Varenna-Grenoble Symposium on Heating in Toroidal Plasmas*, edited by E. Canobbio, H. P. Eubank, G. G. Leotta, *et al.*, Como, Italy, (CEC, Brussels, 1980), Vol. II, p. 775.
- [51] D. E. Post, in *ITER Physics IAEA/ITER/DS/21* (ITER Doc Series), (IAEA, Vienna, 1991).
- [52] T. W. Petrie, A. G. Kellman, and M. A. Mondavi, Nucl. Fusion **33** (1993) 929.
- [53] D. W. Ross and J. C. Wiley, Bull. Am. Phys. Soc. **40** (1995).
- [54] D. W. Ross, P. H. Diamond, J. F. Drake, *et al.*, *Thermal and Particle Transport in Tokamaks—Theoretical Models for Ignition Studies*, Report FRCR #295, The University of Texas (1987).
- [55] R. E. Waltz, R. R. Dominguez, F. W. Perkins, *et al.*, in *Plasma Physics and Controlled Nuclear Fusion Research 1988*, (International Atomic Energy Agency, Vienna, 1989), Vol. 3, p. 369.
- [56] W. A. Houlberg, D. W. Ross, G. Bateman, *et al.*, Phys. Fluids B **2** (1990) 2913.
- [57] J. C. Wiley and D. W. Ross, in *Proceedings of the Sherwood Theory Conference*, Dallas, TX, (1994).
- [58] G. Rewoldt and W. M. Tang, in *Proceedings of the Small Aspect Ratio Tokamaks Workshop*, Oak Ridge, TN, (1994).
- [59] G. Rewoldt, W. M. Tang, and S. Kaye, Bull. Am. Phys. Soc. **39** (1994) 1573.
- [60] G. Rewoldt, W. M. Tang, and R. J. Hastie, Phys. Fluids **30** (1987) 807.
- [61] M. Kotschenreuther, W. Dorland, M. A. Beer, *et al.*, *Quantitative Predictions of Tokamak Energy Confinement from First-Principles Simulations with Kinetic Effects*, Report IFSR #693 (APS invited talk, to be published in Phys. Plasmas), The University of Texas (1995).
- [62] W. Dorland, M. Kotschenreuther, M. A. Beer, *et al.*, in *Plasma Physics and Controlled Nuclear Fusion Research 1994*, (International Atomic Energy Agency, Vienna, 1995).
- [63] M. Kotschenreuther, in *Proceedings of the Transport Task Force Workshop*, Marina del Rey, CA, (1995).
- [64] W. Dorland, in *Proceedings of the Transport Task Force Workshop*, Marina del Rey, CA, (1995).

- [65] M. Kotschenreuther and W. Dorland, in *Proceedings of the Sherwood Theory Conference*, Lake Tahoe, NV, (1995).
- [66] W. Dorland, in *Proceedings of the Sherwood Theory Conference*, Lake Tahoe, NV, (1995).
- [67] M. N. Rosenbluth, *Phys. Fluids* **11** (1968) 869.
- [68] M. Ottaviani, M. A. Beer, S. Cowley, W. Horton, and J. Krommes, *Unanswered Questions in Ion-Temperature-Gradient-Driven Turbulence*, Institute for Theoretical Physics, Santa Barbara (1995).
- [69] M. Kotschenreuther, personal communication (1994).
- [70] Y. Z. Zhang and S. M. Mahajan, *Phys. Lett. A* **157** (1991) 133.
- [71] Y. Z. Zhang and S. M. Mahajan, *Phys. Plasmas* **2** (1995) 4236.
- [72] M. B. Isichenko, A. V. Gruzinov, and P. H. Diamond, submitted to *Phys. Rev. Lett.* (1994).
- [73] M. Isichenko, in *Proceedings of the Transport Task Force Workshop*, Marina del Rey, CA, (1995).
- [74] M. Isichenko, in *Proceedings of the Sherwood Theory Conference*, Lake Tahoe, NV, (1995).
- [75] A. Sykes, M. Bevir, R. A. Bamford, *et al.*, in *Plasma Physics and Controlled Nuclear Fusion Research 1994*, (International Atomic Energy Agency, Vienna, 1995), Vol. 1, p. 719.
- [76] C. B. Forest, *Pressure Driven Currents in CDX-U Trapped Particle Configuration*, Ph. D. Dissertation, Princeton University (1992).
- [77] C. B. Forest, Y. S. Hwang, M. Ono, *et al.*, *Phys. Rev. Lett.* **68** (1992) 3559.
- [78] C. B. Forest, Y. S. Hwang, M. Ono, *et al.*, *Phys. Plasmas* **1** (1994) 1568.
- [79] B. A. Nelson, T. R. Jarboe, D. J. Orvis, *et al.*, *Phys. Rev. Lett.* **72** (1994) 3666.
- [80] S. Wukitch, M. Vukovic, R. Breun, *et al.*, *Phys. Rev. Lett.* **74** (1995) 2240.
- [81] T. Intrator, *Bull. Am. Phys. Soc.* **39** (1994) 1720 (invited talk to be published in *Phys. Plasmas*).
- [82] D. W. Ross, G. L. Chen, and S. M. Mahajan, *Phys. Fluids* **25** (1982) 652.
- [83] S. M. Mahajan and D. W. Ross, *Phys. Fluids* **26** (1983) 2195.
- [84] S. M. Mahajan and D. W. Ross, *Phys. Fluids* **26** (1983) 2561.
- [85] S. M. Mahajan, *Phys. Fluids* **27** (1984) 2238.
- [86] D. W. Ross, Y. M. Li, S. M. Mahajan, *et al.*, *Nucl. Fusion* **26** (1986) 139.
- [87] S. Ryopoulos and S. Mahajan, *Phys. Fluids* **29** (1986) 731.
- [88] Y. M. Li, S. M. Mahajan, and D. W. Ross, *Phys. Fluids* **30** (1987) 2101.
- [89] R. R. Mett and S. M. Mahajan, *Phys. Fluids B* **4** (1992) 2885.
- [90] M. S. Chu, A. D. Turnbull, J. M. Greene, *et al.*, in *Plasma Physics and Controlled Nuclear Fusion Research 1992*, (International Atomic Energy Agency, Vienna, 1993), Vol. 2, p. 71.

- [91] R. D. Bengtson, J. F. Benesch, G. L. Chen, *et al.*, in *Proceedings of the 2nd Joint Varenna-Grenoble Symposium on Heating in Toroidal Plasmas*, edited by E. Canobbio, H. P. Eubank, G. G. Leotta, *et al.*, Grenoble, France, (CEC, Brussels, 1982), Vol. I, p. 151.
- [92] T. E. Evans, P. M. Valanju, J. F. Benesch, *et al.*, *Phys. Rev. Lett.* **53** (1984) 1743.
- [93] Y. P. Pao, *Nucl. Fusion* **15** (1975) 631.
- [94] E. Tennfors, *Plasma Phys. Controlled Fusion* **28** (1986) 1483.
- [95] V. V. Dolgoplov, A. V. Kryukov, and S. S. Romanov, *Phys. Fluids* **31** (1988) 1649.
- [96] K. Appert, T. Hellsten, J. Vaclavik, *et al.*, *Plasma Phys. Controlled Fusion* **30** (1988) 1195.
- [97] E. F. Jaeger, D. B. Batchelor, and D. C. Stallings, *Nucl. Fusion* **33** (1993) 179.
- [98] A. Jaun, K. Appert, J. Vaclavik, *et al.*, in *Proceedings of the Sherwood Theory Conference*, Lake Tahoe, NV, (1995).
- [99] A. Jaun, *Linear Wave Propagation in a Hot Axisymmetric Toroidal Plasma*, Report LRP 513/95, École Polytechnique Fédérale de Lausanne - Suisse (1995).
- [100] A. G. Elfimov and S. Puri, *Nucl. Fusion* **30** (1990) 1215.
- [101] H. L. Berk, J. W. Van Dam, D. Borba, *et al.*, *Phys. Plasmas* **2** (1995) 3401.
- [102] J. Candy, B. N. Breizman, J. W. Van Dam, *et al.*, *Multiplicity of Low-Shear Toroidal Alfvén Eigenmodes*, Report IFSR #737 (14 pages), The University of Texas (1996).
- [103] K. Appert, B. Balet, R. Gruber, *et al.*, in *Proceedings of the 2nd Joint Varenna-Grenoble Symposium on Heating in Toroidal Plasmas*, edited by E. Canobbio, H. P. Eubank, G. G. Leotta, *et al.*, Como, Italy, (CEC, Brussels, 1980), Vol. II, p. 643.
- [104] L. Villard, K. Appert, R. Gruber, *et al.*, *Computer Phys. Reports* **4** (1986) 95.
- [105] L. Villard and G. Y. Fu, *Nucl. Fusion* **32** (1992) 1695.
- [106] S. C. Chiu, V. S. Chan, R. W. Harvey, *et al.*, *Nucl. Fusion* **29** (1989) 2175.
- [107] C. C. Petty, R. I. Pinsky, M. J. Mayberry, *et al.*, *Phys. Rev. Lett.* **69** (1992) 289.
- [108] R. I. Pinsky, C. C. Petty, M. Porkolab, *et al.*, in *Plasma Physics and Controlled Nuclear Fusion Research 1992*, (International Atomic Energy Agency, Vienna, 1993), Vol. 1, p. 683.
- [109] R. I. Pinsky, F. W. Baity, S. C. Chiu, *et al.*, in *Proceedings of the 21st European Phys. Soc. Conf. on Controlled Fusion and Plasma Physics*, Montpellier, (European Physical Society, 1994), Vol. 18B, Part III, p. 1118.

CHAPTER 4

PHYSICS DESIGN CONSIDERATIONS: CONFINEMENT

In this chapter we address the physics-related issues in the design process. The philosophy has been to design the smallest, least expensive machine which can address the issues expounded in chapters 1 through 3. The scheme for achieving that goal is described in Sec. 4.1. In Sec. 4.2, generalized formulae are discussed for identifying the smallest device capable of achieving the relevant physics goals, and in Sec. 4.3, more exact calculations and performance estimates are described. Note that we are designing a machine suitable for NBI although phase I is Ohmic only.

4.1 Design strategy and logic

Summary of the design process

The scheme followed in designing USTX is outlined in this section and illustrated in Fig. 4.1. Following this procedure has led us to the design presented in later sections:

1. Identify and refine physics relevant to low A , including plasma shape and stability, maximum current-ramp rate, beta limits, density limits, neutral-beam absorption and fast particle orbits, current drive, profile control, etc.
2. Identify and refine engineering constraints, including solenoid volt-seconds for a given size core (considering material strength and thermal characteristics), power supplies, toroidal field for a given toroidal-field post size, heat flux limitations on plasma facing components, and forces on the vessel, center core, and toroidal-field return legs during normal operation and disruptions.
3. Research the present state of experimental data and theoretical understanding pertinent to developing a low- A fusion reactor. Identify present accomplishments and unknowns in terms of key physics and engineering parameters.

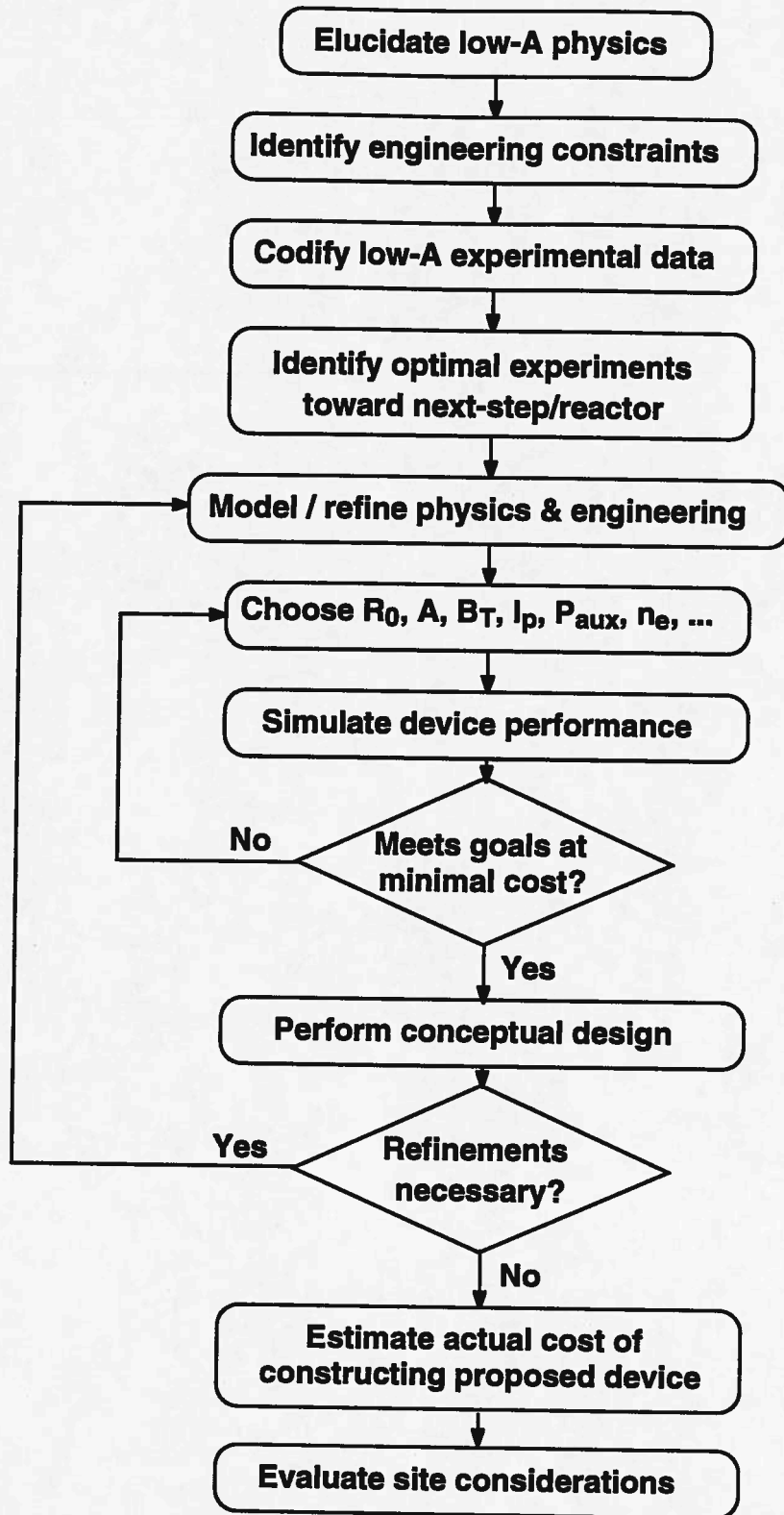


FIG. 4.1. Flowchart of the USTX design process

4. Identify what constitutes a significant but achievable improvement in key physics parameters. Identify the experiments necessary to improve estimates of low- A reactor performance and to allow an informed design of a next-step (2 - 5 MA, or neutron source) device such as those tentatively proposed by ORNL and General Atomics. Consider other contributions USTX could make to the national fusion program including development of current-drive techniques, heat flux handling, disruption avoidance, and advances in basic plasma physics.
5. Model physics and engineering constraints and uncertainties as realistically as possible.
6. Choose test-device parameters: R_0 , A , B_T , I_p , P_{aux} , n_e , and their ranges of variation.
7. Simulate device to estimate performance, flexibility, sensitivity to assumptions regarding transport and profiles, and the probability of reaching the designated goals.
8. Estimate overall performance, size, and cost of the device.
9. Adjust device parameters and iterate to reach optimum performance and cost.
10. Perform a conceptual-device design to refine engineering constraints and requirements.
11. Having completed sufficient iterations on the preceding steps to reach closure, refine the conceptual design to a point sufficient to establish a defensible cost estimate.
12. Evaluate the impact of site considerations and make minor adjustments if necessary, but carefully note any compromises dictated by site limitations.

4.2 Smallest credible machine size

Here we consider the smallest machine with which we can investigate the equilibrium, stability and confinement properties of a tokamak dominated by the physics at low aspect ratio. From the ignition scenarios described in chapter 2, we understand that

important aspect ratios to investigate are $A \approx 1.4$ (the delineating aspect ratio between peaked and hollow current profiles at a $q = 3.2$) and $A \approx 1.25$ (the aspect ratio where neutron wall loading is reduced to a level comparable to that at normal aspect ratio). Therefore, we find the smallest machine which, by replacing the inner vessel cylinder and ohmic-heating core only, will allow operation at both $A \approx 1.4$ and $A \approx 1.25$, and in which:

- 1) The confinement properties are dominated by the physics at low aspect ratio.
- 2) $\beta_N \approx 3 - 5$ can be obtained.
- 3) Neutral beams can ultimately be used for heating or current drive.

We have designed a machine (USTX-0) to accommodate a plasma with an aspect ratio $A^{(0)} = 1.43$ and $R_0 \approx 0.7$ m. The outer major-radial vessel wall is well separated from the nominal plasma surface to allow scaling studies, to allow space for current-drive antennas, and to allow an ultimate $A^{(2)} = 1.25$ capability (USTX-2) which necessitates a larger plasma. This displaced wall also permits operation (called USTX-1) down to $A^{(1)} > 1.33$ with the same solenoid used for USTX-0. The inner vessel wall and ohmic solenoid will be replaced to allow operation at $A^{(2)} \geq 1.25$ (but with reduced inductive I_p). It remains to determine the major radii $R_0^{(0)}$ and $R_0^{(2)}$. In general larger R_0 is better for confinement studies, while smaller R_0 is better for beta limit studies, as long as beam absorption is adequate. These studies must be performed under relevant plasma conditions, i.e., in the correct dimensionless parameter space [1]. This is addressed later.

Confinement properties

Consider a low-aspect-ratio plasma with aspect ratio A , major radius R_0 , and horizontal minor radius (i.e., at the equator) $r = a$ at the plasma edge. Near the center of the plasma, i.e., $r = 0$, the local aspect ratio becomes arbitrarily large. At some radius $r_1 \equiv R_0 / A_n$, where $A_n \approx 3.5$ is a 'normal' aspect ratio, the local aspect ratio is equal to that at the edge of a normal aspect ratio plasma. We now divide the low- A plasma into three regions in the normalized minor radius $\rho = r / R_0$. These are shown in Fig. 4.2, and described below.

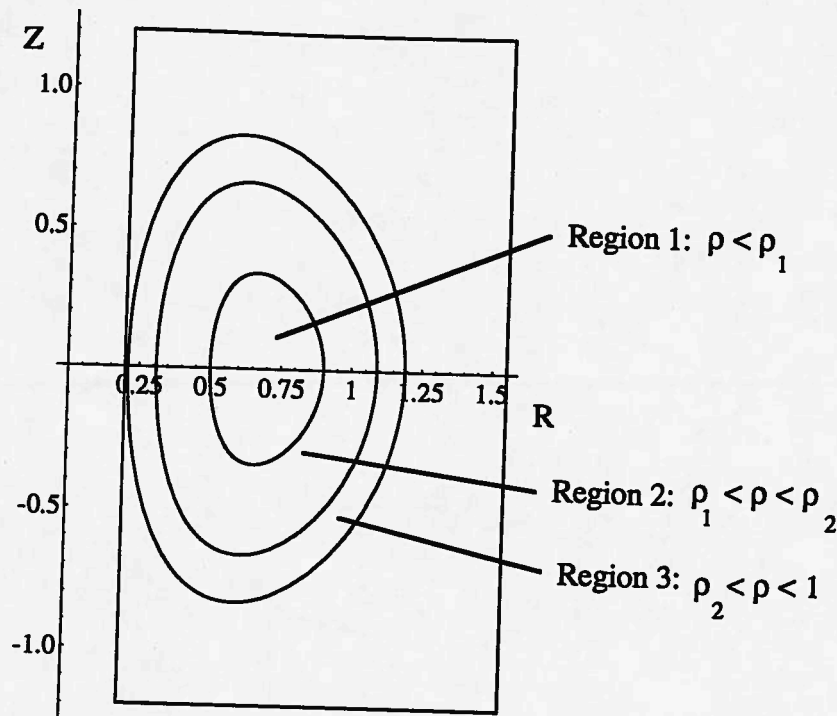


FIG. 4.2. The three plasma regions considered.

Region 1: $0 \leq \rho < \rho_1 \equiv r_1/a = A/A_n$, is the high-aspect-ratio region with $A > A_n$.

Region 2: $\rho_1 \leq \rho < \rho_2 \equiv 1 - \lambda_{\text{rad}}/a$ where $\lambda_{\text{rad}} \approx 0.1$ m (from low density TEXT data) is the distance into the plasma where the dominant energy loss mechanism is not thermal conduction, but radiation, charge exchange, and convection. Therefore, region 2 delimits that part of the plasma with low aspect ratio, which is dominated by thermal conduction.

Region 3: $\rho_2 < \rho < 1$ is that part of the plasma in which energy losses are not attributable to thermal conduction.

We also impose the following constraints:

1. To readily observe equilibrium-parameter gradients and turbulence characteristics which can be attributed to low aspect ratio, and which are uncontaminated by atomic processes, approximately a third of the minor radius should be in region 2.

2. To readily diagnose (for example with a diamagnetic loop) global confinement properties and changes which can be attributed to low aspect ratio, and which are uncontaminated by atomic processes, approximately half of the stored energy should be in region 2. An energy density profile of the form $W = W_0(1 - \rho^2)^\alpha$ is assumed, with $\alpha = 0$ (flat) or $\alpha = 3$ (peaked). Then, the fraction of stored energy in region 2 is,

$$R_W \equiv \frac{\int_{A/A_n}^{1-\lambda_{rad} A/R_0} (1-\rho^2)^\alpha \rho d\rho}{\int_0^1 (1-\rho^2)^\alpha \rho d\rho} \geq \frac{1}{2}$$

3. To readily observe and interpret test-particle transit times in terms of diffusivities which can be attributed to low aspect ratio, and which are uncontaminated by atomic processes, approximately a third of the minor radius squared should be in region 2. This is equivalent to criterion 2 with $\alpha = 0$

The most restrictive of criteria 1 through 3 are shown as contours in R_0 - A space in Fig. 4.3. For low aspect ratio, the criterion 2 with $\alpha = 0$ is limiting, while for higher aspect ratio, the limit is determined by $\alpha = 3$. The break point in each of the three solid lines is the point where the limiting value of α changes from 0 to 3. For a machine with $A^{(0)} \approx 1.4$ to be dominated by low-aspect-ratio energy confinement, it must have $R_0^{(0)} \geq 0.7$ m, while for $A^{(2)} \approx 1.25$ it must have $R_0^{(2)} \geq 0.6$ m. The superscripts refer to three variations of USTX (described in the previous sub-section) based on the final conclusions of this section. Also shown are representative points for some past and present devices, and GLOBUS (currently under construction). Note that none of the past or present machines shown (START [2, 3], MEDUSA [4], TS-3 [5], CDX-U [6], HIT [7], FBX II [8]) meets the criteria, though FBX-II comes closest.

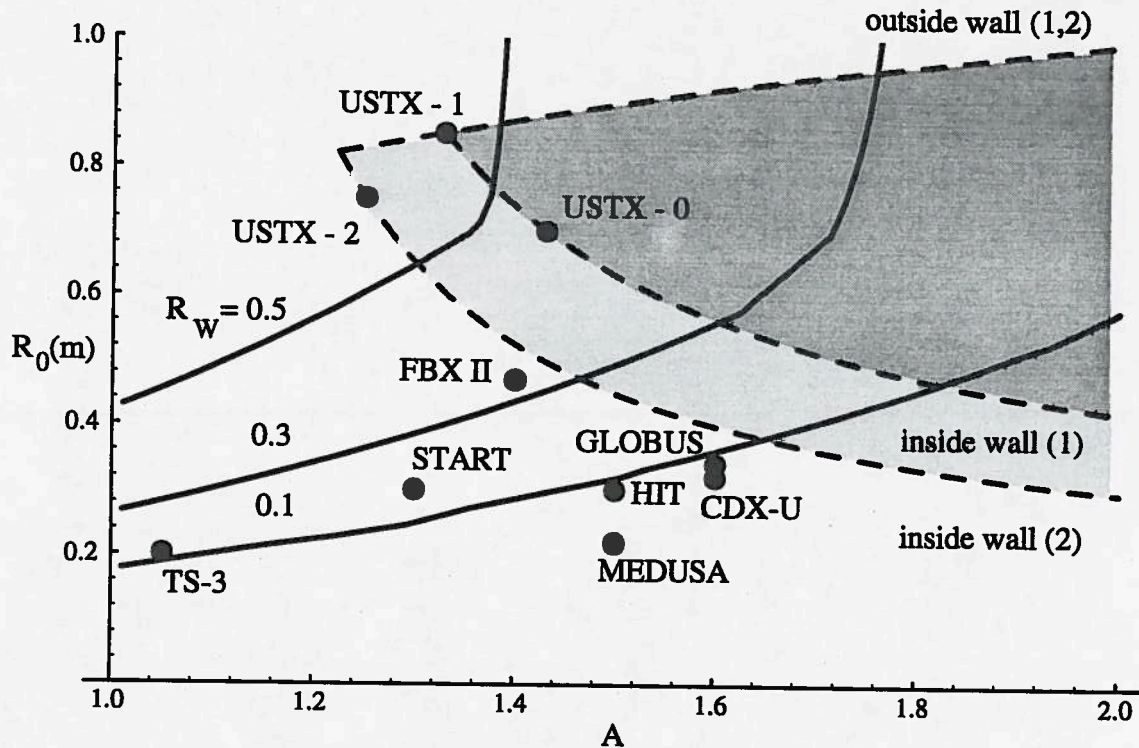


FIG. 4.3. Confinement properties of machines past, present, and under construction. The solid lines marked $R_w = 0.5, 0.3$ and 0.1 are the contours for which a machine will have 50%, 30%, and 10% of its energy in the low-aspect-ratio regime.

The broken lines in Fig. 4.3 depict the relationship between aspect ratio and major radius in USTX. They are obtained by moving the plasma within the vessel, and assuming that the vessel geometry restricts the aspect ratio. The outside wall remains fixed. USTX-0 and USTX-1 have the same inner wall, while USTX-2 has a different inner wall. The dark shaded area illustrates the available space (using movable limiters) which can be accessed in the first vacuum vessel, while the light shaded area indicates the additional area which can be accessed in USTX-2 by replacing the inner vessel cylinder of USTX-1.

From this analysis we conclude that it is necessary that $R_0 \geq 0.6$ m for $A = 1.25$, and $R_0 \geq 0.7$ m for $A = 1.25$ if low- A physics is to dominate energy confinement times. We next consider what device size is required for a low-aspect-ratio tokamak to reach reactor-relevant values of β .

Troyon coefficient

The device should be able to test beta limits [9] and to exceed the values produced by normal-aspect-ratio tokamaks, i.e., to achieve

$$\beta_N \equiv \frac{\langle \beta \rangle (\%) B_{T0} (T) a (m)}{I_p (MA)} \geq 3, \text{ where } \langle \beta \rangle = \frac{2\mu_0 \langle p \rangle}{B_{T0}^2}.$$

Detailed calculations of expected plasma parameters are presented in Sec. 4.3; here we simply wish to derive trends to allow us to estimate the range of major radii to consider. To estimate the values of β_N which can be achieved as a function of the point-design values of R_0 and A we have

1) derived an analytic fit to numerical predictions (described in Secs. 5.1 and 6.2) for the maximum plasma current achievable from a given ohmic solenoid in terms of R_0 and A . Both conductor mechanical and thermal constraints were taken into account. For a given A , reducing R_0 allows less room for the ohmic solenoid, and thus less plasma current can be driven inductively. No credit is taken for volt-seconds produced by the other poloidal-field coils. The analytical result is accurate to within 10% only within the approximate limits $1.25 < A < 1.6$, and $0.4 \text{ m} < R_0 < 0.8 \text{ m}$. This is sufficient for the purposes of this section (determining approximate conditions); more accurate estimates of machine performance are given in chapter 6.

2) assumed that the elongation varies with aspect ratio and internal inductance as calculated for a set of decay index $n = 0$ equilibria (i.e., 'naturally elongated') [10].

3) assumed, as in chapter 2, a confinement scaling for τ_E of the form proposed by Goldston (Goldston L-mode) [11], namely

$$\tau_E (s) = c H I_p (A) P_\Sigma (W)^{-0.5} \kappa^{0.5} R_0 (m)^{\alpha_R} a (m)^{\alpha_a},$$

where for L mode $c = 3.7 \times 10^{-5}$, $\alpha_R = 1.75$, and $\alpha_a = -0.37$. We take $H = 1.6$.

4) assumed a loop voltage of 1.5 V.

5) assumed auxiliary heating power equivalent to one neutral beam with 1.25 MW of power absorbed by the plasma.

6) restricted B_{T0} to greater than 0.15 T (for beam deposition, ease of breakdown, and magnetic island size considerations) and $q > 3.2$.

The results, dependent on the assumed confinement scaling (see Sec. 4.3), are shown as contours of expected β_N in R_0 - A space in Fig. 4.4 for an auxiliary power of 1.25 MW. Also shown is β_N vs. R_0 in Fig. 4.5a for aspect ratio $A^{(0)} = 1.43$, and in Fig. 4.5b for aspect ratio $A^{(2)} = 1.25$, in both cases for ohmic and auxiliary-heated discharges. The maximum ohmic plasma current I_p is used, and the minimum toroidal field B_{T0} consistent with $q > 3.2$ or $B_{T0} > 0.15$ T. For $A = 1.25$ the important restriction on I_p comes from $B_{T0} > 0.15$ T; if the restriction to I_p were only $q > 3.2$, then larger values of β_N could be obtained.

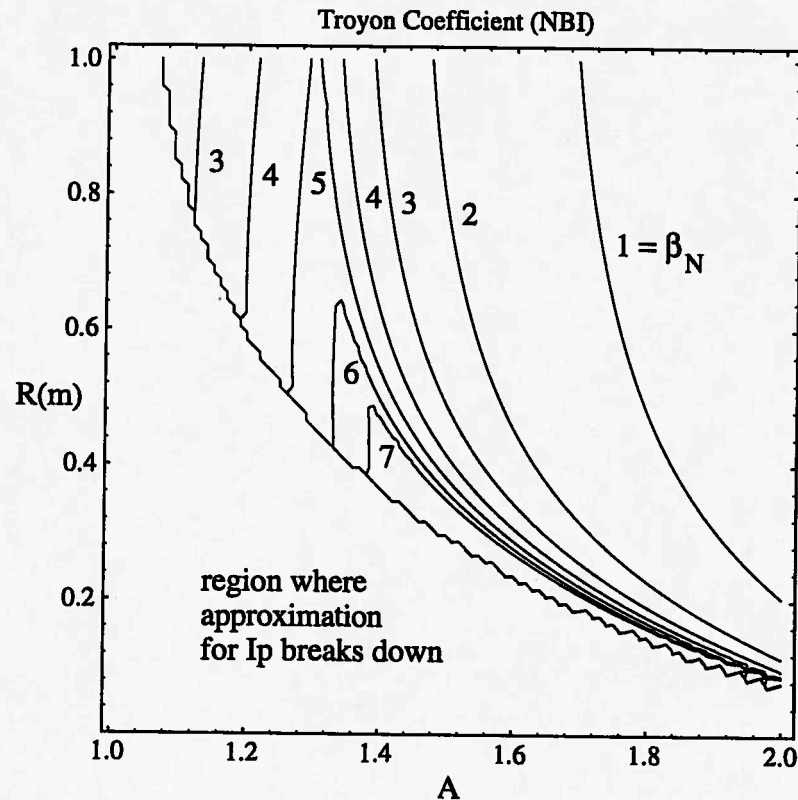


FIG. 4.4. Contours of expected Troyon coefficient β_N for $P_{\text{aux}} = 1.25$ MW, using the maximum I_p available, and the minimum B_{T0} consistent with $q > 3.2$ or $B_{T0} > 0.15$ T, assuming Goldston L-mode scaling.

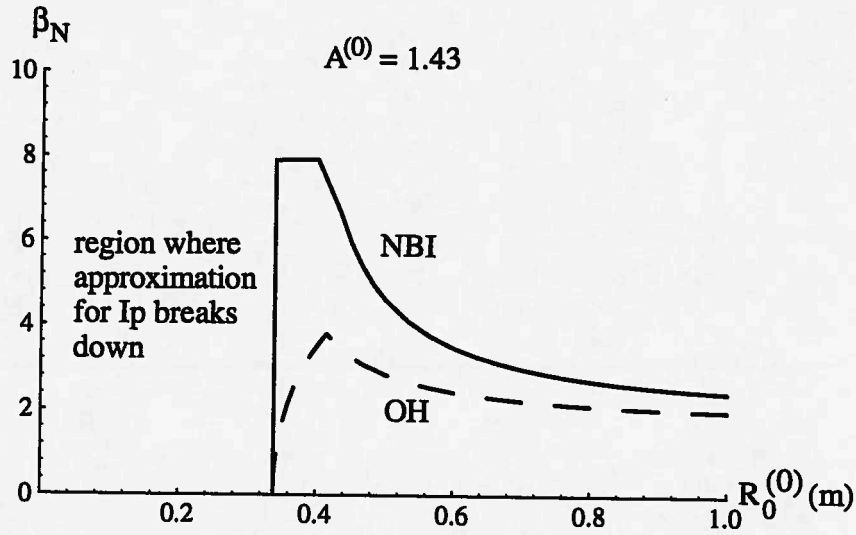


FIG. 4.5a. The Troyon factor β_N vs. $R_0^{(0)}$ for USTX-0 with $A^{(0)} = 1.43$, for ohmic (dashed line, OH) and neutral-beam cases (solid line, NBI).

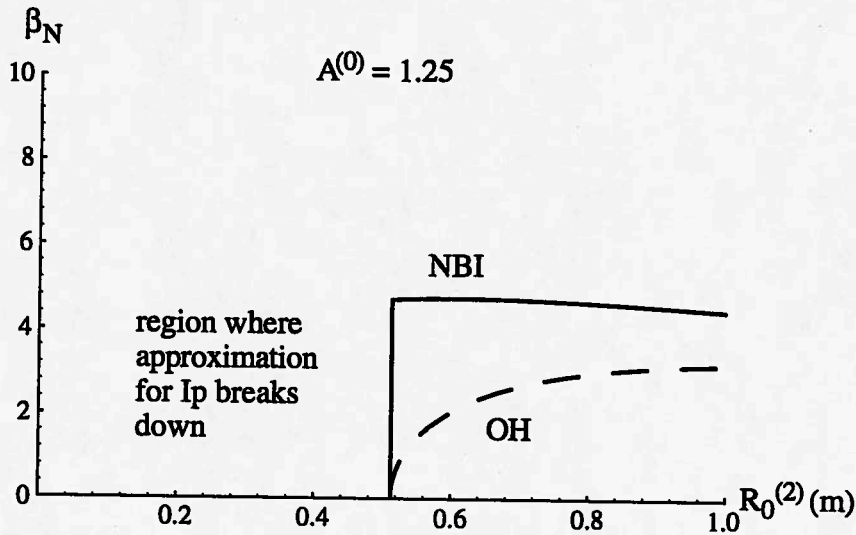


FIG. 4.5b. The Troyon factor β_N vs. $R_0^{(2)}$ for USTX-2 with $A^{(2)} = 1.25$, for ohmic (dashed line, OH) and neutral-beam cases (solid line, NBI).

For $A^{(0)} = 1.43$ there is a value of major radius $R_0 \approx 0.4$ m above which q restricts I_p and β_N , and below which B_{T0} restricts I_p and β_N . Smaller machines allow access to larger β_N only as long as q is limiting I_p . We conclude that with $A^{(0)} = 1.43$ it is marginally possible to access $\beta_N \approx 3$ for ohmic discharges if $0.4 \text{ m} < R_0 < 0.5 \text{ m}$, and with 1.25 MW of auxiliary heating if $R_0 < 0.7 \text{ m}$. The lower limit is not available with the

approximations used here in the analytic expression for I_p , but it is $R_0 > 0.35$ m (based on a fit to I_p for small R_0). With $A^{(2)} = 1.25$ it is marginally possible to access $\beta_N \approx 3$ for ohmic discharges if $R_0^{(2)} < 0.8$ m. With 1.25 MW of auxiliary heating, the lower limit to R_0 is not available with the approximations used here (as above), but it exceeds 0.5 m.

Neutral beam accessibility

The results described above take no account of whether the proposed 40-keV neutral beam will be absorbed in the target plasma. Restricting to $B_{T0} > 0.15$ T and a reasonable $I_p > 300$ kA ensures that beam first-orbit losses are less than 15% for co-injection; counter-injection first-orbit losses are much larger.

The proposed point designs ($R_0^{(0)}, A^{(0)}$ and $R_0^{(2)}, A^{(2)}$) must provide sufficient plasma current that the density achieved, limited by the Greenwald value [12-14], is sufficient to absorb the beam. The beam absorption depends on the integral of the density along the beam path with length l . Calculations using a beam-penetration code indicate that there is more than 15% shine-through, which is unacceptable, for $\int n dl \equiv \bar{n} l < 0.4 \times 10^{20} \text{ m}^{-2}$. Hence the minimum possible $\bar{n} l$ along the beam path should be approximately $0.4 \times 10^{20} \text{ m}^{-2}$. This also agrees with results from ISX-B neutral injection [15], which exhibited a beam deposition (shine-through) problem for line-of-sight densities $\bar{n} < 2.5 \times 10^{19} \text{ m}^{-3}$, with a path length $l \approx 1.5$ m. Therefore we take $(\bar{n} l)_{\min} \approx 0.4 \times 10^{20} \text{ m}^{-2}$, which is a much simpler, yet quite accurate criterion. In order to compare this minimum requirement with the Greenwald limit on density we define the parameter

$$K = \frac{(\bar{n} l)_{\min}}{l(I_{p\max} / \pi a^2)},$$

which is a function of A , R_0 , and the beam tangency radius R_{beam} , and describes the minimum current we must achieve in the target plasma to ensure neutral-beam absorption without raising the density beyond the Greenwald limit. Specifically K is the product of the operational minimum fraction of the Greenwald density limit and the fraction of the maximum possible plasma current (both functions of R_0 and A).

An absolute upper limit on K is unity (i.e., operation at maximum current and maximum density); we consider $K = 0.5$ a practical upper limit. We use $R_{\text{beam}} = 1.15 R_0$ here to represent the upper limit of a beam displaced outward from the geometric axis, for

example to drive current displaced from the magnetic axis. In Fig. 4.6, K is plotted as a function of R_0 for various low values of A . As A is lowered, the available inductively driven plasma current is reduced, and the minimum vessel major radius required to achieve a given K is increased. For $A = 1.25$ we find $R_0 \geq 0.78$ m to ensure $K \leq 0.5$, i.e., operation at half the Greenwald limit for maximum plasma current. For $A = 1.43$ we find (not shown) $R_0 > 0.6$ m to ensure $K \leq 0.5$. We note that if the chosen tangency radius is reduced, the constraints on R_0 are less severe, so $R_0 = 0.75$ m is a reasonable value for $A = 1.25$.

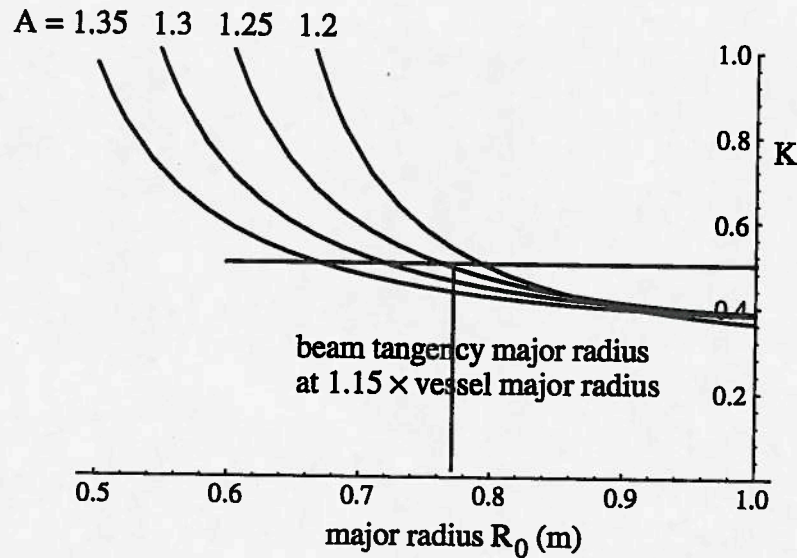


FIG. 4.6. The K factor as a function of vessel major radius R_0 for various A .

Summary: choice of machine size

Table 4.1 summarizes the results, and the values of major radius $R_0^{(0)}$ and $R_0^{(2)}$ chosen to satisfy the constraints. Having defined $A^{(0)}$, $R_0^{(0)}$, $A^{(2)}$, and $R_0^{(2)}$; the outer wall position is constrained. Note that the choice of the major radius $R_0^{(2)}$ in the low aspect ratio $A^{(2)} = 1.25$ case is determined by the neutral-beam absorption criterion. This in turn depends on the plasma current which can be driven inductively, which can only be estimated after initial experiments are performed at $A = 1.43$.

The final values of R_0 shown have been determined by more accurate calculations than those outlined above, but the results are in general accord with our discussion. It may be possible to increase the plasma current above the values used here if both a) a smaller

toroidal field proves feasible, permitting a smaller TF post and thus leaving more room for the ohmic solenoid, and b) if the plasma internal inductance can be reduced (a necessity at low q and low A). The confinement criteria restrict $R_0^{(2)}$ to greater than 0.6 m; depending on the confinement scaling, this may allow larger β and β_N to be obtained. Higher beam absorption can be achieved at lower values of density if lower beam energies (re-gapping the source) or a different beam-species mix is used. Therefore, the precise details of the optimum low- A USTX-2 case must depend on the results from operation of USTX-0 and USTX-1.

Table 4.1. Restrictions on machine major radius

	$A^{(0)} = 1.43$	$A^{(2)} = 1.25$
confinement studies	$R_0 > 0.7$ m	$R_0 > 0.6$ m
beta studies (ohmic)	$0.4 \text{ m} < R_0 < 0.5 \text{ m}$	$R_0 > 0.8$ m
beta studies (beam)	$0.35 \text{ m} < R_0 < 0.7 \text{ m}$ (0.35 is over-estimate)	$R_0 > 0.5$ m (over-estimate)
neutral beam absorption	$R_0 > 0.6$ m	$R_0 \geq 0.78$ m (over-estimate)
final value	$R_0^{(0)} = 0.7$ m	$R_0^{(2)} = 0.75$ m

4.3 Device optimization studies, performance estimates and flexibility

Having set the range of machine sizes, we next explore the design to optimize machine performance and flexibility. That is, although we are designing to a specific geometry, we must have enough flexibility to explore many plasma geometries (i.e., different shapes, aspect ratios) around this point.

USTX must be designed to explore a wide enough range of parameters to allow discrimination among various scaling expressions, and make reasonably accurate predictions for future spherical tokamaks. Since various aspects of the design are closely interrelated, it is important to use design-prediction tools which incorporate both engineering and physics constraints, and are modular enough to allow us to add more information as it becomes available. It is also important to use independent tools to cross-check the results and reduce the possibility of systematic errors. We use four independent

zero-dimensional programs (the OPT optimization spreadsheet [16], two FORTRAN programs S1 and S2, and a Mathematica notebook ST) which we have developed to explore various aspects of the design. (The OPT spreadsheet is partly based on a spreadsheet written by Nevins [17].) We have spot-checked these against the one-dimensional model discussed in chapter 3 [18], using both a plasma-profile spreadsheet and a time-dependent simulation code that we have developed [18, 19]. The 1-D model takes into account low aspect ratio, shaping, and neoclassical effects.

The four zero-dimensional codes we have developed use appropriate temperature and density profiles $T_e \propto (1-\rho^2)^{\alpha_T}$, and $n_e \propto (1-\rho^2)^{\alpha_n}$, and volume-averaged quantities accounting for elongation and triangularity where applicable. They all incorporate operational and stability limits and eleven confinement scaling relations. The latter are *neo-Alcator* [20], *Lackner-Gottardi* [21], *Rebut-Lallia-Watkins (RLW)* [22, 23], *Goldston and Goldston-quadrature* [11], *Kaye-Goldston* [24], *Kaye-all* [25, 26], *ITER-89P* [27], *DIII-D-ohmic (D-III-OH)* [28], *DIII-JET* [29], and *dissipative-trapped-electron mode (DTEM)* as given by Perkins [30, 31]. Various subsets of these are reviewed in the Refs. [25, 26, 32].

In these confinement scaling relations, except as noted, we use q_{cyl} where the safety-factor dependence is explicit. For example, in the Lackner-Gottardi expression

$$\tau_E = 0.12 H \sqrt{A_i/2} a^{2/5} R_0^{9/5} \kappa (1 + \kappa)^{-4/5} I_p^{4/5} q_{\text{cyl}}^{2/5} (\bar{n}_{e20} / P_{\text{tot}})^{3/5}$$

with A_i the plasma effective atomic mass, q_{cyl} is explicitly used. However, the moderate- A experiments, from which the expression was derived, probably do not allow one to accurately distinguish between q and q_{cyl} . Note that where A_i appears in the confinement scaling relations, OPT accounts for dilution of the effective atomic mass by both beam particles and cold beam gas using scaled results from ISX-B [33]. This refinement was suggested by Stan Kaye [34].

The codes have been benchmarked against START confinement data and analysis, and against the analysis of NSTX by the group at PPPL. The inputs include the working gas, A , R_0 , κ , I_p , B_{T0} , volume-averaged density $\langle n_{e20} \rangle$ (in units of 10^{20} m^{-3}), Z_{eff} , H , and P_{aux} . They compute q_{cyl} (including corrections for elongation and triangularity) and q from Peng's formula [35] (essentially identical to the ITER formula [36]), and plasma resistivity from a Spitzer-like formula scaled to START data. They self-consistently compute, for the eleven different scaling relations, $T_e(0)$, $\langle T_e \rangle$, τ_E , β , β_N , and a number of

other quantities. The ion temperature is approximated by a fit to both Ohmic and L-mode data from the MFEDB database [37] for TFTR, DIII-D, and JT-60.

The OPT spreadsheet is well suited to manually explore the parameter space to determine the effect of varying a single parameter. The programs S1 and S2 allow rapid optimizations with constraints, comparisons among various scaling relations, and exploration of "what-if" scenarios. The workbook ST is aimed at studying the problems in terms of dimensionless parameters and scalings. To date, only OPT include the stored energy contribution of circulating fast particles introduced by the neutral-beam injection. This improvement to OPT was also suggested by Stan Kaye [34], and was found to make at most a 15% correction to energy balance calculations for the cases considered.

Device performance estimates and flexibility

One of the first criteria in the design of USTX is that it should be flexible enough to provide adequate resolution to distinguish among confinement scaling expressions. This is especially pertinent in light of the lack of aspect-ratio scalings in the ITER confinement database. This question has been studied using the routine S2, which explores the predictions (based on the various scaling expressions) for machine performance in a multi-dimensional parameter space. The ranges of the five input parameters used for USTX-0 are give in Table 4.2 where GrwFract is the fraction of Greenwald density limit for a particular case. In addition, we set $\delta = 0.4$, and used the natural elongation fitted to the results of Kalmykov [10] (see discussion in Sec. 3.2). We are aware that more recent studies indicate some differences from Kalmykov, but these corrections do not significantly impact our analysis. We have carried out this study for a range of auxiliary heating options (described in FRC report #468). Here, however, we focus on the Ohmic Phase I scenarios, which are described in chapter 9, and find even in this case a significant range of predicted performance.

Table 4.2. Range of S2 input parameters used for USTX-0

	R_0 (m)	A	I_p (MA)	B_T (T)	GrwFract
Minimum	0.6	1.33	0.2	0.25	0.2
Maximum	0.8	1.63	1.0	0.60	0.8

We have found that a useful way of summarizing the results is in the form shown in Table 4.3. Each diagonal element of the table shows the ratio of the maximum to the

minimum value of energy confinement time τ_E predicted by the i 'th scaling relation for operation within the parameter range specified. The (i,j) off-diagonal elements show the maximum ratio of $\tau_E(\text{row}=i)/\tau_E(\text{column}=j)$ in the upper and lower halves for the i 'th and j 'th scaling relations. For each (i,j) pair, the best τ_E ratio is the larger of the (i,j) 'th and the (j,i) 'th element. Note that entries symmetrically located about the diagonal are generally not inversely related since different input conditions are chosen to maximize each element. Higher numbers indicate good separation between the predictions of the two expressions involved. For example, the table below shows that Goldston-quadrature and RLW are very well resolved (max τ_E ratio = 65), while Goldston-L and ITER-89P are not as well resolved by USTX (max τ_E ratio = 1.4). On the average, we obtain a maximum ratio of 11.3 between τ_E 's for scaling relation pairs. The minimum to maximum τ_E variation within each scaling relation is at least a factor of 2.8, with some varying much more. This data will allow significantly better projections for an ST reactor than are presently possible.

In addition to computing the ratios of predicted confinement times, the program computes the maximum τ_E , β , and β_N for each scaling relation, shown in Table 4.4. (For the auxiliary heated cases, values obtained with the OPT code are given later in Table 4.6.) The code also produces a set of operating conditions (input parameters) which are best suited to resolve the scaling relations. This list consists of about twenty "discharges" which will be used as a blueprint for experiments on USTX to determine which if any of the empirical scaling relations derived for normal-A tokamaks apply at low A . These studies (described in chapter 9) will require only a few well-diagnosed cases with full profile analysis.

Table 4.3. Confinement-time ratios for Ohmic discharges

	DIII-JET	DIII-OH	DTEM	Gold-quad	Gold-L	ITER-89P	Kaye-all	Kaye-Gold	Lack-Got	Neo-Alc	RLW
DIII-JET	4.3	6.2	4.62	21	0.8	1.0	0.8	1.6	2.2	12	0.7
DIII-OH	1.0	5.8	2.1	6.6	0.7	0.5	0.4	1.2	0.5	2.4	0.1
DTEM	1.4	7.8	11	6.2	1.2	1.3	1.0	0.7	1.4	5.6	0.6
Gold-quad	0.5	1.6	0.8	13	0.3	0.3	0.2	0.5	0.3	0.9	0.1
Gold-L	1.5	8.0	6.8	31	3.7	1.4	1.1	2.4	3.4	18	1.1
ITER-89P	1.8	6.6	6.3	26	1.3	3.4	0.8	2.5	2.6	14	0.9
Kaye-all	2.9	8.8	8.3	33	2.0	1.6	2.8	3.4	3.7	20	1.3
Kaye-Gold	2.4	12	3.2	20	1.8	2.0	1.5	6.1	2.5	13	1.1
Lack-Got	2.8	5.9	5.1	12	2.0	1.6	1.1	3.6	7.0	5.5	0.4
Neo-Alc	1.7	1.8	3.2	4.0	1.2	1.0	0.7	2.2	0.6	24	0.2
RLW	1.3	22	39	65	15	12	8.7	27	7.6	24	18

Table 4.4. Maximum confinement times and betas

	DIII-JET	DIII-OH	DTEM	Gold-quad	Gold-L	ITER-89P	Kaye-all	Kaye-Gold	Lack-Got	Neo-Alc	RLW
τ_E (ms) Max	54	23	67	14	67	55	68	97	65	40	497
τ_E (ms) Min	12	3.9	6.2	1.1	18	16	24	16	9.3	1.7	27
β_N Max	3.5	1.8	4.0	2.1	3.8	3.6	4.2	4.8	3.5	2.3	5.0
β (%) Max	22	8.4	26	14	24	23	19	31	23	10	32

Beta-limit studies

Normalized beta optimization

In this section we consider the feasibility of achieving either the reactor relevant regime of $\beta_N = 3$ (see section 2.1) or the more aggressive stability limit of $\beta_N = 5$ [38]. An important realization is that it is advantageous to optimize parameters separately for each scaling relation and for each physics goal. Using known physics constraints and a range of operating parameters, and assuming a conservative H-factor of 1.6 consistent with $H^0 \rightarrow D^+$ and Ohmic H-mode (see chapter 3), we have used the OPT code to determine the optimum plasma configuration for each scaling relation. We have also performed some sensitivity studies noting, for example, that for Lackner-Gottardi, RLW, and Kaye-Goldston, the power required to reach $\beta_N = 5$ is a strong function of the achievable plasma density limit. For all of the scaling relations, β increases fairly slowly with P_{aux} , so doubling β is very expensive. However our analysis indicates that very high values of β should be achievable with Ohmic heating only.

In performing the present analysis, we have restricted ourselves, except as noted, to the following range of parameters: $A = 1.25 - 1.7$, $R_0 > 0.55$ m, $\kappa = 1.2 - 2.2$, $\delta = 0.1 - 0.5$, $I_p = 0.65$ MA to $I_{p \text{ max}}$ (predicted for USTX Ohmic cases by an analytic fit to filament model runs for either the $A = 1.25$ or $A = 1.43$ solenoids with $l_i = 0.3$ or 0.7 respectively, and taking no credit for volt-seconds produced by other PF coils), $0.3 \text{ T} < B_{T0} < \max(B_{T0})$ (given the present power supply and twelve single-turn coils), $q > 3.2$, \bar{n}_e less than 0.8 times the Greenwald limit, $\alpha_n = 0.7$, $\alpha_T = 1.0$, and $Z_{\text{eff}} = 2$. We also constrain the plasma geometry such that it fits within the USTX vessel on all sides accounting for the variation in R_{in} between the $A = 1.25$ and 1.43 solenoids. To understand the ultimate performance of this machine, we have also considered cases with neutral-beam heating. For neutral-beam injection with one (or two beams only for a few cases as noted), we restrict the injected power to 1.25 MW (1.5 MW) per beam at $E_{\text{beam}} = 40$ keV (60 keV). Note that OPT does not guarantee MHD stability of high-beta plasmas, but for the purposes of this section, we assume that reaching a beta stability limit can be deemed a success for USTX.

Based on this analysis, we find that for each of the scaling relations, it is possible to achieve $\beta_N = 3$ with a total input power P_{tot} of under 1.9 MW. For each scaling relation studied, it is possible to achieve $\beta_N = 3$ with Ohmic heating alone, with the exception of

neo-Alcator with which $\beta_N = 2.8$ can be achieved. Similarly it is possible to achieve $\beta_N = 5$ with $P_{\text{tot}} < 3.3$ MW, and $P_{\text{NB}} < 2.4$ MW. In every case except neo-Alcator and Goldston-quadrature, $P_{\text{NB}} < 1.25$ MW is sufficient assuming q_{cyl} is used in the scaling relation. All of these results were obtained with the $A = 1.43$ solenoid. Using the $A = 1.25$ solenoid, there is no essential physics change; only the minimum A for a given R_0 is reduced and $I_{p \text{ max}}$ is reduced, taking no credit for non-inductive current drive. If we reduce the target plasma current to the 400 to 600 kA range and use $R_0 \geq 0.5$ m, it is possible to achieve $\beta_N = 5$ with $P_{\text{NB}} \leq 1.5$ MW for each of the scaling relations except Goldston-quadrature where $\beta_N = 4.7$ is reached. Note that while the $A = 1.25$ solenoid is necessary for various physics experiments leading to a reactor, the higher inductive current capability of the $A = 1.43$ solenoid will make it more attractive for initial high-beta experiments.

The high- β_N optimization is accomplished in most cases by reducing B_{T0} to 0.3 T and reducing R_0 and I_p from the nominal values. If one assumes that q (i.e., q_ψ rather than q_{cyl}) is appropriate to use in the neo-Alcator, Lackner-Gottardi, and Goldston-quadrature studies (which seems likely from our analysis), then $\beta_N \geq 4.75$ can be achieved in every case with a single neutral beam. If the achieved H-factor reaches 2, (e.g., by injecting D^0 into D^+ , or by good wall conditioning), or if we can run with $B_{T0} < 0.3$ T, or if elongation can be favorably controlled, or other constraints are slightly relaxed, it should be possible to investigate the β limits at low aspect ratio for any of the scaling relations with $P_{\text{tot}} < 1.5$ MW. Indeed, as we have seen in Table 4.4, we find that, according to many of the scaling laws, high β_N should be possible even for ohmic discharges. While none of these possibilities is guaranteed, the enormous cost-savings implied suggest investigating these approaches, along with separate optimization for each scaling relation, before investing in expensive beam power.

Note that if we require the nominal device parameters, $R_0 = 0.7$ m, $A = 1.43$, $I_p = 1$ MA, $B_{T0} = 0.5$ T, $\langle n_{e20} \rangle = 0.5$, and $\kappa = 1.6$, to be used in each case, we pay an enormous penalty. In this case an average neutral beam power $P_{\text{NB}} = 5.4$ MW is required (ranging from 1.6 to 8.6 MW for the various scaling relations) to achieve $\beta_N = 5$. But, by optimizing the plasma configuration for the various scaling relations and physics issues, we can significantly reduce the required beam power and cost of the experiment.

The results shown in Table 4.5 are for more restrictive conditions than those discussed above to demonstrate that it is not necessary to significantly compromise the plasma size or aspect ratio to achieve high β_N . In particular $R_0 \geq 0.6$ m, $I_p = 0.7$ to 1.0

MA, $A \leq 1.6$, $1.2 < \kappa < 2$. The neutral-beam power has been restricted to either 1.25 MW or 1.5 MW. It is found that despite these constraints, one beam is sufficient to access $\beta_N > 3$; and for nine of the eleven scaling relations, it should be possible to explore even the optimal high beta stability limit $\beta_N = 5$. As will be shown in Table 4.6, it will be possible to achieve $\beta_N = 3$ without NBI.

Table 4.5. Optimized plasma parameters to achieve $\beta_N \approx 5.0$.

Scaling Relation	R (m)	A	I_p (MA)	B_{T0} (T)	$\langle n_{e20} \rangle$ (m^{-3})	τ_E (ms)	β_N	$\langle \beta \rangle$ (%)	P_{NB} (MW)	P_{tot} (MW)
Neo-Alc	0.60	1.60	0.7	0.3	1.01	15.3	3.65	22.7	1.5	2.65
Kaye-all	0.75	1.39	1	0.3	0.70	55.8	5.08	31.4	1.25	1.96
Lack-Gott	0.64	1.49	1	0.3	1.10	45.6	5.13	39.8	1.25	2.19
RLW	0.76	1.38	1	0.3	0.66	89.8	5.21	31.3	1.25	1.74
Gold-quad	0.60	1.60	0.7	0.3	1.01	16.3	3.80	23.6	1.5	2.59
Gold-L	0.64	1.49	1	0.3	1.10	41.9	5.09	39.5	1.25	2.25
Kaye-Gold	0.75	1.39	1	0.35	0.70	72.4	5.21	27.6	1.25	1.80
DIII-JET	0.71	1.42	0.7	0.3	0.57	25.1	5.02	23.4	1.5	2.10
ITER89-P	0.60	1.54	0.7	0.3	0.93	25.9	5.08	30.4	1.25	1.98
DTEM	0.70	1.43	1	0.3	0.85	45.0	5.00	34.0	1.25	2.12
DIII-D-OH	0.77	1.38	1	0.4	0.65	125.0	5.44	24.4	1.25	1.59

Beta-limit scaling with aspect ratio – beam-heated cases

To ascertain that the β -limit can be studied over a range of aspect ratios, we have determined the neutral-beam and total power required to reach $\beta_N = 5$ for A between 1.25 and 2.0, assuming Lackner-Gottardi scaling (which has been compared favorably to START experimental results). The following parameters were chosen to allow this range of A while maintaining $q > 3.2$: $R_0 = 0.60$ m, $\kappa = 2.0$, $\bar{n}_e = 0.8 I_p / (\pi a^2)$, $I_p = 0.8$ MA, and $B_{T0} = 0.3$ T (but increased gradually to 0.63 T as required to keep $q > 3.2$). As Fig. 4.7 shows, $P_{NB} \leq 2.4$ MW (or 1.1 MW if q replaces q_{cyl} in the scaling relation) is required over the entire range of A . The power required using q_{cyl} drops as A is increased from 1.25 because β_N increases linearly with a^{-1} which is proportional to A given a fixed R_0 . When the q -limit is reached, however, B_{T0} must be increased, and the resulting decrease in

β_N dominates. The conclusions are that one beam is adequate to reach the β limit for all but two scaling relations (which may require two beams if these relations are found to apply), and that for Lackner-Gottardi, two beams are adequate for $1.25 \leq A \leq 2.0$ with q_{cyl} dependence and one beam is adequate assuming q dependence. One beam is adequate to reach $\beta_N = 3$ with either assumption. Again, many of the scaling relations predict achievable high β even in the Ohmic phase.

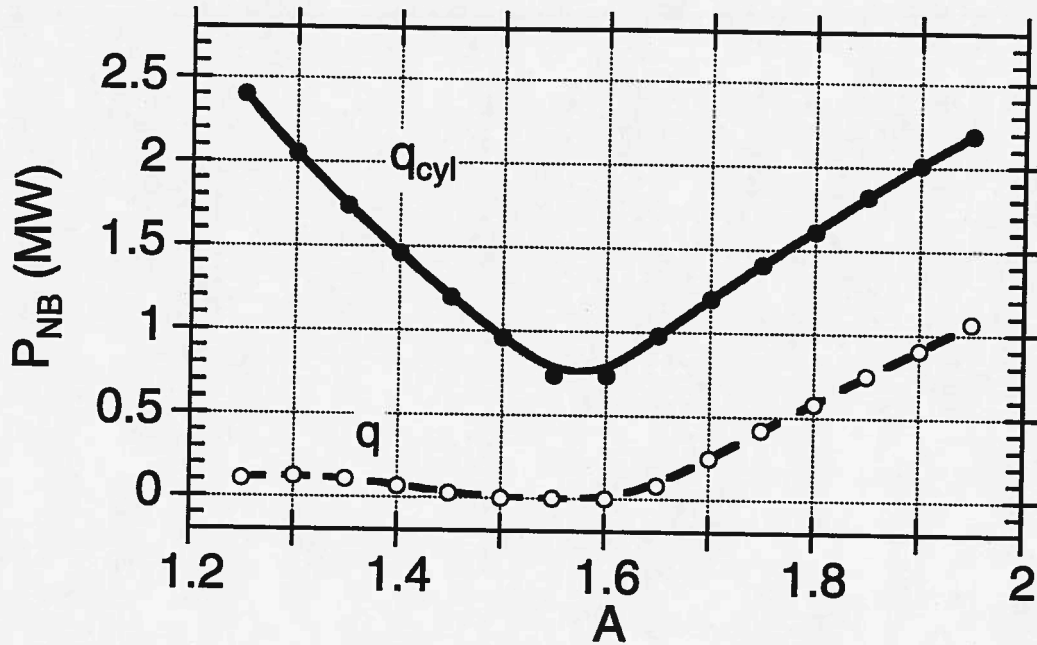


FIG. 4.7. Neutral-beam power P_{NB} required as a function of aspect ratio to reach a normalized beta value $\beta_N = 5$ assuming Lackner-Gottardi confinement scaling with either q_{cyl} or q used in the scaling relation.

Average-beta optimization

We next investigate optimizing plasma parameters to maximize volume-average beta $\langle\beta\rangle$ as opposed to β_N . In general, to maximize $\langle\beta\rangle$ for a given heating power, the major radius is decreased to minimize plasma volume. Then the aspect ratio is minimized, constrained by the inner vessel wall, to allow the greatest I_p before the q limit is reached. Note that Ohmic heating is the most efficient way to increase $\langle\beta\rangle$ since an increase in I_p allows higher plasma densities to be achieved. Once the q limit is reached, neutral-beam power, if available, can be added until the β_N stability limit is reached.

In Table 4.6 shown below, we have restricted ourselves to $R_0 = 0.64$ m, $A = 1.49$, $\kappa = 2.0$, $I_p = 1.05$ MA (to keep $q > 3.2$), $B_{T0} = 0.3$ T, one neutral beam, and $\beta_N < 5$ for stability (assuming an optimized current profile). These studies indicate that with Ohmic heating alone, USTX should be able to achieve $\langle\beta\rangle = 20 - 40\%$ for any of the eleven scaling relations studied, and $\langle\beta\rangle > 25\%$ with $P_{NB} \leq 1.5$ MW. Note that stability considerations are likely to limit $\langle\beta\rangle$ further, but the point here is that excessive beam power is not required with careful optimization. Since we used the same I_p , a , and B_{T0} in each case, for $\beta_N = 5$ all of the scaling relations would reach the same value, $\langle\beta\rangle = \beta_N I_p (\text{MA}) / (a(\text{m}) B_{T0} (\text{T})) = 40.8\%$. For neo-Alcator, Goldston-quadrature, and DIII-D-JET, however, we are unable to reach $\beta_N = 5$ with $P_{NB} \leq 1.5$ MW, for the conditions specified. For RLW and Kaye-Goldston which can reach $\beta_N = 5$ with ohmic heating alone, it is necessary to reduce the density to avoid exceeding the $\beta_N = 5$ limit with the conditions specified.

Table 4.6. Achievable volume-averaged beta with $R_0 = 0.64$ m, $A = 1.49$, $I_p = 1.05$ MA, $B_{T0} = 0.3$ T, and $P_{NB} \leq 1.5$ MW.

Scaling relation	$\langle n_{e20} \rangle$ (10^{20}m^{-3})	τ_E (ms)	P_{NB} (MW)	β_N	$\langle\beta\rangle$ (%)	$\langle\beta\rangle$ $P_{NB}=0$
Neo-Alc	1.16	18.6	1.50	3.22	26.3	20.6
Kaye-all	1.16	56.2	0.74	4.99	40.8	34.9
Lack-Gott	1.16	54.1	0.81	4.99	40.8	35.3
RLW	0.97	124.1	0.00	4.99	40.8	40.8
Gold-quad	1.16	22.6	1.50	3.59	29.4	22.8
Gold-L	1.16	45.0	1.18	4.99	40.8	32.8
Kaye-Gold	0.94	129.6	0.00	4.99	40.8	40.8
DIII-JET	1.16	27.9	1.50	4.05	33.1	26.3
ITER89-P	1.16	39.0	1.50	4.98	40.7	31.5
DTEM	1.16	43.8	1.23	4.99	40.8	33.2
DIII-OH	1.16	62.7	0.56	4.99	40.8	34.0

We conclude that if any of these empirical scaling relations are valid at low A , and current profiles are found to be favorable (or can be adjusted) for MHD stability, this device should achieve a volume-averaged beta in the range of 20 – 40%.

References for Chapter 4

- [1] G. G. Castle, *Dimensionless parameters, scaling laws, and the implications for ETG*, Report FRCR # 462, The University of Texas (1995).
- [2] R. J. Colchin, P. G. Carolan, R. Duck, *et al.*, Phys. Fluids B **5** (1993) 2481.
- [3] A. Sykes, J. W. Connor, R. Duck, *et al.*, Plasma Phys. Controlled Fusion **35** (1993) 1051.
- [4] G. D. Garstka, J. Basken, J. R. Danielson, *et al.*, Bull. Am. Phys. Soc. **39** (1994) 1574.
- [5] Y. Ono, A. Morita, M. Katsurai, *et al.*, Phys. Fluids B **5** (1993) 3691.
- [6] M. Ono, C. B. Forest, Y. S. Hwang, *et al.*, in *Plasma Physics and Controlled Nuclear Fusion Research 1992*, (International Atomic Energy Agency, Vienna, 1993), Vol. 1, p. 693.
- [7] B. A. Nelson, T. R. Jarboe, D. J. Orvis, *et al.*, Phys. Rev. Lett. **72** (1994) 3666.
- [8] M. Irie, H. Kusama, N. Saitou, *et al.*, in *Proceedings of the 17th European Phys. Soc. Conf.*, Amsterdam, (1990), Vol. 14B, Part II, p. 626.
- [9] F. Troyon, R. Gruber, H. Saurenmann, *et al.*, Plasma Phys. Controlled Fusion **26** (1984) 209.
- [10] S. G. Kalmykov, Plasma Phys. Reports **20** (1994) 939. See discussion in Sec. 3.2.
- [11] R. J. Goldston, Plasma Phys. Controlled Fusion **26** (1984) 87.
- [12] M. Greenwald, J. L. Terry, S. M. Wolfe, *et al.*, Nucl. Fusion **28** (1988) 2199.
- [13] K. Borass and NET Team, Nucl. Fusion **31** (1991) 1035.
- [14] D. E. Post, in *ITER Physics IAEA/ITER/DS/21* (ITER Doc Series), (IAEA, Vienna, 1991).
- [15] G. H. Neilson, E. A. Lazarus, M. Murakami, *et al.*, Nucl. Fusion **23** (1983) 285.
- [16] S. C. McCool, A. J. Wootton, R. V. Bravenec, *et al.*, *Optimization of a Megampere Spherical Tokamak for Beta-Limit and Confinement Studies*, Report FRCR 464, The University of Texas (1994).
- [17] W. M. Nevins, personal communication (1994).
- [18] D. W. Ross and J. C. Wiley, Bull. Am. Phys. Soc. **40** (1995).
- [19] G. M. Staebler, F. L. Hinton, J. C. Wiley, *et al.*, Phys. Plasmas **1** (1994) 909.
- [20] S. Fairfax, A. Gondhalekar, R. Granetz, *et al.*, in *Plasma Physics and Controlled Nuclear Fusion Research 1980*, (International Atomic Energy Agency, Vienna, 1981), Vol. 1, p. 439.
- [21] K. Lackner and N. A. O. Gottardi, Nucl. Fusion **30** (1990) 767.
- [22] P. H. Rebut, P. P. Lallia, and M. L. Watkins, in *Plasma Physics and Controlled Nuclear Fusion Research, 1988*, (International Atomic Energy Agency, Vienna, 1989), Vol. 2, p. 191.
- [23] P.-H. Rebut, M. L. Watkins, D. J. Gambier, *et al.*, Phys. Fluids B **3** (1991) 2209.

- [24] S. M. Kaye and R. J. Goldston, *Nuclear Fusion* **25** (1985) 65.
- [25] S. M. Kaye, *Phys. Fluids* **28** (1985) 2327.
- [26] S. M. Kaye, C. W. Barnes, M. G. Bell, *et al.*, *Phys. Fluids B* **2** (1990) 2926.
- [27] P. N. Yushmanov, T. Takizuka, K. S. Riedel, *et al.*, *Nucl. Fusion* **30** (1990) 1999.
- [28] T. H. Osborne, N. H. Brooks, K. H. Burrell, *et al.*, *Nucl. Fusion* **30** (1990) 2023.
- [29] W. M. Nevins, *D3-JET Scaling*, Report TPX DOC #93-930512-PPPL/G.Neilson-01, Princeton Plasma Physics Laboratory (1993).
- [30] F. W. Perkins, in *Proceedings of the 4th International Symposium on Heating in Toroidal Plasmas*, edited by H. Knoepfel and E. Sindoni, Roma, (CEC, Brussels, 1984), Vol. II, p. 977.
- [31] F. W. Perkins and y. C. Sun, *On Confinement Scaling and Ignition in Tokamaks*, Report PPPL-2261, Princeton Plasma Physics Laboratory (1985).
- [32] N. A. Uckan, *Fusion Tech.* **15** (1989) 391.
- [33] J. Tsai, personal communication (1995).
- [34] S. M. Kaye, personal communication (1995).
- [35] Y.-K. M. Peng and D. J. Strickler, *Nucl. Fusion* **26** (1986) 769.
- [36] N. A. Uckan, *ITER -Physics Design Guidelines*, Report ITER Document Series No. 10, IAEA, Vienna (1990).
- [37] W. H. Miner, Jr., *A Tutorial describing Access to the MFE Data Base*, Report FRCR #378, The University of Texas (1990).
- [38] V. S. Chan, M. S. Chu, C. B. Forest, *et al.*, in *Proceedings of the Small Aspect Ratio Tokamaks Workshop*, Oak Ridge, TN, (1994).

CHAPTER 5

PHYSICS DESIGN CONSIDERATIONS: MAGNETICS

We now discuss the physics studies necessary for design of the OH solenoid and poloidal and toroidal field coils. Poloidal field* (PF) coils are necessary to drive plasma current, maintain plasma equilibrium, and to select and actively control plasma position and shape. We show that the present conceptual design of USTX can produce the desired point design plasmas, and that sufficient flexibility in the PF coil system allows exploring a large operating space. Effects of toroidal field coils on plasma and tokamak design are discussed. Some preliminary studies of plasma MHD stability are also presented here.

Non-inductive current drive is one of the major challenges left to the fusion program, and it is claimed to be a necessary condition for the realization of a fusion reactor. But it is still difficult to predict, in part since it depends on the confinement properties of the plasma, which are unknown at low A . That being the case, the design of the USTX PF coil system provides the means for purely inductive current drive to the desired plasma current value of 1 MA.

Because it drives the whole design of the poloidal field coil system, a discussion of the ohmic (OH) solenoid design is presented first. Next follows a discussion of different aspects of the poloidal field system study, as they would arise in the temporal evolution of a discharge: breakdown, current ramp up, and flat top. A preliminary discussion of shape flexibility, position control and disruption effects follows. Simulations of plasma evolution, as driven by available power supplies, are presented. Toroidal field coil considerations such as ripple and eddy currents are discussed with simple models. Finally, preliminary MHD stability studies are discussed.

Time dependent simulations of the evolution of plasma and poloidal fields, taking into account induced eddy currents, transport and MHD stability, will eventually describe the operating space accessible to USTX. Here we present only initial studies showing some of the capabilities of the present concept.

* Anywhere in this chapter, magnetic fields that are not toroidal are described generally as poloidal, whether they are vertical, horizontal, or genuinely poloidal.

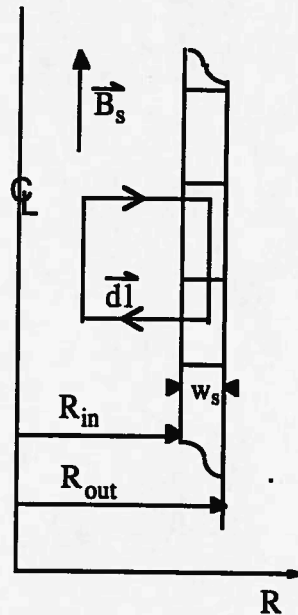
5.1 OH solenoid design strategy

The solenoid design depends on a variety of constraints: geometric, mechanical, electrical, thermal. Here we describe the simplest models that are used to specify the desired solenoid. They provide enough information to choose an optimum design, which is then studied in detail to guarantee its performance.

Geometry

The design attempts to maximize flux swing. The space available to the solenoid is constrained by the central toroidal-field (TF) core and the operational aspect ratio and major radius. Within this space the flux attainable depends on the current density in the solenoid. The current density is limited either by the mechanical strength of the copper, or by a maximum allowable temperature excursion. The details of the solenoid layout (number of layers, number of turns, winding pitch) depend on mechanical and electrical prescriptions.

The simplest possible model to estimate solenoid performance is given by an infinitely long solenoid of radius r_{oh} , thickness w_s , n_s turns per unit length and a one-turn current I_s , as shown in Fig. 5.1.



$$\oint \vec{B} \cdot d\vec{l} = \mu_0 \int \vec{j} \cdot d\vec{S}$$

$$B_s = \mu_0 n_s I_s$$

$$\Delta \Psi_s(R) = 2 \int_0^R \vec{B} \cdot d\vec{S}$$

$$n_s = \text{turns / length}$$

$$I_s = \text{current / turn}$$

$$w_s = (R_{\text{out}} - R_{\text{in}})$$

$$r_{oh} = (R_{\text{out}} + R_{\text{in}}) / 2$$

FIG. 5.1. Schematic of flux calculation in an infinite solenoid.

Assuming that the solenoid current density, J_s , is uniform, the total change in flux when the current changes from I_s to $-I_s$ is given by

$$\Delta\Psi_s = 2\pi\bar{r}_s^2(\mu_0 I_s n_s) = 2\pi\bar{r}_s^2\mu_0 J_s w_s, \text{ with } \bar{r}_s = \sqrt{r_{oh}^2 + w_s^2 / 12}, \quad (5.1)$$

Hence, the solenoid radial extent and the allowed poloidal current density determine the maximum available flux swing.

The solenoid inner radius, R_{in} , is defined by the toroidal field (TF) inner core. The radial extent of the TF core is determined by thermal considerations. Given desired values of B_T at R_0 (which gives the current in the TF coils I_{TF}), the equivalent square pulse duration Δt , and the allowed temperature rise in the TF core ΔT , then the outer radius of the TF core $R_{TF,out}$ is uniquely defined by the allowed current density

$$\pi(R_{TF,out} - R_{TF,in})^2 = I_{TF} \sqrt{\frac{\eta}{\rho C_T} \frac{\Delta t}{\Delta T}}. \quad (5.2)$$

Here η , ρ and C_T are the resistivity, mass density and thermal capacity of the copper, respectively. $R_{TF,in}$ cannot vanish, since a central spindle is included for structural integrity. Allowances need to be made for insulation, cooling lines, and TF-solenoid clearance, which are taken into account in the detailed design, and ultimately determine the inner radius of the solenoid.

The inner radius of the plasma $R_{p,in}$ is defined by the choice of aspect ratio and plasma size;

$$R_{p,in} = R_0 (A-1)/A. \quad (5.3)$$

A radial gap is required between the OH solenoid outer radius and $R_{p,in}$ to allow space for the inner vessel wall, diagnostics, and protective carbon tiles. The OH solenoid radial extent is thus fully specified.

In the above discussion, and in what follows, only the infinite solenoid model is used. The height of the solenoid is effectively determined by the largest expected plasma height, since stray end fields would otherwise deform the plasma boundary. Actual simulation results for realistic solenoid designs are presented in Chapter 6. In most cases the only correction necessary to the infinite-solenoid calculations is the computation of mutual inductances. Note that much of the early work on USTX solenoid optimization was

done in collaboration with the ORNL group, including Richard Colchin, John Galambos, Paul Goranson, and Steve Hirshman.

Materials

The solenoid current density is limited by the mechanical and thermal characteristics of its constituent parts (copper and insulation). The hoop force on each turn is balanced by the tensile strength of copper. In the infinite solenoid approximation, the stress limit $\sigma(R)$ is given by

$$\sigma = F/S = J_s B_s R < \sigma_{Cu}. \quad (5.4)$$

The hoop force is largest at the inner radius of the solenoid. Often a limiting value of the solenoid field B_s (typically 10 T) is quoted as the mechanical constraint, rather than the actual stress. The yield strength of the chosen material defines an upper bound for J_s (taking into account safety margins). Maximizing flux swing is best done by selecting stronger types of copper and high J_s .

Ohmic heating of the solenoid is another limiting factor on J_s , defined by material choice. The solenoid temperature rise at the end of the pulse is given by

$$\Delta T = J_s^2 \frac{\eta}{\rho C_T} \Delta t, \quad (5.5)$$

with all quantities defined as for equations (5.1-2). Active water cooling of the solenoid is required between shots to limit temperature excursions to a reasonable value. The water-cooling system performance defines the time between shots as well.

Any given solenoid design is either stress or thermally limited. The interplay between the two limits guides the choice of material: a stress limited solenoid calls for a stronger copper, even though it may be more resistive.

More detailed calculations of mechanical and thermal stresses, including von Mises forces, are discussed in Chapter 6.

Winding schemes

Ease of winding and fabrication, cooling, and turn-to-turn voltages are taken into consideration to select the "internal" details of the solenoid: how many turns, how they are

distributed radially and vertically (number of radial layers and number of turns/layer), pitch of the coils (n-in-hand). As the number of turns is increased, more space is lost to insulation, and less current per turn is required, but the length of the cooling paths increase. It is generally advantageous to have low current per turn, so error fields associated with feeds are reduced. The more radial instead of vertical layers, the easier it is to wind the coils (to avoid keystoneing). Winding many-in-hand reduces cooling path lengths.

The finite helical pitch of the solenoid coils may produce error fields that would contribute to the formation of islands in the plasma and/or reduce plasma confinement. This problem was investigated by the Auburn University group using a field-line tracing code [1]. Different solenoid designs were studied. It was found that, if there is an even number of radial layers, and they are wound with alternating helicity, there is good cancellation of the stray fields. The largest expected island size is 0.5 cm or less, which is acceptably small.

A large voltage V_S must be applied across the solenoid in order to initiate plasma breakdown with a plasma loop voltage V_{BD} .

$$V_S = (L_S / M_{SP}) V_{BD}, \quad (5.6)$$

where L_S is the solenoid self-inductance, while M_{SP} is the mutual inductance between the solenoid and a filament at the plasma position. To keep V_S low (so less space for insulation is required), it is best to have fewer turns at higher current I_S .

Cost

Cost is also an issue. For instance, a maximum-stress design would have more turns in the outer radial layers (where the most flux gain is attained) than in the inner ones (where the stress is highest). But the increase in flux swing may not be worth the higher fabrication cost and resistive power consumption.

Flux consumption

The available flux swing is consumed by raising the plasma current inductively and by resistive dissipation. During the plasma ramp-up phase, the latter term is most simply modeled as a fraction of the internal inductive term, with the Ejima coefficient C_{Ejima} [2], as follows:

$$\Delta\Psi = L_p I_p + \int_0^{t_p} \mathcal{R}_p I_p dt = \mu_0 R_0 I_p \left[\ln \frac{8R_0}{a\sqrt{k}} + \frac{l_i}{2} (1 + C_{\text{Ejima}}) - 2 \right] \quad (5.7)$$

with L_p being the plasma inductance, \mathcal{R}_p the resistance, l_i the normalized plasma internal inductance, and the other parameters as defined in Table 1.1. In the detailed design the plasma external inductance is not given as in the above equation, but as described by Hirshman and Neilson [3] taking into account low-aspect-ratio corrections. Time dependent simulations that more accurately reflect flux consumption will be described in Section 5.7, and are used to fine-tune the OH solenoid design..

5.2 Breakdown fields

The use of a double-swing solenoid implies that at breakdown time, the solenoid current has a large positive value (the plasma current direction is defined as positive). Such an arrangement produces a large vertical field at the plasma position, which is in the direction that would force the plasma towards the solenoid during the first half of the swing. Such stray fields need to be compensated by return coils to form a field null for breakdown and to facilitate control of plasma shape by the other PF coils.

The fields at breakdown time are produced by the solenoid, the PF coils and eddy currents induced on passive structures by the current ramps in the PF coils and solenoid. Optimum solutions are dependent on details of eddy current models, but basic features are somewhat model independent. A study by Hwang and Ono [4] shows that a sufficiently good field null, as shown in Fig. 5.2, can be achieved with existing coils.

The voltage available for plasma breakdown is very sensitive to the solenoid design and power supply (P/S) circuit details. Two different circuits were modeled to simulate the OH P/S. In the first case the P/S voltage was reversed at full forward current to supply the breakdown voltage. The voltage available for plasma breakdown is presently estimated at 4 to 5 Volts with this circuit. In a second option, a series resistance is included in the solenoid circuit in order to drive the current down more rapidly. The available breakdown loop voltage in that case is of order 15V. The voltage appearing at the plasma is reduced by eddy currents in the TF core (as discussed in section 5.7) and in the vacuum vessel. The TF eddy currents reduce the effective breakdown voltages by 10%. Conservatively we then expect 3 V ($E_T \sim 1$ V/m) with P/S reversal and 12 V ($E_T \sim 4$ V/m) with a series resistance.

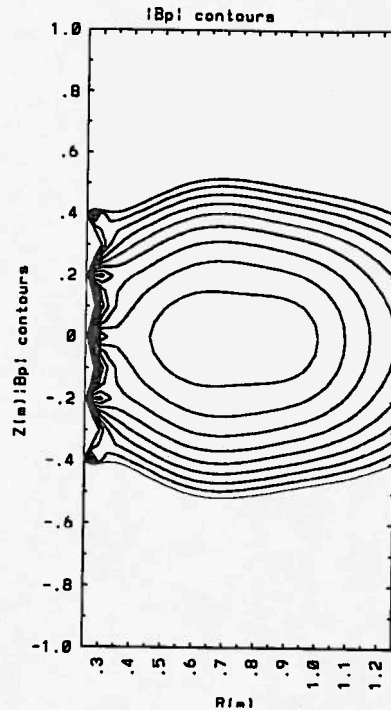


FIG. 5.2. Contours of $|B_p|$ showing that a good null can be formed for plasma breakdown. The innermost contour corresponds to 5 G, subsequent ones are spaced at intervals of 5 G, increasing outwards.

Allowable poloidal error fields for ohmic breakdown, B_\perp , are related to the toroidal electric field E [5, 6] by

$$B_\perp(\text{T}) \leq 10^{-3} E_T(\text{V/m}) B_T(\text{T}).$$

This limits the transverse field to 5 Gauss or less (over most of the plasma cross section) for the P/S reversal circuit, and to 20 Gauss for the series resistor circuit. The poloidal field null achievable with the present set of coils is only that small in the central part of the plasma, as was shown in Fig. 5.2. As a consequence, the use of ECH to initiate breakdown may be required. DIII-D [5] results indicate that ECH allows low voltage breakdown in the presence of error fields larger than 50 G. ECH startup assist scenarios are described in 7.3.

5.3 Plasma current ramp rate

Studies of the current-rise phase of tokamak discharges are inconclusive as to which processes are responsible for initial current penetration: MHD in general, double tearing modes in particular, classical, neoclassical or anomalous resistivity, etc. Results from TEXT [7] and JET [8, 9] indicate anomalous resistivity during the initial current ramp-up phase but Spitzer/neoclassical resistivity for a plasma current ramp later in the discharge [10, 11]. In TFTR [11] current ramps as fast as 5 MA/s are used, up to 1 MA plasma current.

Ramp rates of 1-2 MA/s on DIII-D are routinely used [6]. On TEXT-U, ramp rates of 6 MA/s are easily attained up to 0.2 MA, without exciting large MHD activity. Details of tokamak operation (whether the toroidal field is ramped together with the plasma current, pre-programming of plasma position and shape, gas-puff rates, wall conditioning) allow some latitude in the current ramp rate choice. Different operational scenarios will be investigated numerically and experimentally. For the time being, it has been assumed that the plasma current ramp-up rate in USTX is 5 MA/s, based on TEXT operational experience and on indications from larger tokamaks. This can be considered as an upper bound, since it can always be reduced on demand.

Possible enhanced neoclassical resistance due to the increased number of trapped particles at low A may allow faster current ramp rates, by reducing skin times and automatically producing more peaked current profiles. On the other hand, hollow current density profiles may be stable in low-aspect-ratio tokamaks, allowing low-inductance plasmas during the current ramp and the flat top. This reduces initial volt-second consumption. Indication of such behavior has been observed in START [12] where a current ramp rate of 50 MA/s has been achieved ($V_{loop} = 3-4$ V, $I_p < 160$ kA). The fast ramp rate is thought to be due to the small internal and external inductances of this low- A device. Our own time-dependent simulation codes indicate that plasma current ramp-up rates of order 5 MA/s can be expected in USTX, as will be discussed in section 5.7.

At plasma initiation time, there are large time derivatives of the current in all PF coils. Poloidal field coils in spherical tokamaks have rather strong coupling, particularly to the solenoid. This imposes the most stringent constraints on the voltages of the PF system power supplies. For the point design, a satisfactory assignment of existing supplies can be made, which will be discussed in Chapter 6.

5.4 Plasma shape control

As usual, flexibility and optimization produce orthogonal requirements for poloidal field coil placement, as well as vacuum vessel design. For detailed plasma shape control it is desirable to have the plasma completely surrounded by actively controlled poloidal field coils. One objective of USTX is to study many different configurations, with different plasma sizes and aspect ratios, as described in Chapter 4. Adequate space must be provided inside the vessel for such flexibility, and the poloidal field coils need to be farther from the plasma, becoming less efficient at controlling details of the plasma shape. We show in this section that the USTX design has sufficient PF coils to overcome this problem.

A solenoid of infinite length would provide the flux swing without affecting the plasma shape. A finite solenoid with return windings provides the best realizable approximation to inductive drive with minimum effect on plasma shape. In this section we show that shape control during the plasma flat top phase is possible (see Figs. 5.3-4). Shape flexibility will be explored further. For instance, a highly triangular plasma is described in Sec. 5.8.

A description of a PF coil configuration found to give good equilibrium shape control is shown in Table 5.1 for reference, where ΔR and ΔZ are the conductor full width and height. This set of coils has been used for all equilibrium calculations presented.

Table 5.1. Description of poloidal field coils.

PF#	R(m)	Z(m)	ΔR (m)	ΔZ (m)
PF1a	0.250	± 1.550	0.025	0.090
PF1b	0.250	± 1.480	0.050	0.060
PF2	0.530	± 1.475	0.075	0.130
PF3	1.020	± 1.365	0.075	0.130
PF4	1.600	± 1.200	0.100	0.100
PF5	1.770	± 0.550	0.200	0.100

To illustrate the performance of the PF coil system, a relatively high- β plasma is time-stepped through the current flat-top, while the shape of the last closed flux surface is held constant. Figures 5.3 and 5.4 show the plasma at the beginning and end of the flat-top, indicating that the plasma shape is well controlled by the PF coils. Note that R_{axis} is the major radius of the magnetic axis, J_t is the toroidal current density, and $\langle \dots \rangle$ indicates a flux-surface average. The equilibria are computed with EFIT [13]. The pressure and current-density profiles chosen in this case are conventional (i.e., peaked in Ψ). Note that even though the shape of the last closed flux surface (LCFS) is relatively well conserved, the shape of the scrape-off layer (SOL) changes, due to solenoid stray fields. Different prescriptions in the equilibrium code need to be implemented to allow for requesting not only a given LCFS shape, but also a given SOL shape. Further equilibrium studies will elucidate the degree of control of plasma and SOL shape permitted by the PF system. Of course, non-inductive current drive would alleviate shape control problems, by reducing solenoid stray fields.

As is discussed in Chapter 6, a combination of existing power supplies, P/S, (from TEXT-U) and a new OH solenoid supply are used for the PF system. The current ramp-up and flat-top phases were studied to ensure that the available P/S voltages and currents could control plasma shape and position throughout the discharge. In this particular example the plasma minor radius was increased slowly, from an initial value of 0.26 m, and the safety factor was held approximately constant from $I_p = 250$ kA to 1 MA. The largest PF coil voltages are required during the first few time steps. The present P/S should be adequate to control the plasma. Different prescriptions for the ramp-up phase (varying the plasma major radius or the toroidal field during the ramp) may further alleviate P/S voltage requirements. Additional exploration of the operating space of USTX is required before the design of the PF windings and their power supplies can be finalized.

Other shapes are shown in the MHD discussion in Sec. 5.8. For instance, a low-aspect-ratio plasma ($A = 1.25$), computed with the equilibrium code FBEQ, by Strickler, Peng and Galambos of ORNL [14] is shown later in Fig. 5.8, and a reversed shear configuration computed in collaboration with Lao is shown in Fig. 5.10. Note that the same PF coils are used for both the $A = 1.25$ and the $A = 1.43$ plasmas. The only difference between the two options is in the solenoid and the vacuum-vessel inner wall.

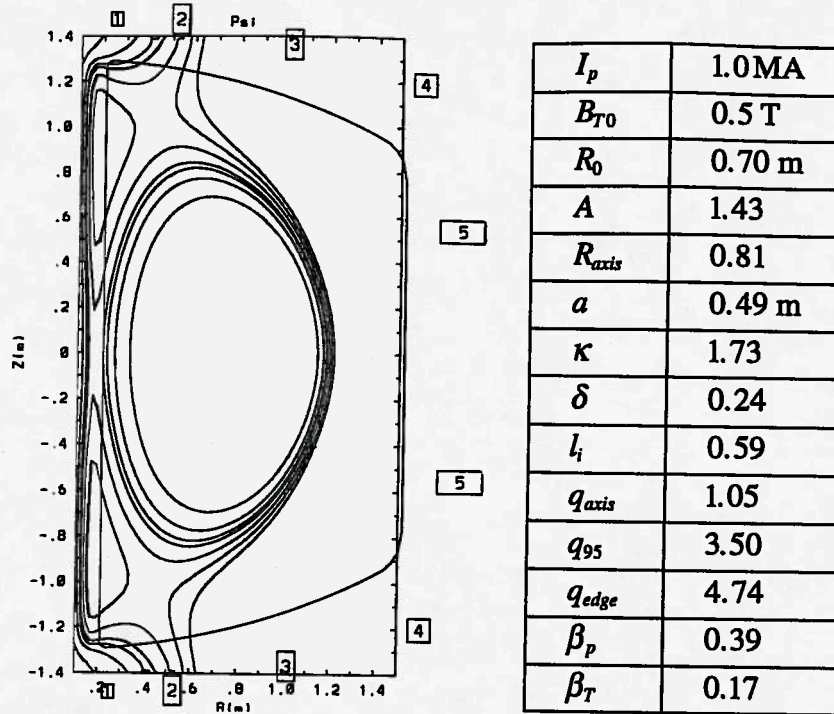


FIG. 5.3a. 1 MA plasma at the beginning of the flat top (solenoid current is -37 kA).

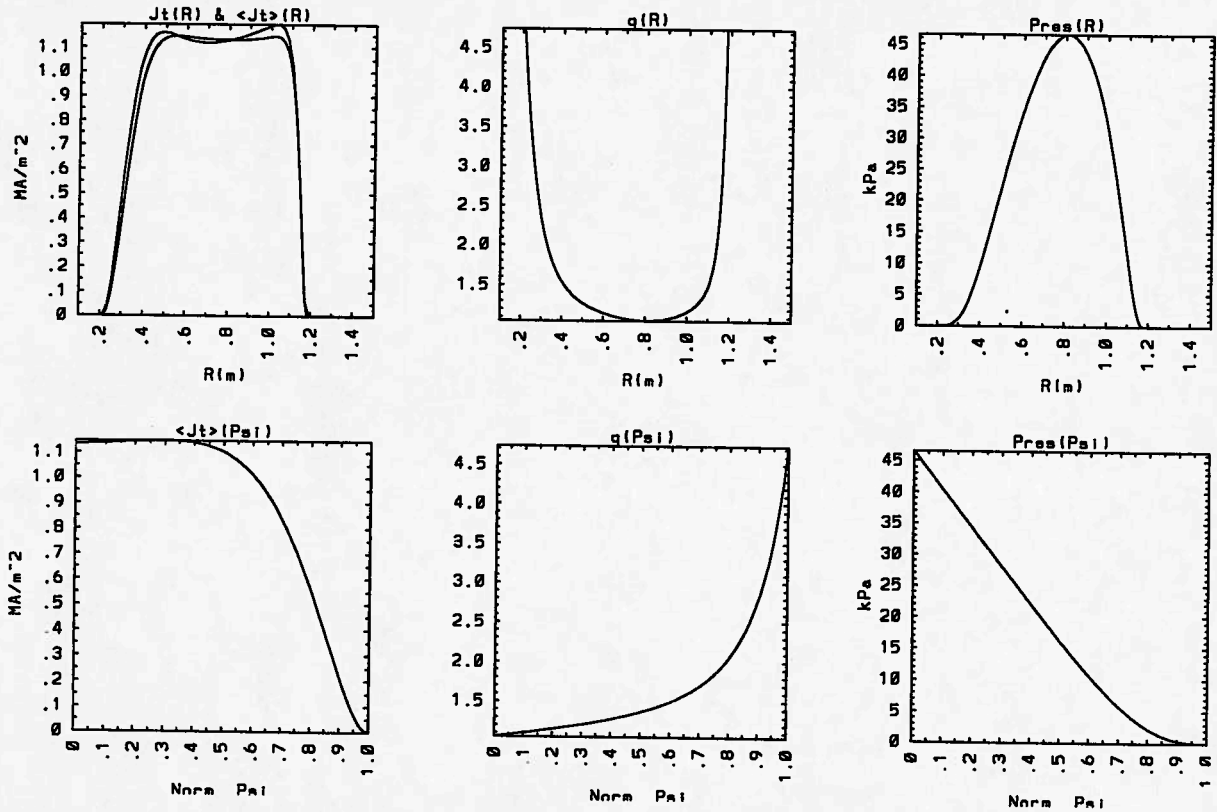


FIG. 5.3b. Profiles of toroidal current density J_T , safety factor q and pressure p , as a function of R at the equator, and as a function of normalized poloidal flux, corresponding to the equilibrium in 5.3a.

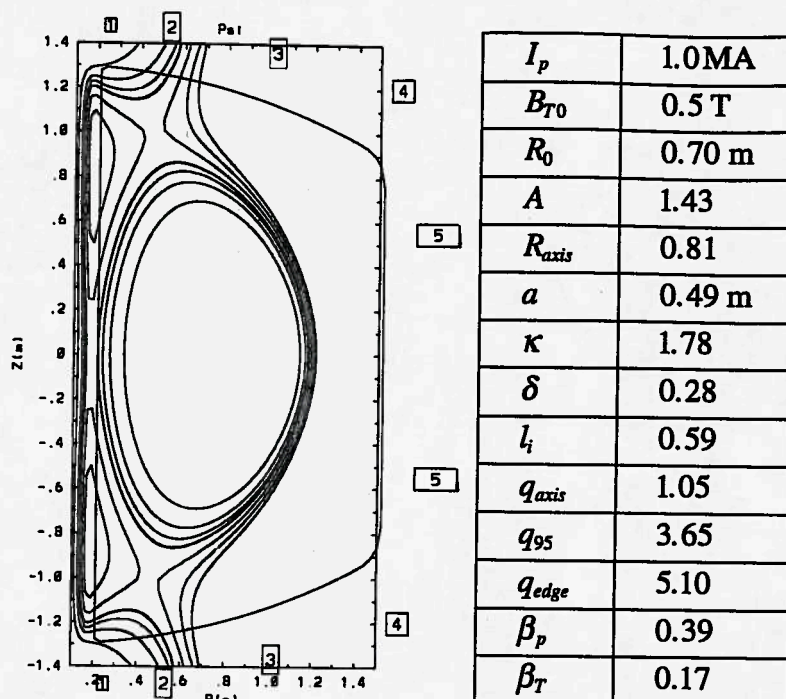


FIG. 5.4a. Plasma at the end of the flat top, when the solenoid current is -60 kA.

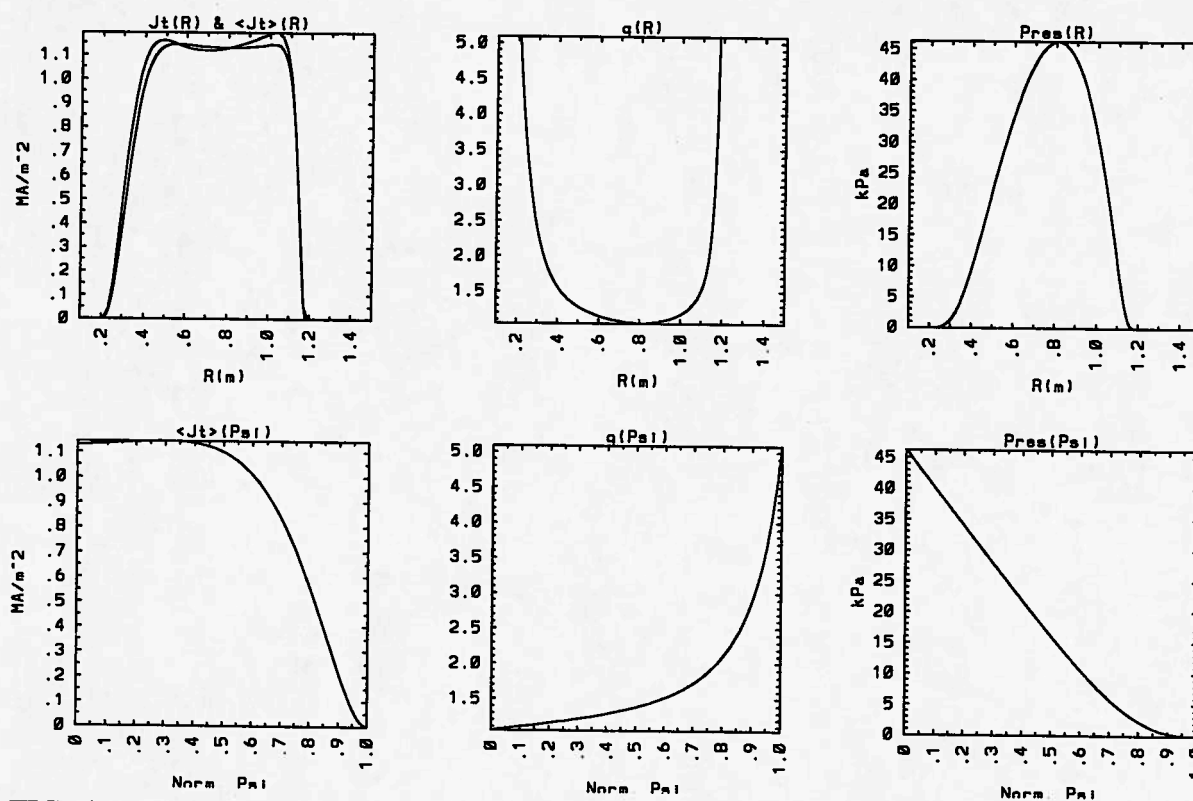


FIG. 5.4b. Profiles of toroidal current density J_T , safety factor q and pressure p , as a function of R at the equator, and as a function of normalized poloidal flux, corresponding to the equilibrium in 5.4a.

5.5 Plasma position control

Poloidal field coils have to provide real-time active control of the plasma position. Here we describe how we intend to study this problem. As mentioned in Chapter 3, in a homogeneous vertical field, elongated low- A plasmas can be stable to up-down displacements. Such natural position stability is reduced by stray fields from the solenoid and eddy currents (time dependent), up-down asymmetric plasmas, and elongation beyond the natural value. In-out plasma position stability also needs to be investigated in low- A tokamaks.

In general, models of the feedback problem have been developed for a simplified plasma, represented as a current filament. Plasmas with low internal inductance exhibit non-rigid behavior, and are generally more up-down unstable than similar plasmas with more peaked current profiles. Non-rigidity effects are usually only taken into account by arbitrarily imposing stronger constraints on the feedback system.

The plasma in-out position problem is connected to the plasma current control problem. A hybrid system is envisioned, in which PF4 and/or PF5 produce most of the vertical equilibrium field (preprogrammed + linear gain) and another coil, with a faster characteristic time (differential gain), is used for fast-feedback stabilization of the in-out position. The evidence from START [15] is that the in-out stability of elongated low l_i plasmas is quite good.

Selection of the active coil requires modeling of the vacuum-vessel eddy currents, which is underway. Eddy currents in passive structures can be decomposed into their normal modes [16]. This technique simplifies the study of the vessel-plasma interaction, since it allows the computation of lumped circuit characteristics (resistance, self and mutual inductances) of the relevant modes. The first symmetric mode is coupled to plasma current ramps and in-out displacements, while the first anti-symmetric mode is coupled to up-down displacements. The optimum active feedback coil is chosen by balancing two opposite criteria: the active coils must be well coupled to plasma displacements, but not to the eddy current distribution produced by such displacements [17].

Once the best coils are chosen, a closed-loop model of the feedback system will be implemented to determine power supply requirements imposed by the worst expected field indices. The possibility of adding fast-feedback coils for position control is still open; they will be added if it is found to be necessary during the design phase.

5.6 Fault conditions

START has disruption-free operation, at least as long as the plasma aspect ratio remains below 1.8 [18]. Reconnection events ultimately reduce the plasma current, but do not destroy the plasma. On the other hand, CDX-U does disrupt when q is low [19]. The electro-mechanical design needs to take possible disruption loads into account, since they may well happen in USTX.

At a 1 MA level, a plasma disruption can have dramatic consequences. Electrically, it induces transient voltages in the PF coils, requiring protection for both insulation and power supplies. Mechanically, induced currents in the vacuum vessel and plasma-facing components may produce large forces when crossed into the ambient poloidal and toroidal magnetic fields. There are two sources of disruption loads:

- a) As the plasma current decays the dI/dt induces toroidal currents in any toroidally continuous elements, including, in our case, the vacuum vessel. This toroidal current experiences a $\mathbf{J} \times \mathbf{B}$ force with any poloidal fields.
- b) Halo Currents: during a disruption the poloidal component of the current flows through the plasma facing components. These halo currents have been measured to be up to 35% of the plasma current (in DIII-D, for instance). The toroidal field induces a $\mathbf{J} \times \mathbf{B}$ force on these poloidal currents which can be considerable. The usual solution is to build a structure internal to the vessel which is not toroidally continuous but has current paths for these transient currents and which is reinforced to the main support structure. (Note that the design has to deal with potentially a 600 V loop voltage without breaking down). The vessel rib structure, external to the vessel and toroidally interrupted, provides current paths for the transient currents, while being stronger than the vessel itself. The forces are transmitted through a set of hard points to the external structure. All the plasma facing components, such as tiles, have to be able to resist these forces. It is believed that the tile breakage on Alcator C-Mod [20] was caused by tiles rotating under these forces, allowing adjacent tiles to supply a current path until the forces exceeded the structural strength.

These issues need to be assessed during the design phase in order to demonstrate the viability of this vessel concept.

5.7 Time dependent simulation

Issues like plasma breakdown, current ramp up, and even control of plasma shape during flat top are all time dependent. A variety of codes has been written to deal with different aspects of the problem. Here we describe the time-dependent codes that were used to aid in the solenoid characterization and design.

To study the plasma current ramp-up phase of the discharge, two codes were used in conjunction. The first one (the circuit code) describes the system of plasma, solenoid and return coils as a lumped circuit, and simulates the OH power supply capabilities. The second code (the plasma code) is a 1-D transport code that incorporates the relevant physics to study plasma evolution during the current ramp-up phase.

In the circuit code, the motor generator set and power supply are simulated as appropriately sized capacitors and series resistors. The OH system (solenoid & return windings) is characterized by its resistance, self-inductance and inductive coupling to the plasma. The mutual inductance between plasma and OH is calculated by assuming the plasma to be a current filament positioned at the nominal major radius, R_0 , without taking into account the plasma current distribution. Thermal heating and the consequent changes in solenoid resistance is included in the calculation. Two different options for the OH P/S were considered, the supply reversal and the resistor circuit. In the first case the P/S voltage was reversed at full forward current to supply the breakdown voltage. The available voltage is severely degraded by commutation lag caused by the series inductances, providing of order 5 V for plasma breakdown. In the second case a series resistance is included in the solenoid circuit in order to drive the current down more rapidly. For that case the available voltage is limited by breakdown limits in the solenoid winding and switching circuits and it is in excess of 15 V. Two plasma models are used in the circuit code. The simplest plasma model uses the Hirshman-Neilson prescription to compute the plasma external inductance, a prescribed value for l_i , and an Ejima coefficient to represent the plasma resistance. The plasma code described below provides an alternative plasma model for the circuit code, effectively describing the plasma as a time dependent current and voltage demand. The OH system is then forced by the circuit code to match that demand. In either case, the circuit equations are time-stepped from the initial conditions, ensuring all constraints (current and voltage limits, coil heating) are met. An example of the output of this code is shown in Fig. 5.5. Other examples are shown and discussed in Section 6.2

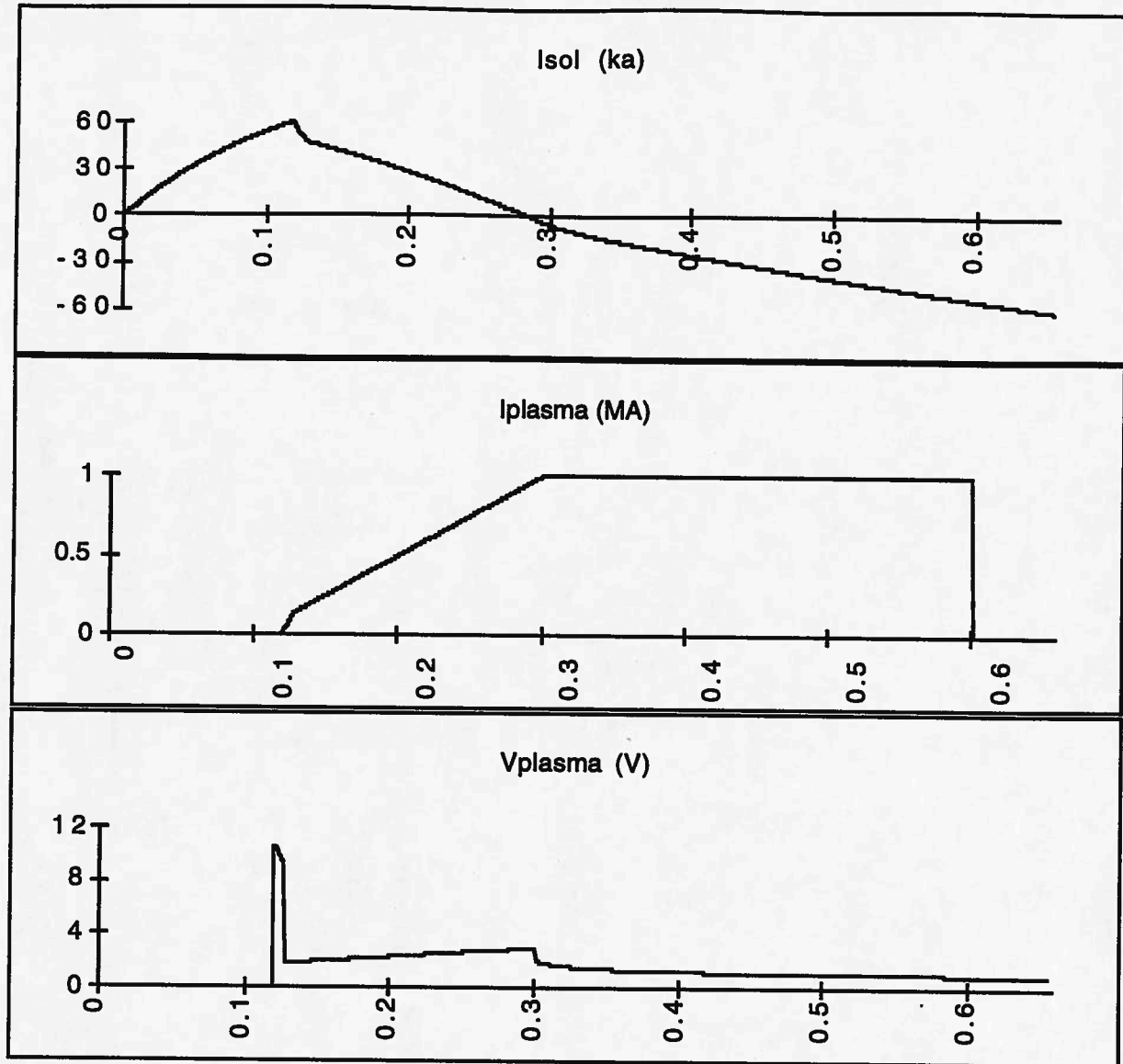


FIG. 5.5. OH current, plasma current and plasma loop voltage as functions of time. Lackner-Gottardi scaling was assumed in the plasma evolution.

The plasma code is a 1-D time dependent transport code. It is a development of a general transport code, designed in modular fashion to allow the study of different problems (for instance, an earlier version was used to study the L-H transitions in collaboration with GA [21]). The present version employs a low aspect ratio geometrical model (Section 3.1) modified to include triangularity [22]. At the moment, the density evolution is prescribed and the two coupled equations for electron energy and B_p (current penetration) are solved with a fixed T_i/T_e ratio. Besides geometric factors, the current penetration equation includes neoclassical resistivity with fixed Z_{eff} and Hirshman's

expression for the low aspect ratio bootstrap current [23] with collisional corrections. The fixed electron thermal transport coefficients are chosen numerically to reproduce a final steady-state solution based on scaling relations. (Neo-Alcator and Lackner-Gottardi were used as "pessimistic" and "optimistic" examples). The code does not include a plasma breakdown phase. The plasma is initialized with low values of distributed current density and temperature. For now, evolution of plasma geometry or transport coefficients has been ignored. Given a prescribed plasma current ramp function $I_p(t)$ and a choice of scaling law, the loop voltage required to match $I_p(t)$ is computed. The code follows the evolution of the current profile to a steady state condition. In the example shown in Fig. 5.5, a linear rise of I_p from 10 kA to 1 MA in 200 ms, followed by a flat top at 1 MA, was chosen. Many other quantities are computed as well, such as plasma resistance, internal and external plasma self-inductance, plasma beta, bootstrap fraction.

Detailed modeling of the system, including the M/G set and P/S circuit, using the EMTP power systems code, is in progress. This will better describe the hardware side of the problem, characterizing the capabilities of the device, and will be used for plasma position control studies in the future[24].

On the plasma side, more detailed simulation of plasma behavior (including anomalous current penetration, stability of profiles, non-inductive current drive, etc....) will also help characterize the expected performance. Collaboration with other institutions will allow us to use their available time-dependent codes to simulate detailed plasma and external circuit behavior. So far we have considered using TSC [25] from PPPL and TEQ [26] and CORSICA [27] from LLNL, and are continuing to develop our own codes.

5.8 Toroidal Field Coils

Ripple

Toroidal-field ripple is a potential source of error fields. The USTX design maintains the level of ripple at an acceptable value.

A simple model of TF ripple is developed by simulating the TF return legs as N vertical filaments located at R_{outer} . The local toroidal field is then be given by

$$B_T = \frac{B_{T0} R_0}{R} (1 + \delta \cos(N\phi)),$$

with

$$\delta(R) = \frac{B_{T\max} - B_{T\min}}{B_{T\max} + B_{T\min}} \approx \left(\frac{R}{R_{\text{outer}}} \right)^N.$$

The ripple δ at $R = 1.5$ m (the outermost possible plasma edge location) is shown in Fig. 5.6 as a function of R_{outer} for different numbers of turns N (all chosen even). The present design ($N = 12$, $R_{\text{outer}} = 2.6$ m) has a ripple $\delta < 0.1\%$, sufficiently small for any purposes. Halving N to 6 gives a ripple $\delta \approx 4\%$, which is still fairly small.

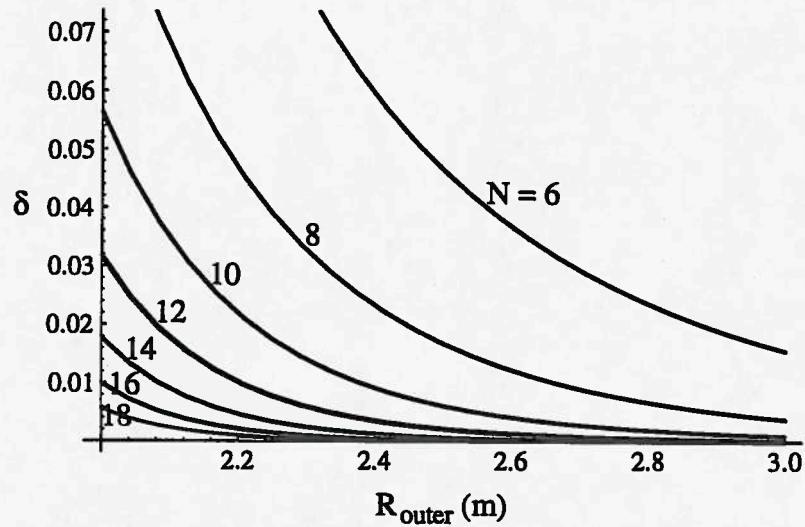


FIG. 5.6. The ripple δ at the outermost plasma edge ($R = 1.5$ m) as a function of the TF vertical return leg major radius R_{outer} , for different numbers of TF coils N .

Eddy currents

The time varying magnetic field in the OH coil generates eddy currents in the central legs of the TF copper coils. The resulting power and flux loss can be a serious problem in any ohmically driven spherical tokamak. These losses, first discussed by Colchin [28], were estimated by S. J. Biao (PRC) [29] by modeling each one of the 12 pie-shaped sections of the TF coil with an equivalent hollow cylindrical conductor with radius r_e ,

$$r_e = \sqrt{\frac{(r_2^2 - r_1^2)}{N} - \frac{s(r_2 - r_1)}{\pi}}$$

where r_1 and r_2 are the inner and outer radii of the TF core and s is the TF insulation thickness. The cylindrical conductor is hollow to simulate the cooling line. The field

penetration problem can be exactly solved for this geometry, given a prescription of the solenoid current. Both solenoid and TF legs are assumed to be infinitely long. The OH current variation is modeled by a slow OH coil current rise phase (125 ms, 0 to 60 kA) followed by a fast current decrease phase (10 ms, 60 to 46.6 kA), consistent with time dependent simulations of the solenoid-plasma system. Our calculations indicate that for 12 legs of the TF coil, the net OH flux swing and the maximum voltage are reduced by ~25%, and 200 kJ of energy are lost by the eddy currents in the TF leg. To prevent this loss of performance, longitudinal slots are machined in the TF coils. In that case the system is better represented by 24 TF legs; the losses are then reduced to ~10% of flux and voltage, and 90 kJ of energy. Power, flux and voltage losses scale roughly as $1/(\text{number of TF legs})$.

5.9 MHD stability

It is well known that details of the plasma current density and pressure profiles, as well as the plasma shape, the total plasma current and β affect the MHD stability properties of the plasma. In this section we will present some preliminary studies of the MHD stability characteristics of plasmas in USTX. It is assumed that confinement properties, auxiliary heating and/or auxiliary current drive are compatible with the plasma profiles being investigated.

A preliminary study of MHD stability for the USTX point design ($A = 1.43$, $R_0 = 0.7$ m, $I_p = 1$ MA, $B_{T0} = 0.5$ T) was carried out by D. Strickler, ORNL [14], with the stability analysis code DCON [30] courtesy of Alan Glasser, LANL. The code evaluates the Direct Newcomb criterion for MHD stability. Mercier stability, high- n ballooning modes and low- n internal modes were studied. Conventional current density ($l_i \sim .7$) and pressure profiles were used. Results are shown in cases 1-3 of Table 5.2.

To ensure Mercier stability, q_{axis} has to be sufficiently greater than unity. This, in many cases, produces a hollow flux-surface-averaged current-density profile (as a function of Ψ). This appears to be a general feature of high-current low- A tokamaks. The maintenance of a steady-state hollow current-density profile is of great importance to research on advanced tokamak concepts. Combined transport and MHD studies (theoretical and experimental) are needed to investigate those profiles.

Table 5.2. MHD stability for $A = 1.43$ USTX point design, with $\kappa = 1.6$, $\delta \sim .25$, (except $\kappa = 1.7$, $\delta \sim .33$ in cases 4 and 5).

Case #	l_i	q_{axis}	q_{edge}	$\beta_T(\%)$	β_N	Mercier	Ballooning	Int. $n=1$	Ext. $n=1$
1	.60	1.10	4.77	6.3	1.58	U	S		
2	.50	1.37	4.78	5.8	1.45	S	S	S	
3	.51	1.25	4.91	9.2	2.29	S	S	U	
4	.46	1.40	5.19	11.3	2.75	S	S	S	S
5	.40	1.30	5.75	17.3	4.2	S	S	S	?

Because of the low magnetic shear, $(r/q)dq/dr$, near the axis, characteristic of the low- A plasmas we have studied, the (1,1) mode may well produce interesting effects if $q_{\text{axis}} < 1$, as mentioned in Section 3.3. For now it has been assumed that $q_{\text{axis}} > 1$.

Recent numerical studies by Hender [31] indicate that the edge q limit rises at low aspect ratio. For $A = 1.4$, the edge q is limited at 3, for $A = 1.2$ the limit is 4. This result doesn't impact the present studies, since $q > 4$ in every case considered.

We have performed initial profile optimization studies using EFIT and DCON. Note that this procedure guarantees that the PF system is capable of containing the designed plasma (it is assumed that transport properties and auxiliary heating and current drive allow the existence of that plasma). This crucial step is often missing from MHD studies. The results are shown in cases 4 and 5 of Table 5.2. The plasma may be in the second stability regime for ballooning modes (implying better stability as pressure is increased), and there is great benefit in raising q_{axis} to improve Mercier stability. A partially optimized plasma, case #4 of Table 5.2, is stable to all modes, without a conducting wall, with $\beta_T = 11\%$. Flux contours, safety factor, pressure and current profiles are shown in Fig. 5.7. Further optimization is possible, as evidenced by case #5, but current density profiles become increasingly hollow. The consistency of hollow current density profiles and centrally peaked pressure profiles with plasma transport and resistivity needs to be investigated.

MHD stability can improve significantly at lower aspect ratio, higher elongation, and with more advanced (hollow) plasma current-density profiles. Figure 5.8 illustrates an $A = 1.25$ equilibrium solution, computed by D. Strickler (ORNL) with FBEQ. The plasma has toroidal field $B_{T0} = 0.25$ T, current $I_p = 1.0$ MA, elongation $\kappa = 2.0$, and low internal inductance $l_i = 0.2$. It is Mercier stable, and stable to ideal $n = 1$ and ballooning modes at $\beta_T = 30\%$, $\beta_N = 4.5$ (DCON).

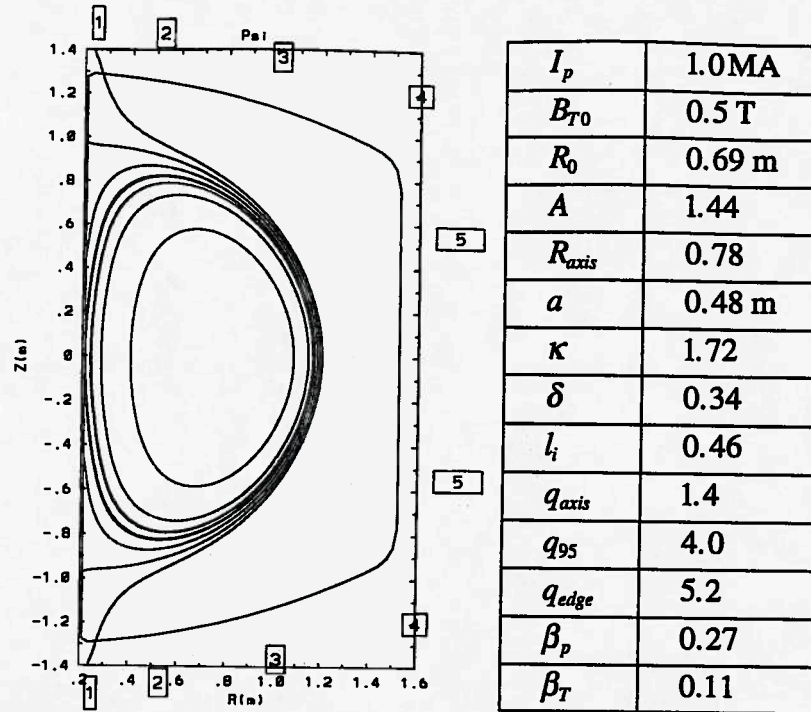


FIG. 5.7a. Flux contours of an optimized plasma (case #4), stable to Mercier, high- n ballooning, $n = 1$ internal and external kink modes (without a wall).

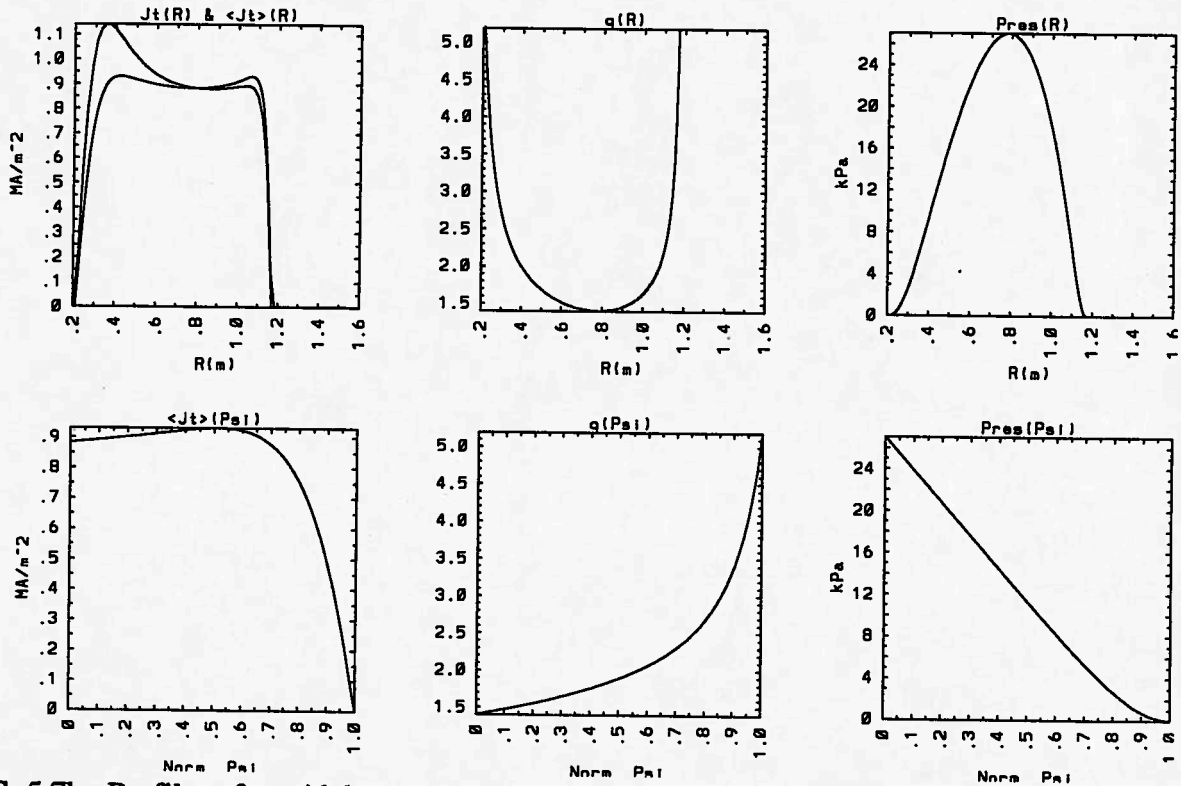
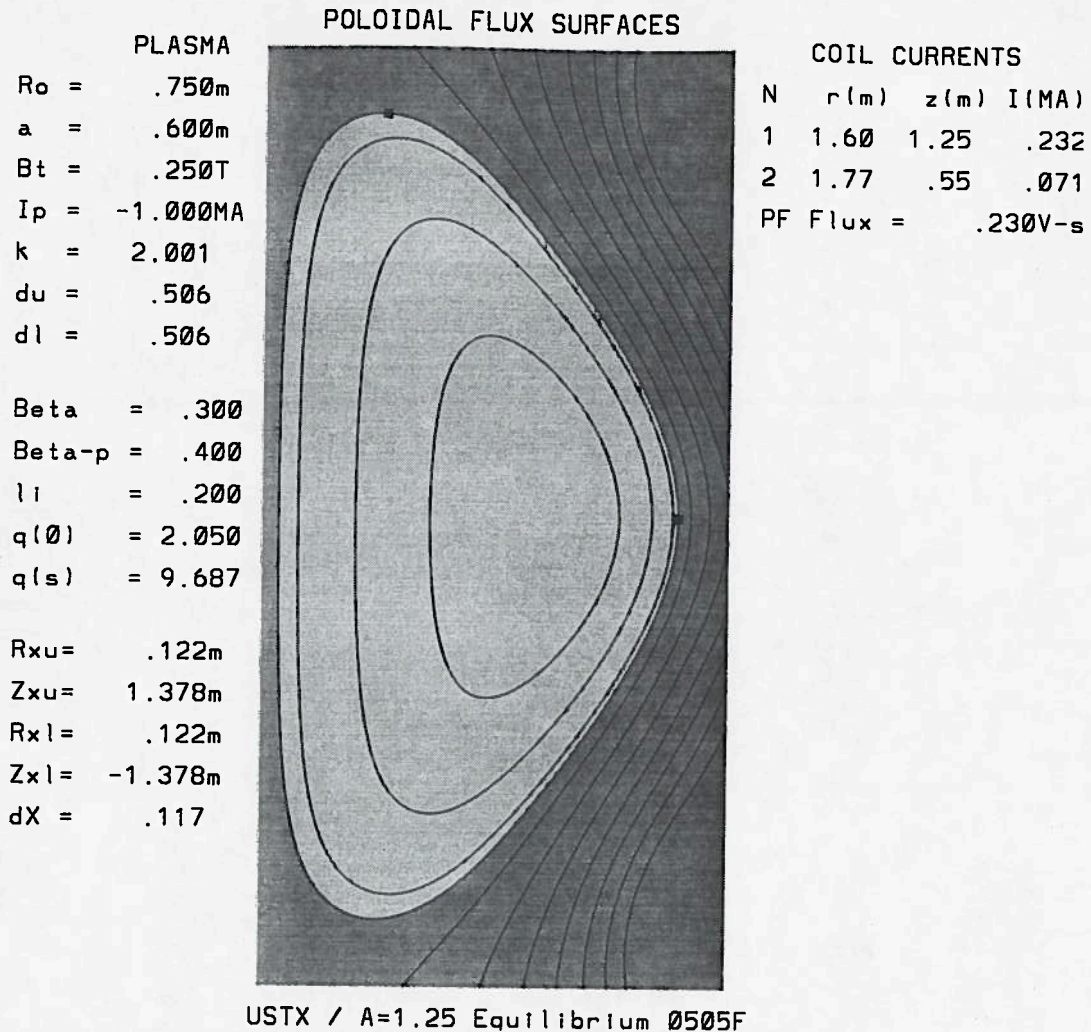
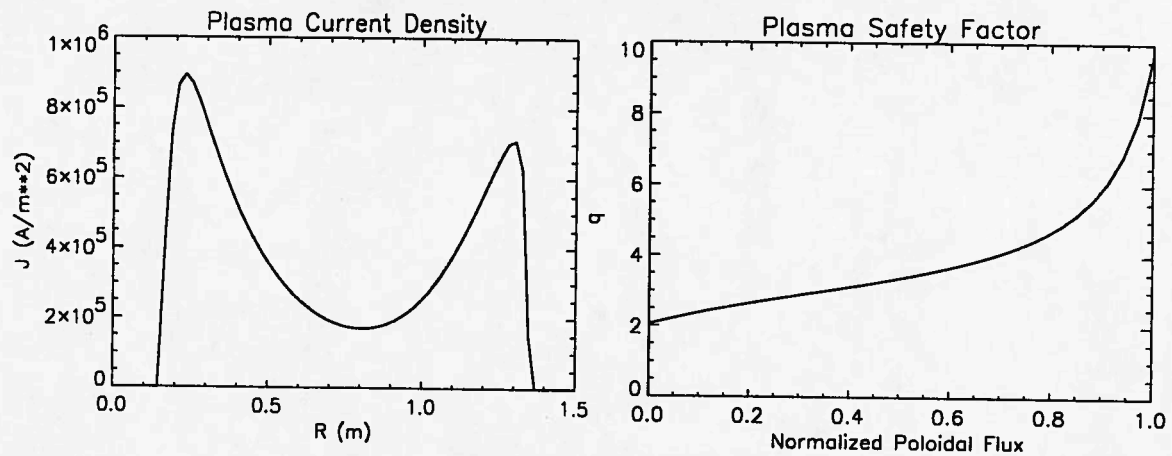


FIG. 5.7b. Profiles of toroidal current density J_T , safety factor q and pressure p , as a function of R at the equator, and as a function of normalized poloidal flux, corresponding to the plasma described in Fig. 5.7a.

FIG. 5.8a. Flux contours for an optimized plasma with $A = 1.25$.FIG. 5.8b. Profiles corresponding to the plasma of the previous figure: a) Current density profile vs. R at the equator, $Z = 0$, b) Safety factor vs. normalized Ψ .

Garofalo and collaborators at Columbia University [32] studied low- n external kink modes for USTX, with the PEST code [33]. With $q_{\text{edge}} = 3.8$, the presence of a cylindrical perfectly conducting wall at $R = 1.25$ m improves the normalized β limit from 3 to 6. They also studied case #4 of Table 5.2. The Grumman equilibrium code [34] was used to reconstruct the EFIT equilibrium we had generated. They confirmed with PEST the DCON findings of stability to internal modes, and found the $n = 1$ external kink mode to be stable without a wall. By increasing pressure in the same general equilibrium configuration, the critical β_N , β_{crit} , is extrapolated from a plot of beta vs. growth rate. Shown in Fig. 5.9 are the β_{crit} values for the first few low- n modes, with and without a wall, and for high- n ballooning modes. It is found that a partial wall at $R = 1.25$ m stabilizes the $n = 1$ kink mode up to $\beta_N = 6$, but the plasma would become ballooning unstable at $\beta_N = 4.35$. (Further profile optimization may raise the ballooning stability limit).

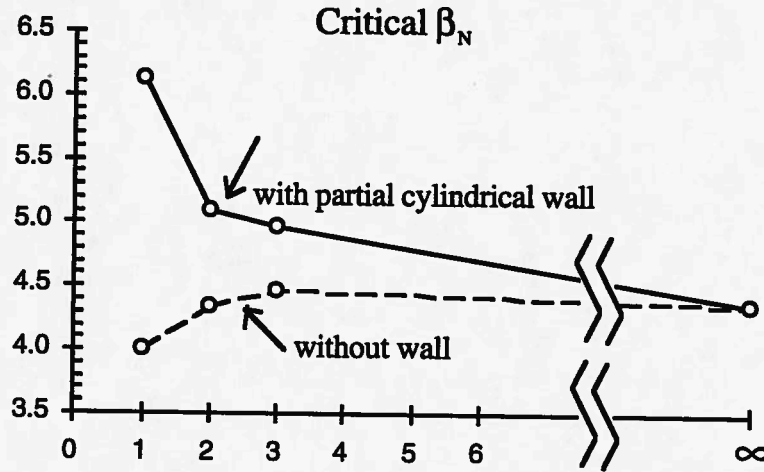


FIG. 5.9. Ideal MHD stability with and without a partial wall for q and p profiles similar to those shown in Fig. 5.7b.

Reverse central shear configurations are considered advantageous for advanced tokamak operation. In collaboration with L. Lao (GA) [35], we developed an example of a possible reversed shear configuration for USTX, as a demonstration that such equilibria are accessible in spherical tokamaks in general and USTX in particular. It is shown in Fig. 5.10. MHD stability studies of that example with DCON indicate good stability to internal modes.

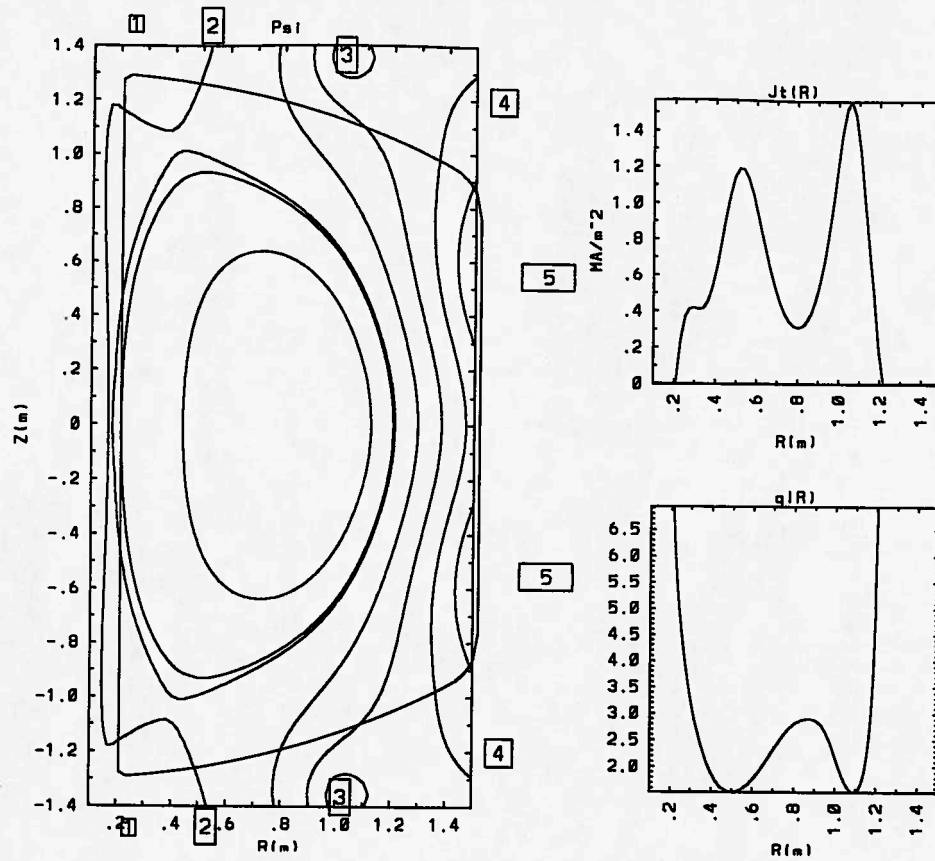


FIG. 5.10.: A negative central shear configuration example for USTX. It has $I_p = 1\text{Ma}$, $B_T = .5\text{ T}$, $a = .5\text{ m}$, $R = .71\text{ m}$, $\kappa = 1.9$, $\delta = .39$, $\beta_T = .2$, $l_i = .66$.
a) Flux contours; b) toroidal current density profile; c) safety factor profile.

MHD stability of low aspect ratio tokamaks is a rapidly developing field. Future collaborations with various institutions are planned. Columbia University, IFS, GA, LANL and ORNL have all expressed an interest in expanding these preliminary MHD studies of USTX.

References to Chapter 5

- [1] R. Gandy and G. Hartwell, personal communication (1995).
- [2] S. Ejima, R. W. Callis, J. L. Luxon, *et al.*, Nucl. Fusion **22** (1982) 1313.
- [3] S. P. Hirshman and G. H. Neilson, Phys. Fluids **29** (1986) 790.
- [4] Y. S. Hwang and M. Ono, personal communication (1995).
- [5] B. LLOYD, G. L. Jackson, T. S. Taylor, *et al.*, Nucl. Fusion **31** (1991) 2031.
- [6] A. Tanga, P. R. Thomas, J. G. Cordey, *et al.*, in *Tokamak Startup* edited by H. Knoepfel, (Plenum Press, New York, 1986), p. 159.
- [7] J. L. Porter, *Thomson scattering on the Texas Experimental Tokamak*, University of Texas at Austin (1985).
- [8] S. Attenberger, B. Balet, D. J. Campbell, *et al.*, in *Proceedings of the 17th European Phys. Soc. Conf. on Controlled Fusion and Plasma Heating*, Amsterdam, (European Physical Society, 1990), Vol. 14B, Part I, p. 5.
- [9] J. Wesson, Nucl. Fusion **29** (1989) 641.
- [10] J. L. Porter, P. E. Phillips, S. C. McCool, *et al.*, Nucl. Fusion **27** (1987) 205.
- [11] S. C. Jardin, M. G. Bell, and N. Pomphrey, Nucl. Fusion **33** (1993) 371.
- [12] M. Gryaznevich, R. J. Colchin, R. Duck, *et al.*, in *Proceedings of the 21st European Phys. Soc. Conf. on Controlled Fusion and Plasma Physics*, Montpellier, (European Physical Society, 1994), Vol. 18B, Part 1, p. 22.
- [13] L. L. Lao, H. St. John, and R. D. Stambaugh, Nucl. Fusion **25** (1985) 1611.
- [14] D. J. Strickler, Y.-K. M. Peng, and J. Galambos, personal communication (1995).
- [15] A. Sykes, J. W. Connor, R. Duck, *et al.*, Plasma Phys. Control. Fusion **35** (1993) 1051.
- [16] G. H. Neilson, G. R. Dyer, and P. H. Edmonds, Nucl. Fusion **24** (1984) 1291.
- [17] E. A. Lazarus, J. B. Lister, and G. H. Neilson, Nucl. Fusion **30** (1990) 111.
- [18] A. Sykes, M. Bevir, R. Bamford, *et al.*, in *Plasma Physics and Controlled Nuclear Fusion Research 1994* (International Atomic Energy Agency, Vienna, 1995), .
- [19] Y. S. Hwang, M. Yamada, T. G. Jones, *et al.*, in *Plasma Physics and Controlled Nuclear Fusion Research* (International Atomic Energy Agency, Vienna, 1994), .
- [20] R. Granetz, D. Gwin, and J. Irby, ITER disruption Expert Group Workshop, Feb. 1995. (1995) .
- [21] G. M. Staebler, F. L. Hinton, J. C. Wiley, *et al.*, Phys. Plasmas **1** (1994) 909.
- [22] D. W. Ross and J. C. Wiley, Bull. Am. Phys. Soc. **40** (1995) .
- [23] S. P. Hirshman, Phys. Fluids **31** (1988) 3150.
- [24] P. H. Edmonds, S. J. Wang, and E. R. Solano, Fusion Technology **592** (1990) .
- [25] S. C. Jardin, N. Pomphrey, and J. DeLucia, J. Comp. Physics **66** (1986) 481.
- [26] L. L. Lodestro and L. D. Pearlstein, Phys. Plasmas **1** (1994) .
- [27] S. W. Haney, L. J. Perkins, J. A. Crotinger, *et al.*, Bull. Am. Phys. Soc. **39** (1994) 1595.

- [28] R. J. Colchin, to be published in *Fusion Technology* (1996) .
- [29] C. Siyue, C. Xingqian, W. Songtao, *et al.*, University of Texas at Austin, Fusion Research Center Report # 476 (1995) .
- [30] A. H. Glasser, *Phys. Plasmas*, submitted Feb. 1995 (1995) .
- [31] M. Gryaznevich and the START team, in *Proceedings of the U.S.-Japan Workshop for Low Aspect Ratio Tokamak and International Workshop on Spherical Torus*, Princeton, N.J., (PPPL, 1995) .
- [32] A. M. Garofalo, M. E. Mauel, G. A. Navratil, *et al.*, Columbia University, Plasma Physics Laboratory Internal Report 129 (1995) .
- [33] R. C. Grimm, J. M. Green, and J. L. Johnson, *Methods Comput. Phys.* **16** (1976) 253.
- [34] J. DeLucia, S. C. Jardin, and A. M. M. Todd, *J. of Comp. Phys.* **37** (1980) 183.
- [35] L. Lao, personal communication (1996).

CHAPTER 6

DEVICE AND POWER SYSTEMS DESCRIPTION

The design of the USTX device has been completed to a level required to establish engineering feasibility and to generate a preliminary cost estimate. The device magnetic and power system design is directed to the performance parameters described in the physics section of this proposal. An evolutionary program is envisaged; initially an ohmically heated, inductively driven device will be used to establish the fundamental performance and physics. Later phases of the program will include auxiliary heating and current drive advances. Only the base device (including provision for later expansions) is described here.

6.1 Overall description

The base USTX device employs inductive drive both for plasma breakdown and for plasma current generation and maintenance. This technique has been chosen because it is well understood and very reliable. However the current drive and OH solenoid, required for this inductive drive, is the critical feature of the machine. For this reason the description presented here concentrates on the design of the center TF core and OH inner solenoid; the design of the remainder of the device being rather straightforward. Additionally, details of innovative design features are described. These include the vacuum vessel support concept, the TF center column to radial leg joint and the TF return winding.

The basic machine design has an interchangeable TF inner core, OH solenoid and vacuum vessel sleeve assembly. Two designs have been pursued, one with an aspect ratio of 1.43 and one with an aspect ratio of 1.25. The present intent is initially to build the $A = 1.43$ design; the $A = 1.25$ design will be installed after operating experience has been obtained. A summary of the solenoid and plasma parameters for the two cases is given in Table 6.1. The mechanical and electro-magnetic constraints - number of turns, coil stresses, room temperature resistance, etc. - for the solenoid were calculated using the procedure described in Chapter 5. The solenoid performance was optimized to match the available power supply and motor generator set package.

USTX can be considered as consisting of five essentially independent structures, namely a) the vacuum vessel, b) the inner ohmic drive and heating solenoid, c) the poloidal-field (PF) coils, which complete the poloidal-field circuit, d) the toroidal-field (TF) system, including the center core and the return legs, coil cross-overs and feeds, and e) the support structure. A summary of these structures is listed in Table 6.2. The inner core assembly, consisting of the TF core, the OH solenoid, and the vacuum vessel inner sleeve requires special focus as an integrated design. Electrical power will be supplied by a number of power supplies driven by three flywheel storage motor-generator (M/G) sets, capacitor banks and the electrical grid.

Table 6.1. Solenoid and plasma parameters for $A = 1.43$ and $A = 1.25$ point designs. (For worksheet see Tables 6.3-4.)

A	1.43	1.25
R_0 (m)	0.70	0.75
a (m)	0.49	0.60
κ	1.7	2.0
I_p (MA)	1.00	0.5
B_{T0} (T) at R_0	0.5	0.5
V_{loop} (V)	1.5*	1.5*
l_i	0.7	0.3
L_{Plasma} (μ H)	0.48	0.22
$M_{sol-plasma}$ (μ H)	7.9	2.56
τ_{flat} (s)	0.13*	0.04*
I_{sol} (kA)	± 60	± 60
N_s (turns)	240	160
Layers	4	2
R_{sol} (m Ω)	7.9	7.8
P_{OH} (MW)	28.5	28.2

*The flat-top times quoted here are for inductive current drive only, at peak current, with a purposely pessimistic assumption that $V_{loop} = 1.5$ V. For more favorable confinement scalings, or for operation at reduced currents or for non-inductive current drive scenarios, flat-top times exceeding two seconds are predicted.

The vacuum vessel is a single welded structure constructed of non-magnetic stainless steel. There is no insulating gap and the inner sleeve and upper and lower caps are built from thin wall ($\sim 1/4$ ") material in order to reduce eddy-current effects. Poloidal

ribs are to be installed to ensure adequate mechanical strength. Flanges will be manufactured to standard dimensions to reduce cost, the large radial ports are Helicoflex sealed, and all other ports are standard ConFlat. The vessel will be electrically baked out to between 120 °C and 180 °C. (The temperature limit will be established during detailed design to be consistent with insulation and clearance requirements; present design is to heat the vessel to 180°C and to separately heat the PFCs to ~400°C using SS resistance heaters). The vacuum vessel is attached to the support structure by a combination of swinging links and hydraulic positioners. Pumpout is conventional and consists of two turbo-pumps backed by oil roughing pumps.

Table 6.2. USTX concept machine parameters for the $A = 1.43$ design.

Vacuum Vessel		
Material	316 Stainless Steel	
Thickness	1/4" (except outer wall may be thicker)	
Height	2.6 m	
Vessel I.D.	3.05 m	
Bore I.D.	0.38 m	
Solenoid (A = 1.43)		
Material	Chrome Copper 182	
Length	2.6 m	
Inner radius	0.105 m	
Outer radius	0.180 m	
Number of turns	4 layers 60 turns wound 4 in hand	
PF Coils		
Material	OFHC Copper Half Hard	
Number	10 Coils up/down symmetric	
TF Coil		
Material	OFHC Copper Half Hard *	
Number of Turns	12	
Core I.D.	0.030 m	
Core O.D.	0.170 m	
Core Height	4.5 ±0.5 (TBD) m	
TF Core	Machined OFHC copper	
TF Return Legs	OFHC Copper 1-1/2" by 6" rectangular bar	
Outer Leg I.D.	5.1 m (inscribed circle)	
Support Frame		
Material	Stainless Steel	
Primary Structure	4" by 4" rectangular cross-section bar	

The ohmic solenoid is the critical element of an inductively driven low-aspect-ratio tokamak, and an extensive study has been made in order to optimize the design and to match to available power supplies. The optimization procedure is described in Chapter 5. In summary, the TF-core outer radius and the vacuum-vessel inner-wall radius establish the inner and outer solenoid radii. The general requirement for large cross section and short conductor length drives the design to high solenoid current, constrained by power-supply and field-error limitations. It is essential that all conductors are continuous, with no joints in the body of the solenoid. The stress calculation requires a fatigue criterion, such as the von Mises, and must include the vertical stress due to the finite length of the solenoid. A finite element calculation of the final conductor cross-section, including the stress concentration effects of the cooling line cutout, was made in order to identify the optimum cooling line orientation and to establish the available safety margin [1]. The high stresses in the conductor unfortunately call for high strength coppers; the present plan is to use a chrome copper alloy, C-182. Insulation is critical; it is proposed to use Kevlar fabric to prevent insulation damage caused by the high stresses associated with the coil winding. All assemblies will be vacuum/pressure impregnated with high-temperature thermoset epoxy using precision molds for dimensional control.

The PF coils are located outside the vessel and inside the TF return legs. The design is very conventional with current densities low enough to allow free air convection cooling. The machine design allows the coils to be fabricated off site and installed during assembly. The windings may be tapped to increase the flexibility of the device. Initial plasma stability studies indicate that both axisymmetrically stable and unstable plasmas can be produced. A number of smaller coils for position feedback and control will be added if required for stability of highly elongated or triangular configurations.

The TF design is necessarily innovative; because of the limited space in the center column a highly optimized design is necessary. The number of TF coils is a compromise between access required for diagnostics, neutral beam systems, etc., acceptable TF ripple and power supply availability. The USTX design has selected a 12 turn TF system. It is desirable for each TF coil to be a single turn in order to maximize the packing factor and hence the allowable effective current density, and this requires high conductor currents. The center TF core is water cooled. Conduction time from the innermost material may be the limiting cooling path for shot repetition rate. Two cooling lines are installed in each leg in order to reduce the conduction path as much as possible. In order to reduce eddy current effects a longitudinal slot will be cut in each TF segment.

The design proposes that the TF core, the inner solenoid, and the vacuum-vessel sleeve telescope together after manufacture and testing of the individual components. This requires that the ends of the TF core be of the same or smaller diameter than the center section. The design has a T-shaped heel plate that bolts to the center core in order to transfer the current and hoop forces from the vertical core to the radial legs. The central core expands approximately 7 mm vertically per shot for full performance operation. To supply sufficient compliance for this expansion, horizontal slots will be cut in the TF upper radial leg. The return legs are conventional, convection cooled. The turn-to-turn cross-overs and TF feeds are located at the outer corners of the top and bottom radial legs. The present design includes a concept for effectively halving the number of TF coils, from 12 to 6, for ripple-field experiments. For a TF outer-leg radius of 2.6 m, the normalized ripple field, defined as $(B_{\max} - B_{\min}) / (B_{\max} + B_{\min})$ at the midplane outer plasma edge, will be increased from about 0.1 % to about 4 % (see Fig. 5.6.).

The separate components of the tokamak are supported by a drum shaped external exoskeleton or support frame. The vacuum vessel is connected to the exoskeleton by a set of swinging links, so located that for uniform vessel expansion the center line of the vessel remains fixed. A set of hydraulic cylinders also connects the vessel to the structure; these cylinders will be locked during each shot in order to absorb the transient forces, but otherwise will allow differential movement for thermal expansion.

A plan view of the entire device including all supporting systems and power supplies is shown in Fig. 6.1. A more detailed view of the tokamak inside the enclosure, including layouts for the neutral beam line and the 2 MeV HIBP, is given in Fig. 6.2. The design includes the capability of installing a single beam line (located in the Southwest corner of the tokamak enclosure); however installation space will be reserved for a possible upgrade to a second beam. The design includes the option to modify the tangency radius of the neutral beam by reworking the front-end flange and rotating the beam-line table. The extreme positions are shown in Fig. 6.3. An elevation view of the device, including a beam line and the HIBP is shown in Fig. 6.4. The HIBP assembly and the neutral beam have been rotated into the plane of the drawing. A detailed elevation view is given in Fig. 6.5. The plasma cross section is for a 1 MA high-triangularity discharge at zero solenoid current, similar to the equilibrium presented in Fig. 5.7. The complete tokamak assembly, in isometric projection, is shown in Fig. 6.6.

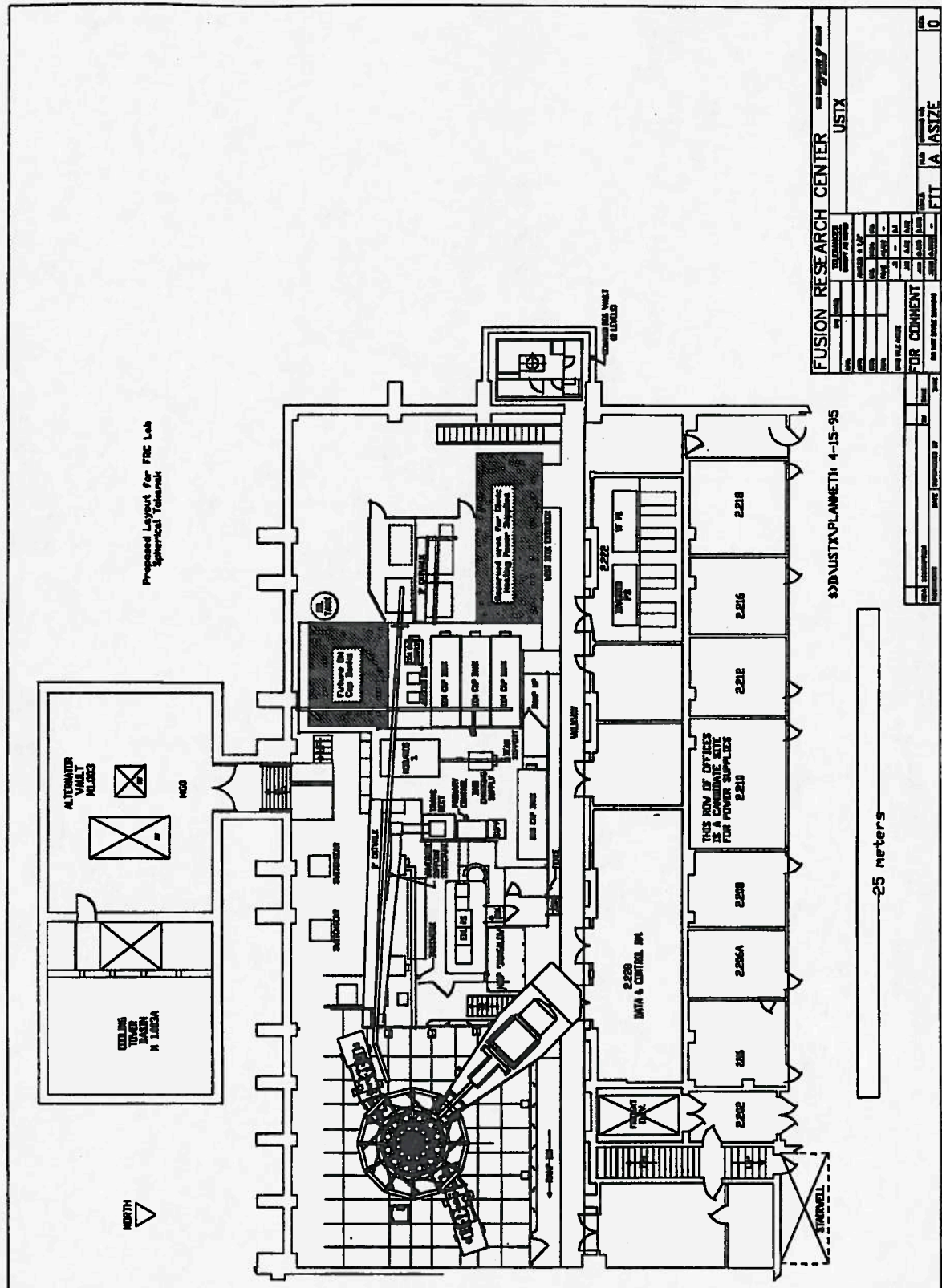


FIG. 6.1. Plan view of USTX, with supporting systems and power supplies.

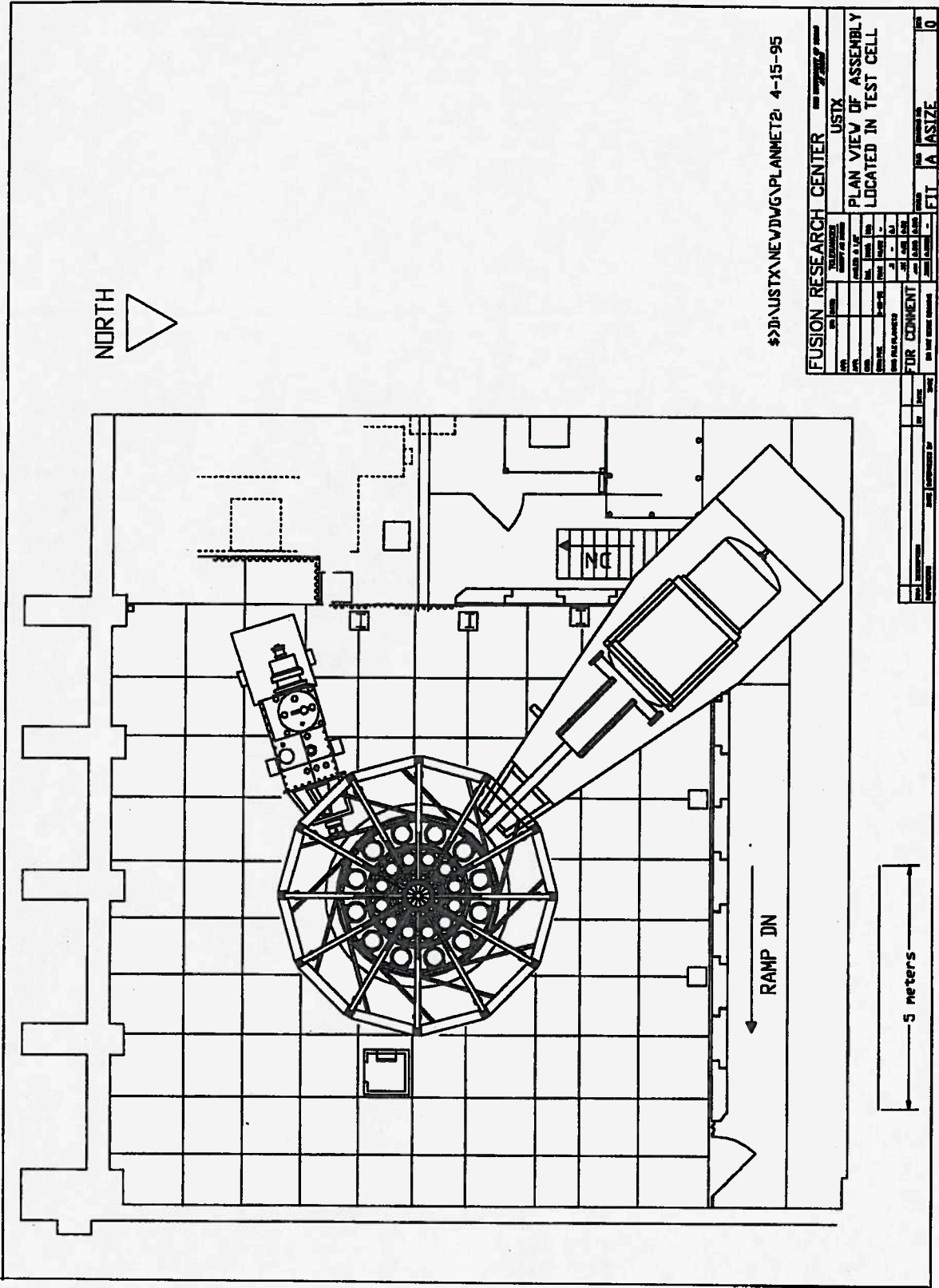
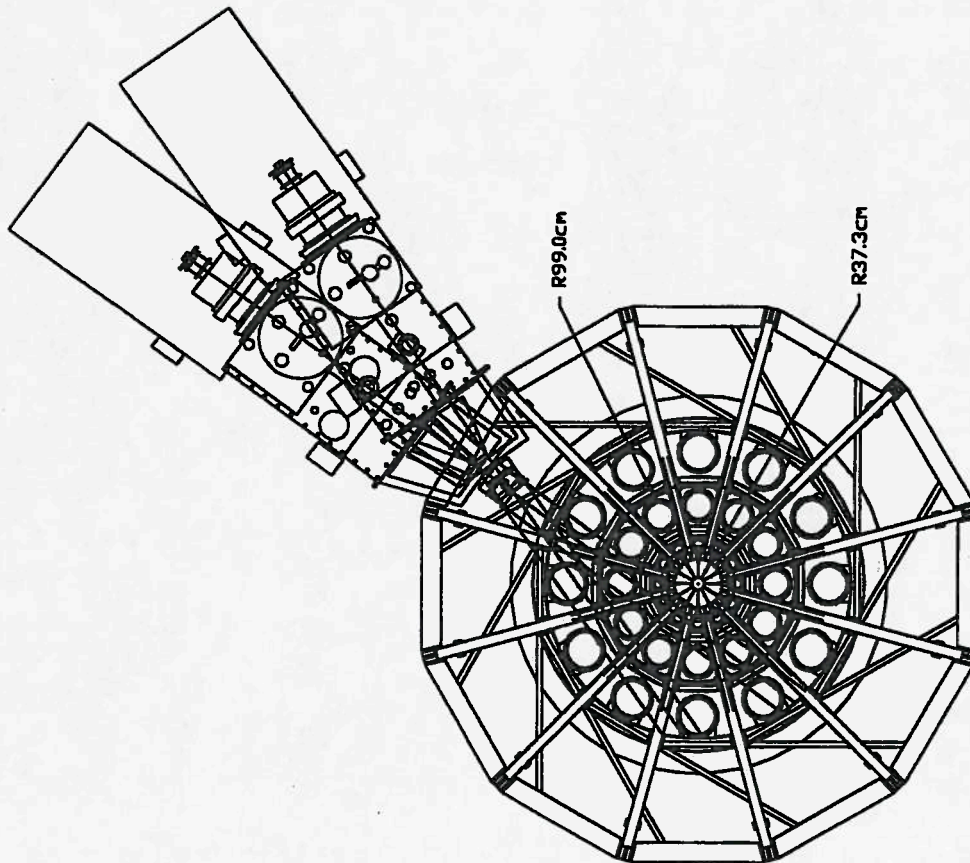


FIG. 6.2. Plan view of USTX, with layouts for neutral beam line and 2 MeV HIBP.

[illegible]

6-8

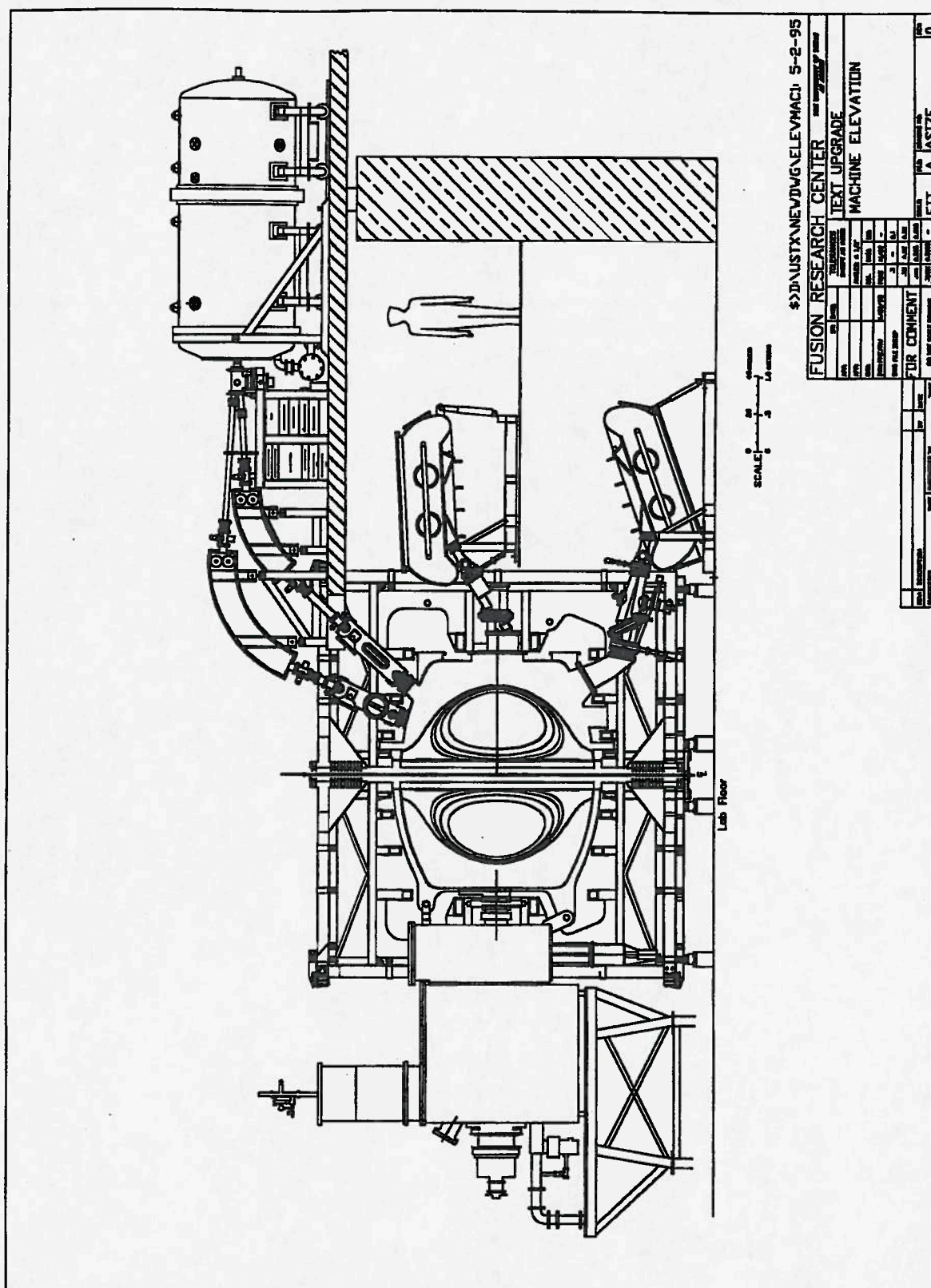


FIG. 6.4. Elevation view of USTX showing beam line and HIBP rotated into plane of view.

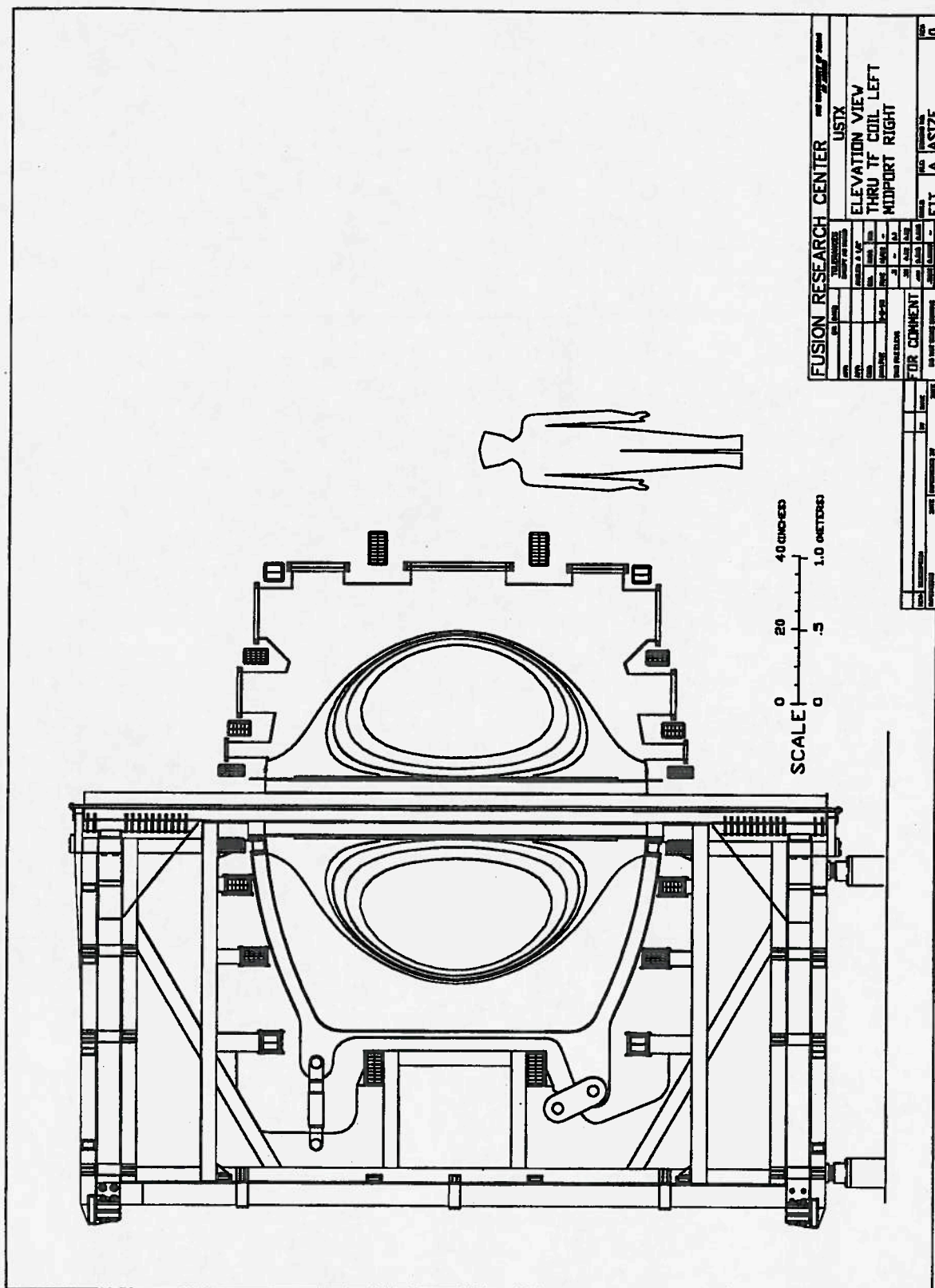


FIG. 6.5. Detailed elevation view of USTX.

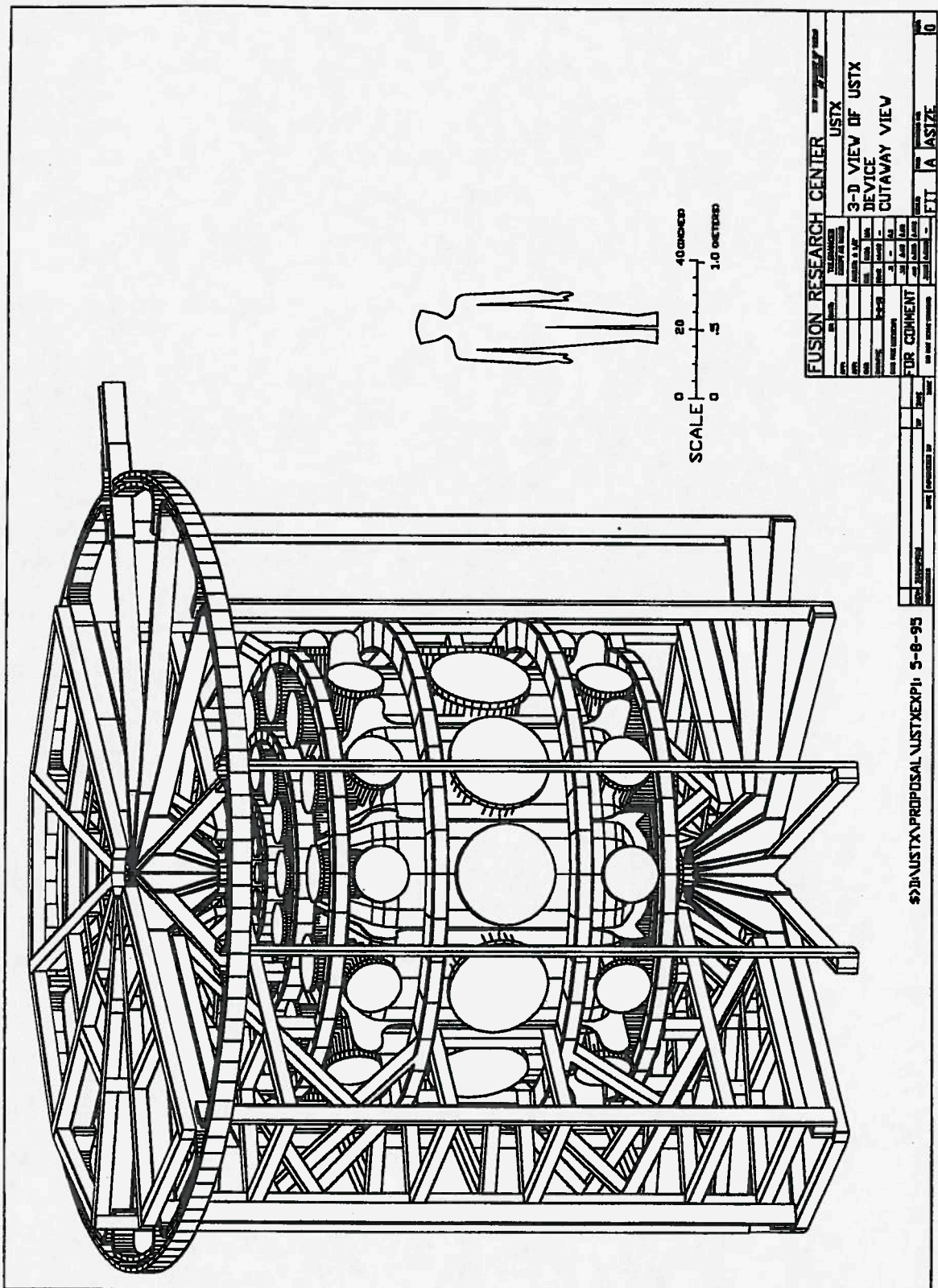


FIG. 6.6. 3-D view of the complete USTX tokamak assembly.

Power requirements are discussed in Sec. 6.7, and are within the capabilities of the TEXT inertial generator system and available grid power. The OH solenoid is designed to match the available P/S and M/G set performance. The plasma breakdown voltage will be produced either by reversing the OH P/S voltage or by the addition of a commutated series resistor. Breakdown will be assisted by ECRH. The PF coils and TF core have been sized to allow multi-second flat-top operation with non-inductive current drive.

The flat-top pulse length for the $A = 1.43$ point design with a plasma current of 1 MA is about 0.13 s, limited by the OH P/S and associated M/G set capabilities and by the stress limit in the solenoid conductor. This time may exceed 300 msec for more favorable confinement scaling. For non-inductive current-drive operation the flat-top duration will be limited by either the TF core heating, the PF-coil P/S energy availability, or the TF P/S limits. For the 1-MA case at full toroidal field, the corresponding maximum flat top is about 0.5 s, limited by the TF power supply and M/G set combination. For lower toroidal-field and plasma-current cases the flat top can be extended.

6.2 TF coil, OH solenoid and PF coils

The concentric center post coils (TF, OH solenoid) and the inner vacuum-vessel sleeve are all constructed separately and made such that they will telescope together. These components are assembled to form the center post and can be disassembled if required. The solenoid will be wound on a fiberglass cylinder which will supply the base for the supporting structure. Differential expansion, both radial and axial, requires a compliant support system and preferably a compliant material between the various components. The detailed design has not yet been established, but the present concept proposes the installation of compressible high-temperature silicon-rubber sleeves between the separate components. The properties of the insulating materials will establish the maximum bakeout temperature of the vessel. An alternative concept is that during operation the entire assembly will be filled with a high-temperature anathixotropic material, for instance, a high viscosity silicon oil, to absorb the transient off-axis loads from disruptions and fault conditions. The 1 cm to 2 cm gaps between the TF core and the solenoid, and between the solenoid and the inner sleeve, are considered adequate for manufacturing tolerance, assembly clearance and thermal expansion.

The present plan is to build at least two solenoid assemblies. A prototype coil will be wound in order to develop the construction procedures required for construction to the required tolerance and performance specifications. This prototype solenoid will be tested to maximum limits in an accelerated life cycle program. The final solenoid (for an aspect ratio of 1.43) will be wound with chrome copper conductor. A lower-aspect-ratio modification (for an aspect ratio of 1.25) will be designed and constructed at a later date.

The TF radial and return legs are single conductor rectangular cross-section OFHC copper, mounted to the exoskeleton. Cross-overs and returns are located at the outer upper corner of the coils. A design concept has been considered to provide a 6 turn TF system in order to study TF ripple effects.

The PF coils are conventionally wound multi-turn rectangular cross-section convection-cooled assemblies. The coil pairs PF1-A and PF4 are connected in series with the solenoid to simplify return field correction. These turns will be tapped for additional flexibility and in anticipation of installation of the $A = 1.25$ solenoid. Poloidal field current densities are kept below 2 kA/cm^2 .

TF core and return legs

The design of the center core assembly, and essentially the entire device, begins with the TF core. In order to minimize core heating, the smallest practical number of turns is required. This number is set by either the maximum available P/S current or the number of TF coils selected. The latter choice is normally a compromise between the TF ripple requirement and the need to maximize access to the plasma, particularly for the neutral-beam system. TF ripple is discussed in Chapter 5.8. The present selection for USTX is 12 turns, with a point design plasma radius of 0.7 m and a toroidal field of 0.5 T. The individual leg current is 146 kA which is within the performance range of the TEXT TF power supply. The support-structure design includes a central tie-rod with a diameter of 3.2 cm (1-1/4"), which defines the inner radius of the TF core at 2 cm (with 4 mm insulation clearance). Because of differential thermal expansion the stud will be coated with a non-stick material to provide expansion freedom between the stud and the TF core.

A design algorithm has been developed to complete the design of the TF core, which is described here in detail. A packing factor for the copper conductor, and an electrical resistivity for the material are selected. (At present the design is for OFHC

copper.) The resistivity used is increased by an estimated amount allowing for the effect of heating during the pulse. An equivalent rectangular flat-top pulse duration is chosen. This number is subsequently iterated against the P/S performance (and the TF coil resistance and inductance) to confirm that the design is adequate for the planned operating scenarios. A maximum temperature rise during the shot is selected. (The criterion used at present is that the maximum conductor temperature will not exceed 100 °C with the start temperature assumed to be 25 °C.) For the designs described here, the temperature range is set at 70 °C or less in order to allow extended flat-top performance for non-inductive current-drive scenarios.

With these criteria, the algorithm selects an outer radius for the TF core. Using this radius, an engineering drawing is made with proper allowance for insulation and cooling lines, and the actual packing factor calculated. The calculation is then repeated with this updated packing factor to produce a final TF core outer radius. Note that the packing factor is not sensitive to the TF segment detail.

The TF core design algorithm has been integrated into the design of the OH solenoid and incorporated into an EXCEL spreadsheet. The results for the two aspect ratios used in this design study are shown in Tables 6.3 and 6.4, in the next subsection.

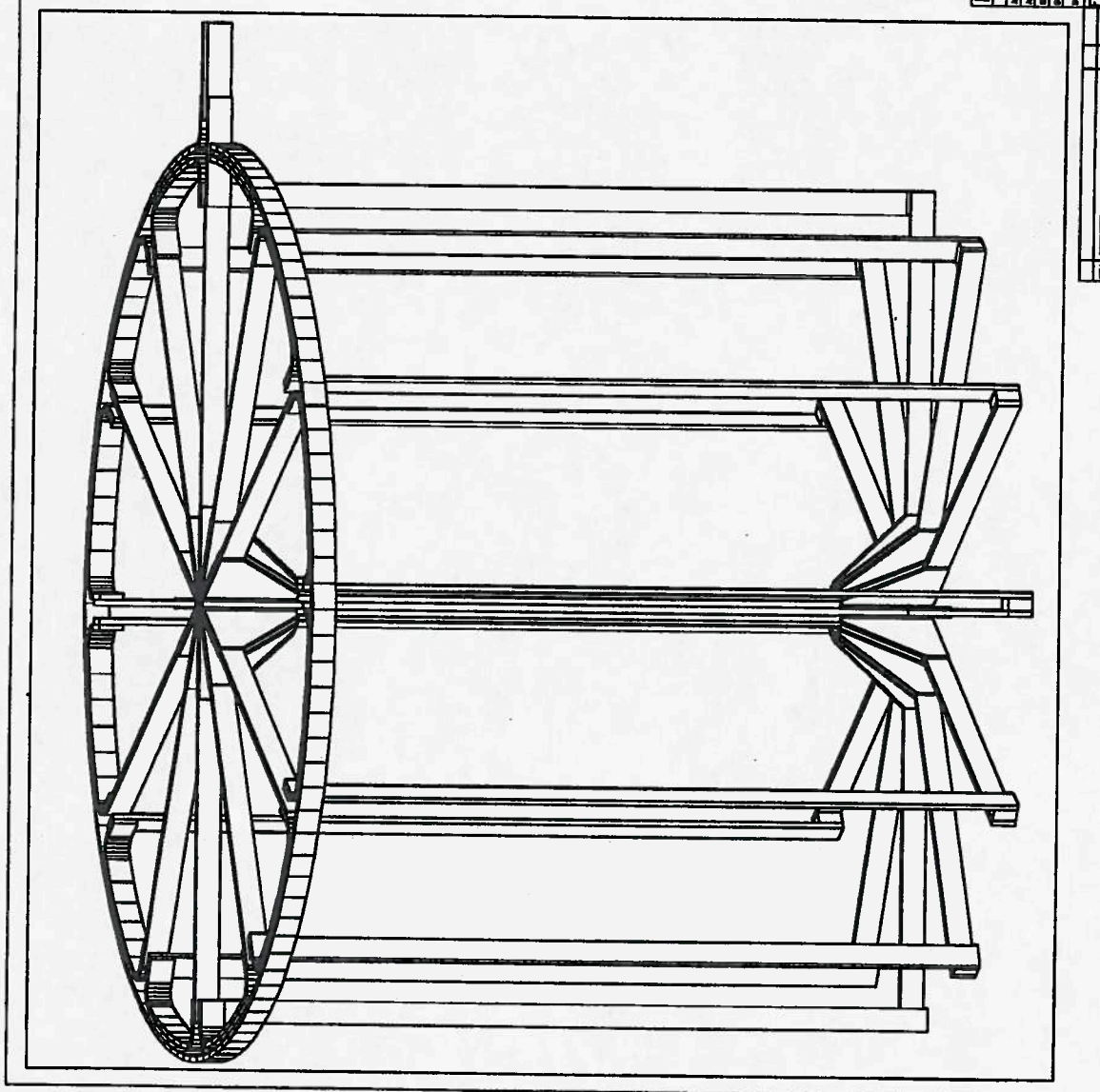
Eddy current effects in the TF core induced by the solenoid current ramps pose a potential problem in limiting the available volt-seconds and plasma breakdown voltage and in degrading the effective OH power supply parameters [2]. These effects are discussed in Chapter 5. A thin longitudinal slot will be machined in each TF core segment and filled with a 0.5 mm G-10 insulating sheet to increase the impedance to the magnetic flux. Details of this slit are shown in Fig. 6.9.

The TF core is cooled by copper lines laid into grooves machined into the pie-shaped segments (see Figs. 6.7, 6.8). The conduction path from the conductor extremities to the cooling lines is, at present, the limiting factor in the machine shot repetition rate, which is about five minutes between shots for the point designs. Each segment will be wrapped in 1 mm (0.040") of fiberglass insulation (two layers oppositely wound with 50% overlap per layer of 0.010 glass tape) and the individual segments separated by a 0.5 mm (0.020") G-10 spacer. The assembly will be wrapped in a 1 mm ground wrap and vacuum/pressure impregnated with epoxy. Dimensional control will be ensured by the use of precision molds and tooling.

The TF core height has been selected large enough to move the radial TF legs and the current direction transition into a region of relatively low vertical field in order to reduce the overturning forces as much as practical. The minimum constraint is to supply adequate room for the bolted assembly between the TF core and the TF radial legs. The maximum constraint is the available headroom required for assembly and maintenance, limited by the overhead clearance of the test cell.

A feature of the design is that the individual components of the center assembly are independently fabricated and assembled following full performance tests. This requires that the individual components - the TF core, OH solenoid and vacuum vessel sleeve - telescope together. Because of this requirement the clearance radius at the vertical to radial transition must be no larger than the overall core radius. An innovative design for this joint has been included in the design. A heel plate is welded to the radial leg and this plate bolted to the TF core segment. A triangular cheek plate is welded to the radial leg and the heel-plate to transfer out-of-plane loads. The bolt array is installed through the gap in the cheek plates. The bolt array is sized to maintain adequate compression force at the maximum TF current. A stack of domed spring washers will be installed on each bolt to ensure constant pressure. An isometric view of the TF coil assembly is shown in Fig. 6.7. The details of the end design are shown in Fig. 6.8 and of a core segment in Fig. 6.9. An end ring with hydraulic pre-load may be added to absorb radial loads.

The radial and outer legs will be fabricated from 3.81 cm by 15.24 cm (1-1/2" by 6") rectangular copper bar. The current density is low enough that convective cooling will be adequate for the design repetition rate of five minutes between shots. The TF core will experience about 7 mm vertical thermal expansion for a full performance shot. The present design includes a row of horizontal slots in the upper radial legs to increase the flexibility and allow relatively free vertical movement. The TF radial leg will be supported against out-of-plane forces by a pair of cheek plates attached to the radial arms of the exoskeleton. Differential movement will be against Teflon pads. The details of this design and the effect of these slots on the thermal performance will be developed in the detail design phase of the project. The feeds and cross-overs will be located at the upper outer corners where access is available and external loads are minimized. Details of the twelve coil cross-over and feed design are shown in Fig. 6.10.



6 - 16